Master Thesis

Estimation of anthropogenic greenhouse gas emission rates using Methane Airborne MAPper (MAMAP) spectroscopic measurements

Postgraduate Programme Environmental Physics (PEP)
Institute of Environmental Physics Bremen (IUP)
August 2013

Sven Krautwurst

1. Examiner: Prof. Dr. John P. Burrows
2. Examiner: Dr. Andreas Richter
Supervisor: Dr. Michael Buchwitz

Abstract

Carbon dioxide (CO_2) and methane (CH_4) are the two most important anthropogenic greenhouse gases. The quantification of their sources and sinks is essential to predict their future abundance and their impact on climate. The Methane Airborne MAPper (MAMAP) instrument provides spectroscopic measurements which can be used to estimate emission rates of localized CO_2 and CH_4 sources (e.g. of power plants, landfills, fossil fuel exploration sites, etc.).

In this manuscript, new measurements of the coal-fired power plants Jänschwalde and Schwarze Pumpe taken during a campaign in the year 2011 were investigated. The obtained column-averaged dry air mole fractions of carbon dioxide (XCO_2) were compared to previous data of the same power plants gathered during a campaign in the year 2007. It could be confirmed that a modification of the instrument, between 2007 and 2011, improved the quality of XCO_2 by a factor of approximately 2.

Furthermore, an algorithm was developed utilizing new vertically highly resolved potential temperature and wind profiles for a more realistic description of the atmosphere, in order to determine the plume propagation and its vertical distribution in it. From that, a mean wind speed of the plume used for emission rate estimates of the power plants Jänschwalde and Schwarze Pumpe in 2007 was estimated, and compared to the former emission rate estimates of the same power plants only applying vertically low resolved wind profiles. Finally, the vertically highly resolved wind profiles were also applied to the new measurement flight in 2011 for the power plant Jänschwalde in order to estimate emission rates.

The CO_2 emissions could be retrieved within $\pm 3.5\,\%$ for Jänschwalde 2007 (statistical uncertainty: $8.0\,\%$) and $+15.0\,\%$ for Schwarze Pumpe (statistical uncertainty: $11.9\,\%$) compared to the reported value by the power plant operator. In Krings et al. (2011), only using coarsely resolved wind profiles, the bias of $+8.3\,\%$ for Jänschwalde was by a factor of around 2 larger than in this study. The emission rate estimates and biases $\big($Krings et al. (2011): $-9.0\,\% \Leftrightarrow$ this study: $+15.0\,\%\big)$ of Schwarze Pumpe were not directly comparable because two different approaches were used due to a changing wind direction during the measurement flight, which actually violated the basic assumption of a quasi stationary plume of the model. Nevertheless, all emission rate estimates for 2007 agree well within the scope of uncertatinties. For Jänschwalde in 2011 the emission was underestimated by $7.9\,\%$ (statistical uncertainty: $6.4\,\%$) assuming it was the same as in 2007.

The statistical error of the emission rate estimates in 2011 was reduced by a factor of at least 1.25 due to the improved XCO_2 compared to 2007, whereas the largest systematic uncertainties of up to $\pm 13.0\,\%$ originated from a not well-known plume behaviour in the atmosphere.

Contents

Chapter 1

Introduction

Motivation

A decisive point in human history was reached during the 18th century, when James Watt developed the steam engine (Hatsopoulos, 2006). It triggered a development without which the current world would look differently. For the first time in history, energy could be concentrated in a relatively small area and was available in abundance. This was also the reason for the industrial revolution, which was based on the steam engine, and the steam engine was based on coal. While it was powering more and more looms and railways, its combustion residue polluted the environment. This adverse effect of seemingly unlimited energy resources culminated in the London Smog in 1952 (Bell et al., 2004). Whereby smog was a local phenomenon, other combustion products influenced and are still influencing the earth as a whole. The most famous one is carbon dioxide (CO_2), which absorbs thermal infrared radiation. Moreover, the concentration of the second most important so called greenhouse gas methane (CH_4) has also been increased due to anthropogenic emissions (Forster et al., 2007). This trapping effect of heat in addition to the natural greenhouse gas effect within the atmosphere is cause of concern in terms of global climate change.
As indicated by the Intergovernmental Panel of Climate Change (IPCC, 2007), the recent observed rise in mean global temperature is most likely caused by anthropogenic activities and emissions. On basis of the statements of the IPCC, first steps were taken to limit the emissions resulting from large carbon dioxide emitters (European Commission, 2007), at least. However, for that purpose, it is mandatory to measure and monitor these emissions precisely. Right now, the largest anthropogenic CO_2 sources are energy producing fossil fuel fired power plants (EPER, 2012). Their reported emissions are not based on direct measurements but for example, on emission factors. Evans et al. (2009) compared these calculated emissions with direct measurements in case of four power plants using coal, natural gas or oil as fuel. Their result was that the reported emissions are all too low by up to 15%. Ackerman and Sundquist (2008) who compared two datasets of the US for the year 2004 representing indirect and direct measurements of power plants, respectivily, came to a similiar conclusion. The calculated emissions

were always lower than the directly measured emissions. These two case studies show the difficulty of measuring CO_2 emissions accurately.
Besides the carbon dioxide emitters, there are also natural (wetlands) and anthropogenic (fossil fuels, livestock, rice paddies and landfills) methane sources (Wuebbles and Hayhoe, 2002). The feasibility of flux estimations of methane sources was studied by Babilotte et al. (2010). They compared five field-scale measurement methods applied to a landfill site, which disagreed by a factor of up to 7.
To provide additional understanding of emission sources of the two most important greenhouse gases, the Methane Airborne MAPper (MAMAP) (Gerilowski et al., 2011) was developed. It provides spectroscopic measurements in the short wave infrared (SWIR) to derive precise information about the amount of carbon dioxide and methane in the atmosphere on basis of the molecular absorption in solar backscattered radiation from the earth's surface. Strong CO_2 point sources like power plants has been used to develop the retrieval method and Krings et al. (2011) showed that the resulting emission rates are within $\pm 10\%$ of the reported values, whereas the uncertanties are of the same order of magnitutde as described by Evans et al. (2009). Krings et al. (2013) also showed that emissions of strong CH_4 point sources can be estimated with an uncertainty of 13.5%. This knowledge will be used to measure fluxes of large extended areal methane sources like landfills, wetlands or fossil fuel exploration sites which cannot be determined sufficiently. Additionally, it is a demonstration for developement of future instruments.

Task

This Master thesis continuous that work and aims to improve the emissions fluxes further. The objectives are to use new spectroscopic measurements by MAMAP from the year 2011 and old data from 2007, and external meteorological data, and from these, estimate CO_2 emission rates of two strong point sources. The parametre wind is crucial and plays a major role. New vertically high resolution model wind profiles are used to calculate the emission rates of the two point sources Jänschwalde and Schwarze Pumpe for 2011 which have not been published yet. Krings et al. (2013) have already used highly resolved wind profiles but only for methane and not for carbon dioxide sources. Furthermore, the new wind profiles are also applied to the same power plants but for the year 2007, which were published by Krings et al. (2011) only using coarse wind profiles. For that purpose, column-averaged dry air mole fractions of carbon dioxide (XCO_2) have to be retrieved from the MAMAP measurements and then inverted with the aid of external meteorological data from the German Weather Service (DWD). Already developed retrieval and inversion algorithms can be used but have to be adjusted and modified to accommodate for the 2011 MAMAP data set and the new model data like higher resolved wind and new potential temperature data. It is expected that the new vertical profiles give new insights in the behavior of an emitted plume to the atmosphere and reduce the uncertainties of emission fluxes.

To achieve the new emission fluxes for the year 2011 it is necessary to test the retrieval algorithm on a new computer system and reproduce the results of Krings et al. (2011) for the year 2007. The next phase consists of analyzing the flight of the year 2011 in terms of flight parametres e.g., flight altitude or flight velocity, which are needed for the retrieval. Subsequently, the column-averaged dry air mole fractions of carbon dioxide are retrieved on basis of the MAMAP measurements and flight parametres for the year 2011, and compared to the year 2007 in terms of data quality. Based on these mole fractions and the new vertically highly resolved profiles from the DWD, the emission rates of the power plants Jänschwalde and Schwarze Pumpe for the overflight in 2007 and 2011 are retrieved. The emission rate results of the year 2007 with the new profiles are compared to the already published data (Krings et al., 2011) in order to assess the new approach and algorithm, respectively, which process the vertically highly resolved profiles.

Structure

This manuscript is arranged in five additional chapters. Chapter 2 introduces theoretical aspects which are essential to interpret the measurements of MAMAP correctly. It starts with a short introduction of the two greenhouse gases carbon dioxide and methane, their effect in the atmosphere and their sources. This is followed by a discussion of the stability of the lower atmosphere and the behavior of an emitted plume under different atmospheric conditions. Subsequently, it presents the infrared spectroscopy and explains the absorption features in the measured spectra due to methane and carbon dioxide which the intermediate quantity XCO_2 is derived from. Chapter 3 deals with the MAMAP instrument, describes the WFM-DOAS algorithm which converts the measured spectra, and introduces a new algorithm, which derives the mean wind speed on basis of the vertically highly resolved profiles from the German Weather Service and the location and behavior of the plume, respectively. The retrieval results column-averaged dry air mole fractions of CO_2 of Jänschwalde and Schwarze Pumpe for the years 2007 and 2011 are presented in the 4^{th} part. They are used to estimate the emission rates of the power plants in either year in chapter 5. Finally, a conclusion summarizes the findings.

Chapter 2

Theory

The following chapter establishes a solid foundation for upcoming parts of this work. It starts with a short discussion of the two gases carbon dioxide and methane, their importance for and influence on our climate system and how their amount in the atmosphere is altered by men. The second part deals with the dynamics and stability of the lower atmosphere and measures to determine them. This is necessary to understand where the emitted plume of a power plant is located and how it propagates in the atmosphere. The theory part is finally completed by a description of the interaction between radiation and molecules, in particular, with CO_2 and CH_4 molecules. The result of that interaction is measured and used to derive the emission rate of a specific point source e.g., a power plant.

2.1 The greenhouse gases CO_2 and CH_4

The earth's atmosphere has a dynamical structure and is part of the climate system. It interacts with the remaining spheres cryosphere, hydrosphere, lithosphere and biosphere. The main components of today's (dry) atmosphere are nitrogen ($78.08\,\%vol$[1]), oxygen ($20.05\,\%vol$), and the noble gas argon ($0.93\,vol\%$). The remaining $0.94\,\%vol$ spread over different trace gases like carbon dioxide, methane, hydrogen, nitrous oxide, ozone and CFC's (Roedel and Wagner, 2011).
In contrast to the history of the planet, when the atmospheric composition changed strongly, it is rather stable nowadays or at least in the time frame we are interested in. The main constituents nitrogen, oxygen and argon are spatially and temporally quite constant, whereas some trace gases show a high variability as well as water vapour which can account for up to $5\,\%vol$ (Wallace and Hobbs, 2006). In terms of climate, the subgroup greenhouse gases (tab. 2.1) plays an important role. Although, their

[1] $\%vol$ = volume percent

contribution to the total amount is small, only some ppm[2], ppb[3] or ppt[4], they determine the properties of the atmosphere to a large degree due to absorption of infrared radiation emitted by the earth's surface, which would leave the planet otherwise.

gas	**amount in 2005**	**RF** $\left[\mathrm{W/m^2}\right]$	**GWP for** 100 **yr** [ ]
CO_2	(379 ± 0.65)ppm	1.66 ± 0.17	1
CH_4	(1774 ± 1.8)ppb	0.48 ± 0.05	25
N_2O	(319 ± 0.12)ppt	0.16 ± 0.02	298
Halocarbons	—	0.34 ± 0.03	$5 - 14800$

Table 2.1: Depicted are the mole fractions, radiative forcings (RF), and the global warming potentials (GWP) for a time frame of 100 years for the important greenhouse gases carbon dioxide, methane and nitrous oxide and the group of the halocarbons which are influenced by human activities. The values for the RF are relative to the year 1750. For further explanations of RF and GWP see text. There is no single value for the amount of halocarbons in 2005 because there are many different species, and its GWP represents the range of values for the different types (data is based on Forster et al. (2007)).

On the one hand, greenhouse gases are important because they cause the natural greenhouse effect, which has increased the planet's temperature by approx. $33°C$ to today's temperature of $14°C$ (Jones et al.) and provides a habitable environment. To this effect, the natural greenhouse gas water vapour contributes 62 % (Roedel and Wagner, 2011) but its amount cannot be influence directly by men as it is possible and happening for CO_2 or CH_4. On the other hand, human activities have been increasing and still are increasing the amount of certain greenhouse gases further and, thus, causing an anthropogenic climate change.
To quantify the influence of different gases on the energy balance of the earth, the radiative forcing (RF) is used. It describes how the energy balance of incoming solar radiation and outgoing infrared radiation is disturbed by the total amount of a specific gas in the atmosphere. Due to the strongest contributers carbon dioxide and methane, for example, additional $1.66\,{}^{W}/_{m^2}$ and $0,48\,{}^{W}/_{m^2}$ compared to pre-industrial times (1750) are not able to leave the earth (tab. 2.1).
The amount of heat which is trapped within the atmosphere by a certain amount of a greenhouse gas depends on its type and lifetime. To compare different greenhouse gases, the term global warming potential (GWP) has been introduced. It states how large the radiative efficiency of an injection of 1kg of a greenhouse gas in the atmosphere relative to the injection of the reference gas carbon dioxide (also 1kg) is. In order to take also into account the different lifetimes, both pulses are integrated over a certain time interval, usually, 20, 100 or 500 yr before taking the ratio. That means, CO_2 always has a GWP of 1 but e.g., CH_4 is 25 times and nitrous oxide even 298 times more effective

[2]ppm = parts per million
[3]ppb = parts per billion
[4]ppm = parts per trillion

than CO_2 over a period of 100 yr (also compare to tab. 2.1).
From tab. 2.1, it can also be seen that CO_2 and CH_4 are the two most important anthropogenic greenhouse gases which concentrations have been increased from 278 ppm and 715 ppb in pre-industrial times (around 1750) to 379 ppm and 1774 ppb in 2005 (also compare to fig. 2.1), respectively. The steady increase after 1750 has been attributed to the industrialization and, thus, the combustion of fossil fuels.

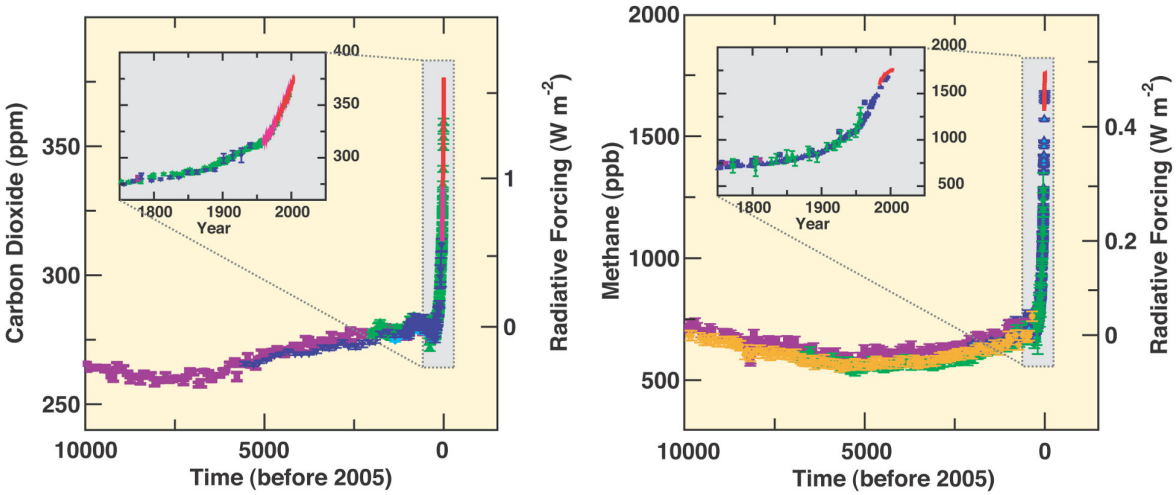

Figure 2.1: Shown is the temporal evolution of the amount of carbon dioxide in ppm (left panel) and methane in ppb (right panel) in our atmosphere over the last 10000 years, and over the last 255 years (insert boxes) before 2005. The coloured symbols correspond to different studies of different ice cores, whereas the red crosses are atmospheric measurements. Additionally, the radiative forcing for each gas relative to 1750 is depicted on the right axis (IPCC-SPM, 2007).

Their sources can be divided in natural and anthropogenic ones. In case of CO_2, most of the emissions originate from anthropogenic sources.

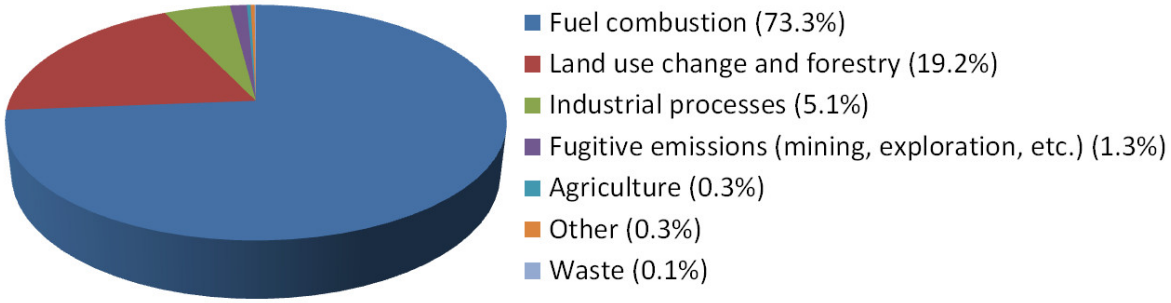

Figure 2.2: The pie chart depicts the contribution of the different types of sources to the total CO_2 emission of $\sim 36000\,{}^{TgCO_2}/_{yr}$ in 2005[5].

In 2005, the total output[5] was $\sim 36000\,{}^{TgCO_2}/_{yr}$, whereas almost three-quarter (compare

[5]Source: EC-JRC/PBL. EDGAR version 4.2., http://edgar.jrc.ec.europa.eu/, 2011

to fig. 2.2) were produced by fossil fuel combustion and 41.9 % of these three-quarter were emitted by public electricity and heat production facilities like power plants.
For CH_4, the total emission of 503 $^{TgCH_4}/_{yr}$ splits in anthropogenic (71.2 %) and natural (28.8 %) sources (Wuebbles and Hayhoe, 2002). It consists of point sources like waste disposal (responsible for 12.1 % of the total emissions), biomass burning (9.9 %) or coal mining(9.1 %) as well as of areal extended sources as wetlands (19.9 %), ruminants (16.1 %) or rice cultivation (11.9 %) (see fig. 2.3).

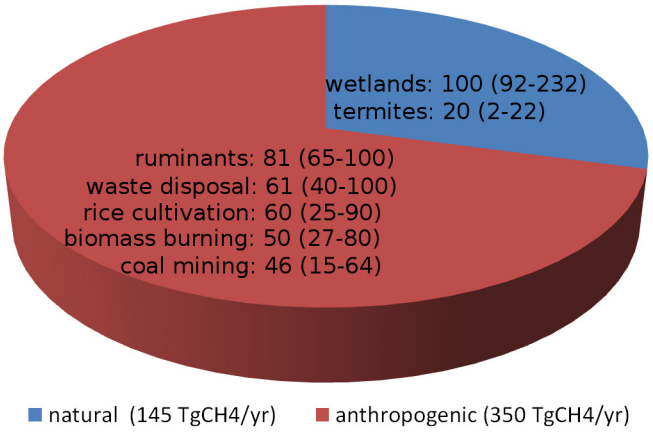

Figure 2.3: The pie chart shows the amount of emitted CH_4 by natural (blue) and anthropogenic (red) sources. Furthermore, the major contributors to both types and their range of values given in the literature are also added. All numbers are in $^{TgCH_4}/_{yr}$ (Wuebbles and Hayhoe, 2002).

2.2 Dynamics and stability of the lower atmosphere

The stability of the atmosphere is an important property, which influences the behavior of the plume after it has been emitted by a power plant. This knowledge has also an influence on the inversion later yielding the emission rate estimates of a specific source. Therefore, the first part of this chapter introduces the general structure of the atmosphere and properties which can be used to describe it. Next, the methods are presented that give an idea about the stability and special kinds of stratifications for the lower atmosphere are shown.
Most parts are based on the common textbooks Seinfeld and Pandis (2006), Wallace and Hobbs (2006), Masters and Ela (2008) and Roedel and Wagner (2011) related to the structure of the atmosphere, its stability and the governing quantities.

2.2.1 General structure of the atmosphere

An important parametre describing the atmosphere is the pressure p and its change with altitude. It can be described by assuming a thin horizontal slab of air with a mass of $\rho g dz$. The pressure at the bottom of this slab is p and on top is $p + dp$. That means, in equilibrium, the upwards, negative pressure change $-dp$ is equal to the downwards one exerted by the mass of the air slab:

$$dp = -\rho * g * dz \tag{2.1}$$

where ρ $\left[{}^{kg}/_{m^3}\right]$ is the density and g $\left[9.806\,{}^{m}/_{s}\right]$ the gravitational constant. Replacing ρ by the ideal gas equation leads to

$$dp = -\frac{M_d * g}{R * T} * p * dz \tag{2.2}$$

where M_d $[28.97\,{}^{g}/_{mol}]$ is the mole mass of dry air, p [hPa] the pressure, R $\left[8.315\,{}^{J}/_{K*mol}\right]$ the universal gas constant and T [K] the temperature. Integrating eq. 2.2 from sea level to top of the atmosphere assuming a constant temperature T with height gives the hydrostatic equation:

$$p = p_0 * \exp\left(-\frac{z}{z_0}\right) \tag{2.3}$$

with

$$z_0 = -\frac{R * T}{M_d * g} \tag{2.4}$$

where p_0 [1013 hPa] is the pressure at sea level. It can be seen that the pressure exponentially decreases with height z (also compare to fig. 2.4, blue line). Additionally, the quantity scale height z_0 has been introduced. It is the height at which pressure has decreased to ${}^{1}/_{e}$ in an hypothetical isothermal atmosphere. For the whole atmosphere, its value is approx. 8 km.
The scale height can also be calculated only for specific constituents e.g., argon (5.98 km), molecular oxygen (7.48 km), molecular hydrogen (119.50 km) for a temperature of $0\,°C$ if the molar mass of dry air is replaced by the molar mass of the specific constituent. These considerations implies a separation of the different types of molecules in the atmosphere, which cannot be observed near the ground. The reasons are turbulent mixing and transport processes leading to a relatively well-mixed air mass below 100 km, also called homosphere. A separation firstly starts above 100 km in the heterosphere.

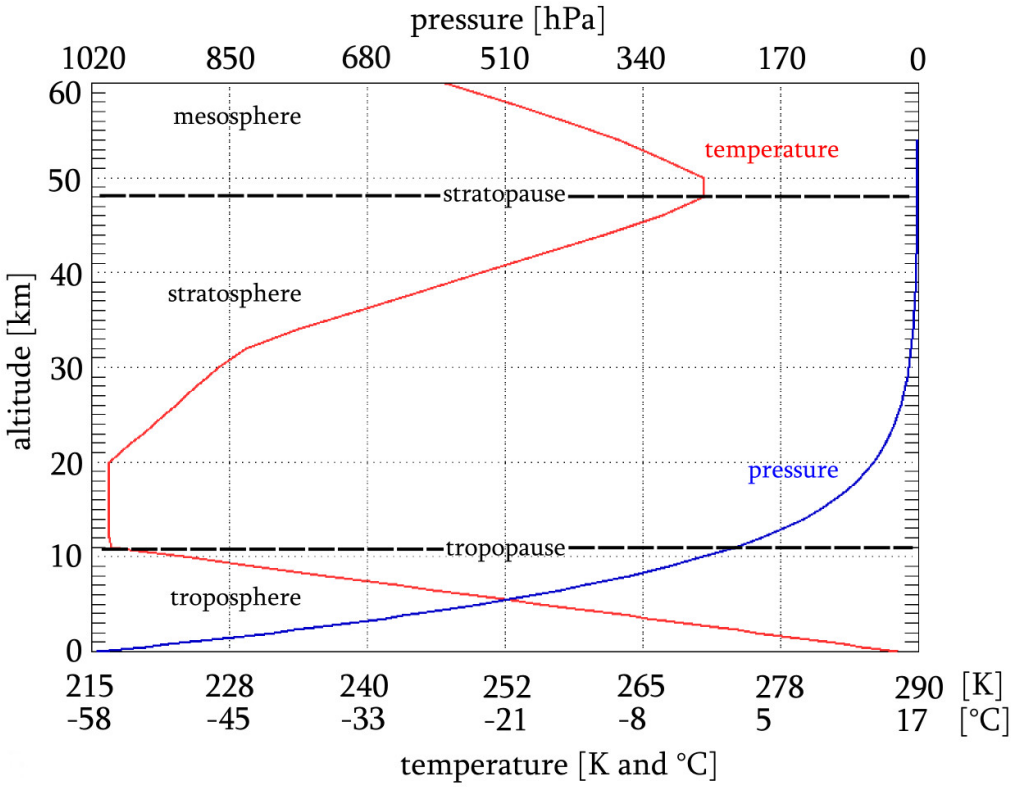

Figure 2.4: Shown is the vertical structure of the earth's atmosphere till a height of 60 km and its classification based on temperature. The temperature is given in K and °C. The profile represents a US standard atmosphere in temperate latitudes. Additionally the pressure in terms of altitude is depicted.

The atmosphere can further be divided by the temperature distribution. It consists of three main heating layers located at the ground, at around 50 km and above 90 km. Starting at sea level, the sun radiation is absorbed by the surface and heats the lowest part of the atmosphere. These heated air parcels rises because their density is lower than that of the surrounding air. While they are rising, their volume is increasing and the air parcels are cooling again if the exchange of heat with the surrounding air is negligible. In a first approximation, this assumption is true and is called an adiabatic process. The mechanism explains the cooling of the troposphere with altitude (fig. 2.4, red line) up to 10 km to 13 km in the temperate latitudes and and around 18 km in the tropics. The minimum temperature of around $-55\,^\circ$ and $-80\,^\circ C$, respectively, is reached in the tropopause. Furthermore, nearly all water vapour in the atmosphere is trapped below the tropopause because it cannot penetrate it. That leads to an additional heat sink due to emission of infrared radiation at top of this water vapour sphere. In the following layer, the stratosphere, the temperature increases again. This second heating source is characterized by ozone, which is built due to the photolysis of oxygen molecules. It absorbs UV-radiation and is destroyed again. As by-product, heat is produced reaching a maximum of $0\,^\circ C$ at an altitude of 50 km. This heating layer is also responsible for the

temperature inversion around 10 km limiting weather activities to the troposphere. The ascent of the air parcels heated at the ground is stopped at the tropopause because the parcel is colder and denser than the surrounding air. That is also the reason for the slow exchange of air masses between troposphere and stratosphere, which takes one to two years (Roedel and Wagner, 2011, p. 147). The stratopause follows another cooling layer, the mesosphere, and the mesopause at around 80 km with $-80\,°C$. Above 80 km oxygen molecules absorb UV-radiation again but are destroyed leading to a strong increase in temperature with altitude.

Laps rates

As this study is about pollutants emitted near the surface, a closer look to the troposphere is needed.
The general rate of decrease in temperature with height is between 5 and $10\,{}^{K}/_{km}$, and can be calculated on basis of the first law of thermodynamics (Seinfeld and Pandis (2006, pp. 722) and Roedel and Wagner (2011, pp. 72)). Assuming only dry air without any water vapour in the atmosphere, yields the dry adiabatic laps rate Γ_d:

$$\Gamma_d = -\left(\frac{dT}{dz}\right) = \frac{g}{c_p} \approx 1\,\frac{K}{100m} \tag{2.5}$$

where c_p $\left[1.005\,{}^{J}/_{kg*K}\right]$ is the specific heat at constant pressure of dry air per unit mass. Γ_d is defined as the negative change in temperature with altitude and using numbers for g and c_p gives $9.76\,{}^{K}/_{km}$. That means, the temperature decreases by approx. $10\,{}^{K}/_{km}$ in a dry atmosphere. Also considering water vapour with a specific humidity of 0.01, which must not condense out, would decrease the value by only 0.86% (Roedel and Wagner, 2011, p. 75).
In case of condensation, additional energy (latent heat) is available, which slows down the decrease in temperature. The new quantity is called saturated adiabatic laps rate Γ_s:

$$\Gamma_s = -\left(\frac{dT}{dz}\right) \approx 0.5\,\frac{K}{100m} \tag{2.6}$$

For temperatures between $0\,°C$ and $10\,°C$ its value is $5\,{}^{\mathrm{K}}/_{\mathrm{km}}$ and, thus, only half of the dry adiabatic laps rate Γ_d.
These are theoretical laps rates whereas γ is the actual laps rate of the atmosphere based on the real temperature profiles.

Potential temperature

In terms of temperature, a further definition is possible, which considers both thermal/inner and potential energy of an air parcel. In other words, this quantity, the potential temperature θ, is the temperature an parcel would have, if it is brought to a pressure p_0 of 1013 hPa at sea level:

$$\theta = T * \left(\frac{p_0}{p}\right)^{\frac{R_d}{c_p}} \tag{2.7}$$

where T [K] is the temperature of the air parcel at pressure p [hPa], R_d $\left[287.058\,{}^{J}/_{kg*K}\right]$ is the specific gas constant of dry air $\left(R_d = {}^{R}/_{M_d}\right)$ and the term ${}^{R_d}/_{c_p}$ has the value 0.286 for dry air. Potential temperature is a conservative quantity which remains constant in case of an adiabatic shift of an air parcel. Its change with height (Roedel and Wagner, 2011, p. 76) is given by

$$\frac{d\theta}{dz} = \frac{\theta}{T} * (\Gamma_d - \gamma) \tag{2.8}$$

Eq. 2.8 implies that the potential temperature changes even if the actual laps rate γ in the atmosphere is $0\,{}^{K}/_{km}$. This behavior is used to describe the stability in the next part.

2.2.2 Stability criteria and different types of layering

On basis of previous obtained quantities potential temperature, dry adiabatic, saturated adiabatic and actual laps rate, the stability of the atmosphere can be estimated. Therefore, the response of an air parcel is investigated when it is vertically disturbed. Disturbed means, the parcel is lifted or lowered by a certain distance $\pm\Delta z$ from its initial location z whereby its temperature changes due to the dry or saturated adiabatic laps rate. Subsequently, this change is compared to the real/actual laps rate in the atmosphere.
If there is a sunny day without clouds, the actual laps rate γ can be compared to the dry adiabatic laps rate Γ_d. Fig. 2.5 depicts two possible cases.
In the left panel (fig. 2.5a), the laps rate of the real atmosphere γ is smaller than of the dry adiabatic laps rate Γ_d and, thus, of the air parcel. That means, if the air parcel is lifted to a certain altitude $z + \Delta z$, its temperature will drop faster than that of the surrounding air. Therefore, also its density is higher than that of the surrounding air an it will subside to its initial position. If the air parcel is lowered, its temperature is

higher than that of the surrounding air, thus, its density is lower and it will rise to its starting point. In this case, the atmosphere is called stable, because an air parcel always returns to its source position.

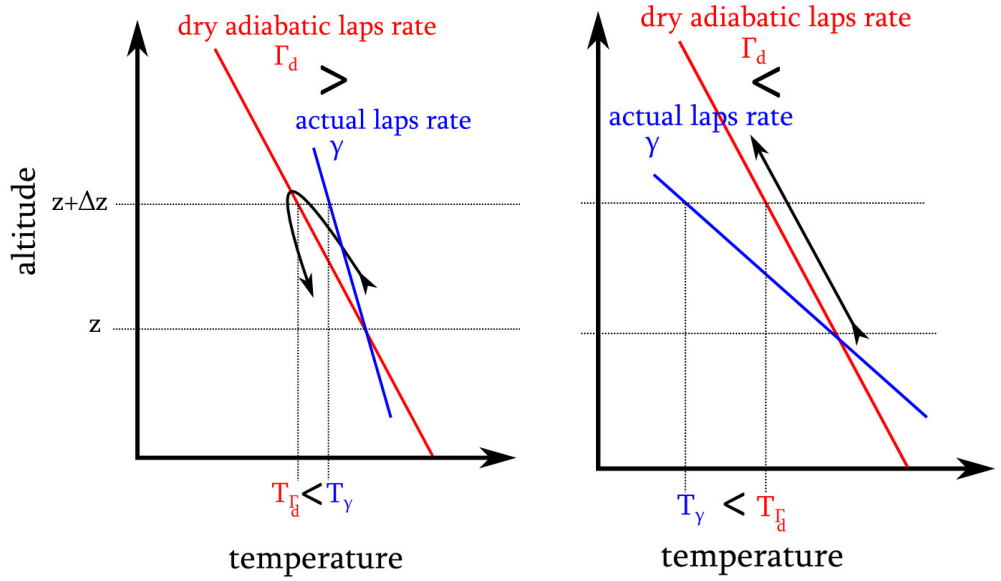

(a) Air parcel is lifted by Δz but returns to its initial altitude z because its temperature T_{Γ_d} rises slower than that of the surrounding air T_γ ($\gamma < \Gamma_d \Rightarrow$ stable and ${}^{d\theta}/_{dz} > 0$).

(b) Air parcel is again lifted by Δz but the ascent is accelerating because its temperature T_{Γ_d} rises faster than that of the surrounding air T_γ ($\gamma > \Gamma_d \Rightarrow$ unstable and ${}^{d\theta}/_{dz} < 0$).

Figure 2.5: Shown are the behavior of a vertically displaced air parcel in a dry sub- (a) and superadiabatic (b) atmosphere. The x-axis represents temperature and the y-axis altitude in arbitrary units.

The second possibility (fig. 2.5b) is, that the laps rate of the real atmosphere is larger than of the dry adiabatic laps rate and of the air parcel, respectively. If the air parcel rises, its temperature increases faster than the temperature of the surrounding air and also the parcel's density is lower than the density of the surrounding air. This leads to a further buoyancy effect and the air parcel shoots over. The same is true if the parcel is lowered. Its temperature increases slower than that of the surrounding air and, thus, its density is always higher, which intensify the dropping. In this case, the atmosphere is called unstable because the air parcel does not return to its initial location.
In a third possibility, the displaced air parcel stays exactly in the altitude where it has been put because its temperature and density is equal to the temperature and density of the surrounding air due to the same laps rates.
These laps rates can also be related to potential temperature using eq. 2.8. A neutral atmosphere, where the actual and the dry adiabatic laps rate are equal would correspond to an constant potential temperature with height, whereas a larger dry adiabatic laps rate would lead to an increase in potential temperature with height (stable), and a

smaller one to a decrease with height (unstable). These assumptions are only valid in an atmosphere where no condensation happens and summarized in tab. 2.2.

γ	$<$	Γ_d	stable	$^{d\theta}/_{dz} > 0$
γ	$=$	Γ_d	neutral	$^{d\theta}/_{dz} = 0$
γ	$>$	Γ_d	unstable	$^{d\theta}/_{dz} < 0$

Table 2.2: The table relates the possible stabilities of the atmosphere depending on its actual laps rate γ providing an air parcel follows the dry adiabatic laps rate Γ_d to the potential temperature change with altitude.

If water condenses out, there is an additional area called conditionally stable situated between absolutely unstable and absolutely stable. The lapse rate in that area depends on the level of saturation of the parcel. This case plays only a minor role for this thesis because, until now, measurements can only be taken under cloud free conditions and, thus, no condensation occurs.
Under specific conditions, parts of the atmosphere can reach a very high stability $\left(\gamma > 0 \text{ or } {}^{d\theta}/_{dz} >> 0\right)$. This layer is then called inversion and can hardly be penetrated by pollutants emitted below it. One example is the radiation inversion (Masters and Ela, 2008, p. 444), usually observable in the morning hours.

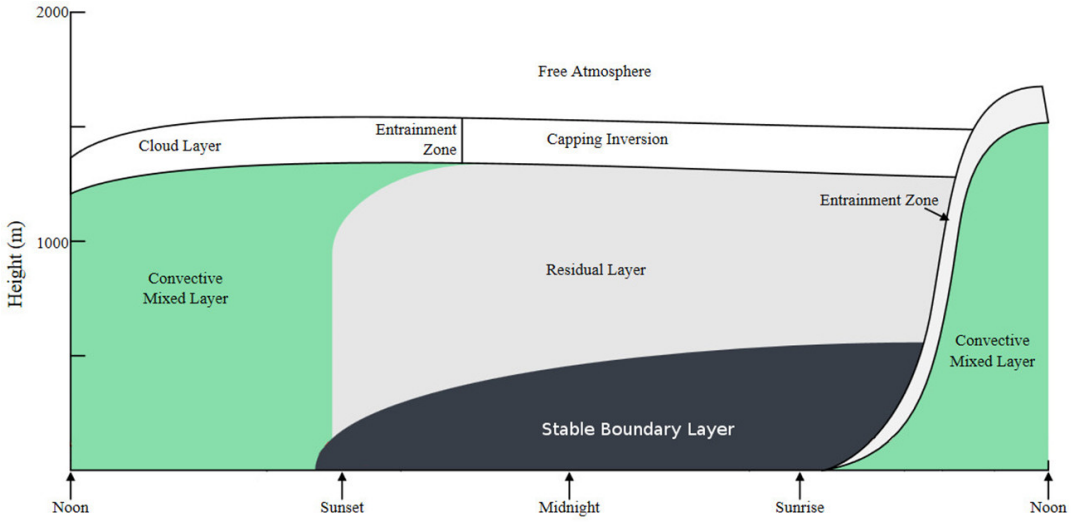

Figure 2.6: The plot schematically depicts the temporal evolution of the lower troposphere over one day. At 1500 m there is a capping layer separating the planetary boundary layer (PBL, below 1500 m) from the free troposphere (1500 m up to the tropopause height) during day and night. The planetary boundary layer is usually well-mixed during the day because of solar heating and the resulting convection (convective mixed layer). Starting at sunset, a stable boundary layer develops during night because of a radiative cooling of the surface but vanishes some hours after sunrise (modified after http://upload.wikimedia.org/wikipedia/commons/f/f1/Atmospheric_boundary_layer.svg, June 2013, based on Stull (1988)).

Fig. 2.6 shows such an inversion leading to a stable boundary layer (here: till 500 m). This kind is triggered by radiation. That means, the surface radiates more energy than it receives e.g., by the sun. This leads to a cooling of the surface and also to a cooling of the air mass above that surface. The air mass or parcel is now colder than the surrounding air and cannot ascend and stays on the ground. This kind of inversion can occur and develop during night when no sun is available to compensate for the lost energy. As soon as the sun rises, it penetrates the cold layer, and heats the ground which heats the cold air mass above. The cold air warms and rises until the inversion vanishes completely. The depth of such a cold surface layer mainly depends on the amount of lost energy during the night but it is usually between 500 m and 1500 m. Additionally, it needs to be calm because wind leads to turbulences near the surface and prohibit the development of an inversion layer. Usually, it is thinner in winter or during the night than in summer or during day because no energy is available, which can expand and, finally, dissolve the layer.
A second important type is the subsidence inversion (Masters and Ela, 2008, p. 445). It develops in high pressure systems when air is sinking. During this ascent, the air is compressed and heated adiabatically and becomes warmer than the air near the surface. It can achieve a thickness from several hundred metres to several thousands metres above the surface and can also be the boarder for the capping layer marked in fig. 2.6 around 1500 m. In this case, the radiation inversion/stable boundary layer can develop beneath a subsidence inversion. A second opportunity would be, they coincide.
The characteristic of an inversion is, that any pollutant which is released between the surface and that layer, is trapped, reflected back to the surface and might get well-mixed after some time with the surrounding air (compare to fig. 2.7a). But this is only an extreme case for a very stable layering. Its behavior might be different in a stable, neutral or unstable environment. Fig. 2.7b, 2.7c and 2.7d compare theses cases. In a stable and neutral atmosphere, the propagation is symmetrical whereas the plume diverges faster in the neutral one. In an unstable atmosphere, it is moving up and down producing something like a loop.
The behavior of a plume e.g. how much it spreads or whether it is trapped between two altitudes is later derived from vertical potential temperature and wind profiles. This knowledge of the vertical distribution of the plume will then be used in the inversion process to estimate the emission rate of a specific power plant.

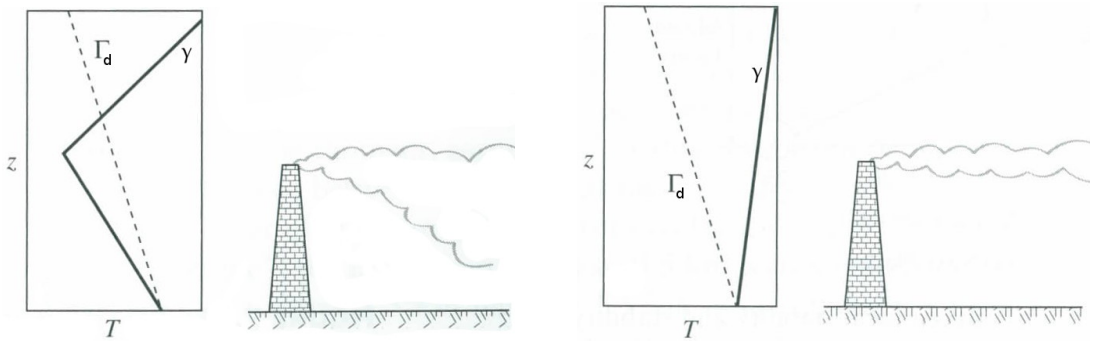

(a) Inversion leading to fumigation. **(b)** Stable atmosphere leading to fanning.

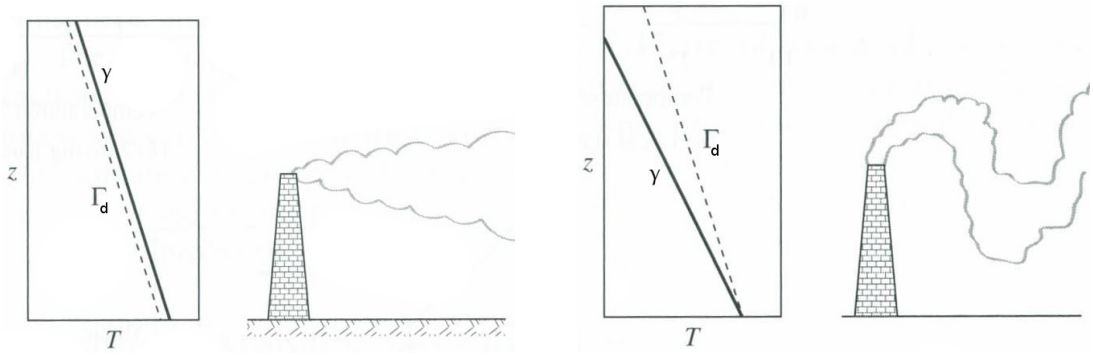

(c) Neutral atmosphere leading to conning. **(d)** Unstable atmosphere leading to looping.

Figure 2.7: The four sketches represent possible developments of a plume emitted at certain height by a power plant under different atmospheric conditions (inversion (a), stable (b), neutral (c), unstable (d)). The left plots always show the vertical profile of the dry adiabatic laps rate Γ_d (dashed line) and the actual laps rate γ (solid line). On the right sides, the response of the plume to the different conditions is shown (modified after Masters and Ela (2008)).

2.3 Radiative transfer in the short wave infrared region

The used instrument measures radiation of the sun which has been modified by the earth's atmosphere. Therefore, it is essential to know the different types of radiation and how they interact with air molecules or particles.
In the beginning, basics of radiation, its interaction with matter and the available types of radiation in the earth's atmosphere are described. The next section focuses then on the physical background which is used to explain the behavior of carbon dioxide and methane in the short wave infrared (SWIR) region around 1640 nm.
The following parts are based on the common text books Haken and Wolf (2006), Banwell and Kreiner (1999), Liou (2002) and Bohren and Clothiaux (2006) dealing with infrared spectroscopy and related fields.

2.3.1 Fundamental basics

Radiation corresponds to electromagnetic waves with a certain energy. They cover the very high energetic gamma rays on one end and the low energetic radio waves one the other end. The energy E is usually described in terms of electron volt[6] and is given by the wavelength λ, frequency ν or wavenumber $\tilde{\nu}$:

$$E = \frac{hc}{\lambda} = h\nu = hc\tilde{\nu} \tag{2.9}$$

where h is Planck's constant[7] and c is the speed of light in vacuum[8]. Tab. 2.3 gives a short overview about different types of electromagnetic waves and their properties, and fig. 2.8 depicts the solar spectrum on top of the earth's atmosphere and after it has reached the surface. The difference between both spectra are due to interactions of photons with the components of the atmosphere e.g., gases and particles.

gamma-rays	**x-rays**	**ultra-violet**	**visible**	**infrared**	**micro-waves**	**radio-waves**
$0.01 - 0.1$	$0.1 - 10$	$10 - 400$	$400 - 700$	$700 - 10^5$	$10^5 - 10^9$	$10^9 - 10^{13}$

Table 2.3: The table depicts one possibility of dividing the electromagnetic waves in regimes as they are suggested in the literature. The regions are given in nm.

The main processes are absorption, emission, and different types of scattering. All process but some types of scattering change the energy state of a molecule or atom,

[6] $1\,\mathrm{eV} = 1.602 * 10^{-19}\,\mathrm{J}$
[7] $h = 6.625 * 10^{-34}\,\mathrm{Js}$
[8] $c = 2.998 * 10^{8}\,{}^{m}/_{s}$

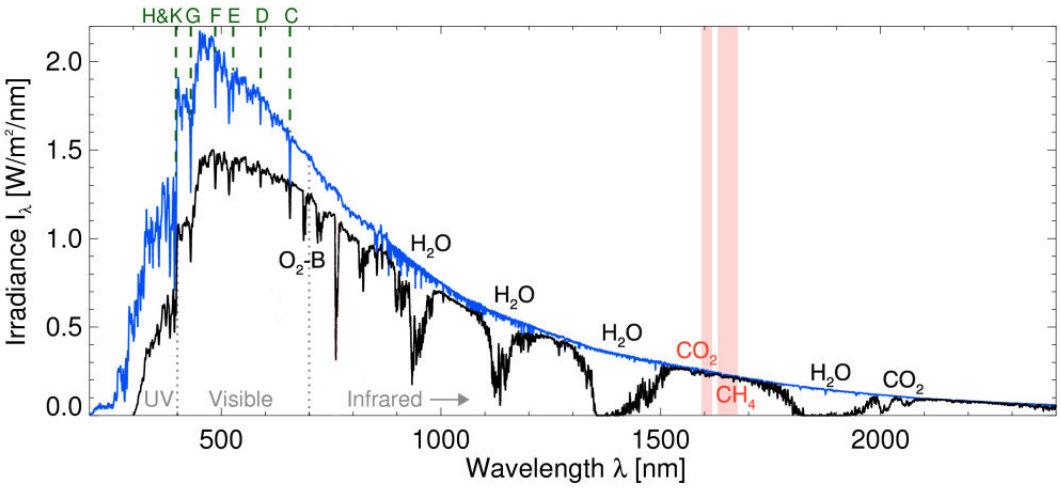

Figure 2.8: The plot shows the solar spectrum at top of the atmosphere (blue) and at the surface (black). The differences between both spectra are mainly due to absorption and scattering processes within the atmosphere by air molecules or particles. The solar spectrum itself already contains some strong absorption lines (H, K, G, ...) also called Fraunhofer lines, which originate in the sun's atmosphere. Additionally, the region under consideration around 1640 nm is emphasized, which contains absorption bands of carbon dioxide (CO_2) and methane (CH_4). Taken from Krings (2012).

whereas the type of change depends on the energy/wavelength of that photon and the type of molecule.
A molecule, and also an atom, have different energy states, which can be occupied. The ground state denotes the lowest amount of energy which can be realized. The energy difference between two states is given by

$$E' - E'' = h\nu \tag{2.10}$$

E' is the higher energy state, E'' is the lower energy state, and $h\nu$ is the energy difference, which is also the energy of one photon. In case of emission, the molecule returns to a lower energy state, and the energy $h\nu$ is emitted as a photon with frequency ν. That also means, a photon can only be absorbed if it has an energy which fits the energy difference between two states in an atom or molecule.
For absorption, different types of transitions exist to excite a molecule depending on the wavelength:

- **electronic transition**: in the visible, an electron is lifted to a higher state but is still part of the molecule.

- **vibrational transition**: in the infrared, atoms of a molecule vibrate with respect to each other.

- **rotational transition**: in the microwave region, the molecule rotates.

It is seen, that the highest energies are needed for electronic transitions and the lowest for rotational transitions:

$$E_{electronic} >> E_{vibration} >> E_{rotation} \tag{2.11}$$

In terms of a molecule, the total energy is given by the sum of the three different energies. The energy difference between two states can also be expressed in terms of spectral lines or wavenumber, used, especially, in infrared spectroscopy.

$$\tilde{\nu} = \Delta T + \Delta G + \Delta F \tag{2.12}$$

where ΔT, ΔG and ΔF represent the energy differences of the electronic, vibrational and rotational transition, respectively, divided by the term hc (compare to eq. 2.9).
In general, transitions are quantized, meaning only specific energy levels are available. In case of electronic transitions, this was first shown by Bohr (1913) who formulated the energy levels in an hydrogen atom which has one electron:

$$E_n = -\frac{R_H hc}{n^2}, n = 1, 2, 3, ... \tag{2.13}$$

where R_h is the Rydberg constant for hydrogen[9], and n is the discrete electronic quantum number describing the different energy states in a hydrogen atom. For rotational and vibrational transitions it is getting more complicated because they only occur in molecules with more than one atom and can combine to one transition called rotational-vibrational transition.

2.3.2 Infrared spectroscopy

For the spectroscopic measurements taken by MAMAP, absorption features around 1640 nm are considered. Therefore, it is expected to observe combined rotational-vibrational transitions. Hence, a short introduction of the pure rotational transitions, which actually occurs in the microwave region, the pure vibrational transition, occurring in the infrared, and finally, the combination of both are given.

[9] $R_h = 1.097 * 10^5 \, {}^1/_{cm}$

Rotational transitions

A rotational transition requires at least a diatomic molecule which has a permanent dipole moment[10]. The dipole moment can also be induced by the a rotation or vibration. For an observer, the dipole moment changes due to rotation around the centre of mass and can interact with electromagnetic waves. A photon is absorbed if wave and rotation have the same energy.

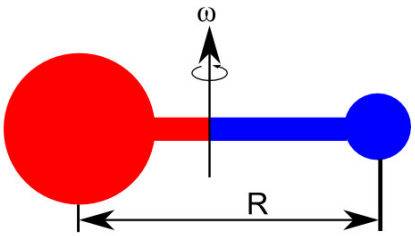

Figure 2.9: Shown is the rotation of a diatomic molecule. Both atoms are connected by a fixed bond. R is the distance between both atoms.

A diatomic molecule can be approximated by a dumbbell (fig. 2.9). The atoms are connected by a fixed bond and rotate around their centre of gravity. The energy of this rotation can be calculated solving Schroedinger's equation and is given by

$$E_{rot} = \frac{\hbar^2}{2\theta} J(J+1), J = 0, 1, 2, 3, ... \tag{2.14}$$

where θ is the moment of inertia of the system, $\hbar$ is the reduced Planck constant[11], and J is the rotational quantum number only taking discrete numbers. As for electronic transitions, also the rotational energy is quantized and its zero-point energy ($J = 0$) cannot be zero. The higher J, the larger the rotational energy is. The energy can also be expressed as the term value:

$$F(J) = \frac{E_{rot}}{hc} = BJ(J+1), J = 0, 1, 2, 3, ... \tag{2.15}$$

where B is the rotation constant, which is connected to the momentum of inertia and characteristic for one type of molecule. The energy difference between two states is equal to the energy of a photon, whereby only transitions with $\Delta J = \pm 1$ are allowed:

$$h\nu = E_{J+1} - E_J, J = 0, 1, 2, 3, ... \tag{2.16}$$

and the distance between two absorption lines in terms of wavenumber is given by

$$\tilde{\nu}_{J \leftarrow J+1} = F_{J+1} - F_J = 2B(J+1) \tag{2.17}$$

Eq. 2.17 is also used in spectroscopy. A rotational spectrum is measured and from the distance between two lines, one can determine the characteristic rotational constant for a type of gas.
The model used so far provides equidistant absorption lines (eq. 2.17). It assumes a rigid

[10] not observable for homonuclear diatomic molecules like H_2, N_2, and O_2
[11] $\hbar = \frac{h}{2\pi} = 1.055 * 10^{-34}$ Js

connection and hence, a constant distance R, between the two atoms of a molecule for all rotational energy states. That can be further expanded because the distance depends on J. The higher the rotational quantum number J, the larger also the centrifugal force between both atoms is, and the distance is increasing leading to a larger momentum of inertia and, therefore, affects the rotational constant and change the wavenumber (eq. 2.17).
The effect is rather small for pure rotational spectra but can be larger and important in combination with vibrations.

Vibrational transitions

As for rotational transitions, vibrational transitions can only be observed in molecules. Moreover the dipole moment must change due to a vibration. Assuming again a diatomic molecule but the atoms being connected by a spring. The dipole moment changes if the atoms vibrate with respect to each other because the distance changes and they can interact with an electromagnetic wave.
In the ground state, the distance between two atoms in a molecule is determined by the repulsive force due to the positive charge of the nuclei, and the attraction due to the chemical bound caused by their electrons. The molecule minimizes the total force so that they are in an equilibrium. The resulting distance is then called equilibrium distance R_e. In order to change R_e, energy needs to be put into or out off the system. The larger the deviation from R_e, the larger the necessary energy is.
For example, if a photon is absorbed, the atoms start vibrating around the equilibrium distance and the molecule is excited and has reached a higher energy state. The amount of energy needed for a certain deviation can be approximated by different 2 dimensional potentials which are used to solve Schroedinger's equation. Eq. 2.18 depicts the solution for a Morse potential (compare fig. 2.10) which describes an inharmonic oscillator.

$$E_{vib}(v) = \hbar\omega_e\left(v+\frac{1}{2}\right) - x_e\hbar\omega_e\left(v+\frac{1}{2}\right)^2 \tag{2.18}$$

where ω_e is the vibration constant, x_e is the anharmonicity constant, and v[12] is the vibrational quantum number. Or in terms of the term value:

$$G_v = \tilde{\nu}_e\left(v+\frac{1}{2}\right) - x_e\tilde{\nu}_e\left(v+\frac{1}{2}\right)^2 \tag{2.19}$$

with

$$x_e = \frac{\hbar\omega_e}{4D_e} \tag{2.20}$$

[12]vibrational quantum number v is not to be confused with the frequency ν or the wavenumber $\tilde{\nu}$

and

$$\omega_e = \frac{\hbar\omega}{hc} \tag{2.21}$$

where D_e is the total energy necessary to dissociate the molecule. Fig. 2.10 depicts such a Morse potential with different vibrational states. As for rotational transitions, the zero-point energy at ground state ($v = 0$) is not 0 eV and the selection rules are $\Delta v = \pm 1, \pm 2, \pm 3, ...$, where $\Delta v = \pm 2, \pm 3, ...$ are overtones of the basic oscillation $\Delta v = \pm 1$.

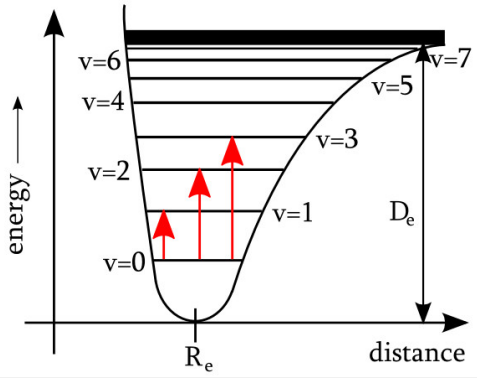

Figure 2.10: The sketch shows the Morse potential for the ground state of a molecule (electronic quantum number $n = 0$) and three vibrational transitions: the basic oscillation ($\Delta v = +1$) and two overtones ($\Delta v = +2, +3$). Additionally, the dissociation energy D_e is also depicted. The distance between two vibrational energy states converges for larger v as a result of the empirical Morse potential. For large v, single states are not distinguishable anymore and go over to a continuum at the energy D_e. The ground state has an energy of $\frac{1}{2}\hbar\omega_e(1 - \frac{1}{2}x_e)$.

Rotational-vibrational transitions

As already mentioned, vibrational and rotational transitions regularly occur together. Each vibrational state has many corresponding rotational states. As a first approximation, it can be assumed that the transitions are not coupled (Born-Oppenheimer approximation) and can be depicted by a sum:

$$\begin{aligned} E(v, J) &= E_{vib}(v) + E_{rot}(J) \\ &= \hbar\omega_e\left(v + \frac{1}{2}\right) - x_e\hbar\omega_e\left(v + \frac{1}{2}\right)^2 + hcBJ(J+1) - hcD_vJ^2(J+1)^2 \end{aligned} \tag{2.22}$$

The first two terms on the right sight, describe the vibrational energy of an inharmonic oscillator and the last two terms describes the rotational energy of a flexible rotator[13]

[13] expansion of the rigid dumbbell model

with D_v is the expansion centrifugal constant. D_v considers the effect that the momentum of inertia is increasing for increasing rotational quantum numbers J but, in the following, it is assumed to be small and negligible.
Using the notation from the first section, it follows for a transition in terms of wavenumber from eq. 2.22:

$$\tilde{\nu} = \frac{1}{hc}\big(E(v', J') - E(v'', J'')\big) \tag{2.23}$$

with the selection rules $\Delta J = \pm 1$ and $\Delta v = \pm 1(, \pm 2, \pm 3)$, whereas a transition of $\Delta v = \pm 1$ without a change in ΔJ, is only allowed for special cases and depends on the symmetry of the molecule. Fig. 2.11 shows typical rotational-vibrational transitions for $v'' = 0$, $v' = 1$ and $\Delta J = \pm 1(, 0)$.

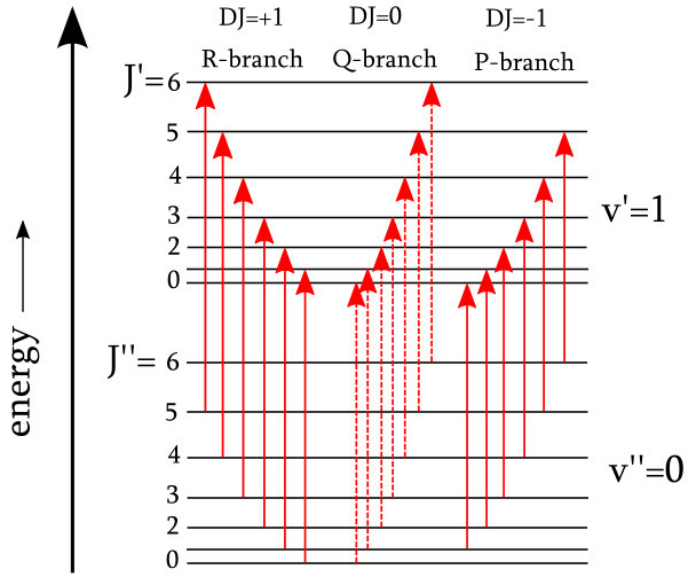

Figure 2.11: The sketch shows the branches occurring for rotational-vibrational transitions in the ground state of an atom (electronic quantum number $n = 0$). The P-branch belongs to the transitions $\Delta v = +1$, $\Delta J = -1$ and the R-branch belongs to the transition $\Delta v = 1$, $\Delta J = +1$. Furthermore, the unusual Q-branch for a pure vibrational transition ($\Delta v = +1$, $\Delta J = 0$) is depicted. Compare also the spectrum of carbon dioxide (P- and R-branch) and methane (P-, R- and Q-branch) around $1640nm$ in fig. 2.13. The distance of the rotational states diverges for increasing J because of the coupling of rotation and vibration.

For each $\Delta\nu$ two ΔJ with ± 1 are available, which give rise to two different branches. The P-branch is located on the more long wave side, and the R-branch is located on the more short wave side of the basic oscillation, which is usually not observed. The wavenumber of each absorption line in the two branches for $v + 1 \leftarrow v$ is given on basis of eq. 2.23 with the aid of a case discrimination:

- **P-branch**: $\Delta J = -1$; $J' = J$ and $J'' = J + 1$:

$$\nu_P = (v', v'') - 2B_{v''}(J+1) - (B_{v''} - B_{v'})J(J+1) \tag{2.24}$$

- **R-branch**: $\Delta J = +1$, $J' = J + 1$ and $J'' = J$:

$$\nu_R = (v', v'') + 2B_{v''}(J+1) - (B_{v''} - B_{v'})(J+1)(J+1) \tag{2.25}$$

The last term on the right side of both eq. 2.24 and 2.25 including $B_{v'}$ (rotational constant for $v = 1$) and $B_{v''}$ (rotational constant for $v = 0$), considers the interaction between rotation and vibration because they can actually not be separated. Any kind of vibration also influences the momentum of inertia and, therefore, the rotation constant B, whereas the effect of stretching the bond due to the centrifugal force itself, described by D_v, is much smaller.
This results in not equidistant absorption lines on both sides of the zero-point frequency (also compare to fig. 2.13). The P-branch converges and the R-branch diverges for larger rotational quantum numbers. Additionally, the transition for $\Delta v = \pm 1$ and $\Delta J = 0$ is called Q-branch and can usually not be observed in the rotational-vibrational spectrum. The CH_4 absorption spectrum around 1665 nm is an exception and shows all three branches.

Infrared absorption by carbon dioxide and methane around 1640nm

The previous section dealt with diatomic molecules, which have only one degree of freedom for oscillation and, hence, only one vibrational transition. The molecules CO_2 and CH_4, under consideration in this work, have three and five atoms, respectively. This allows different types of oscillations and also overtones/combinations of the basic oscillations.
Carbon dioxide is a linear molecule consisting of two oxygen and one carbon atom.

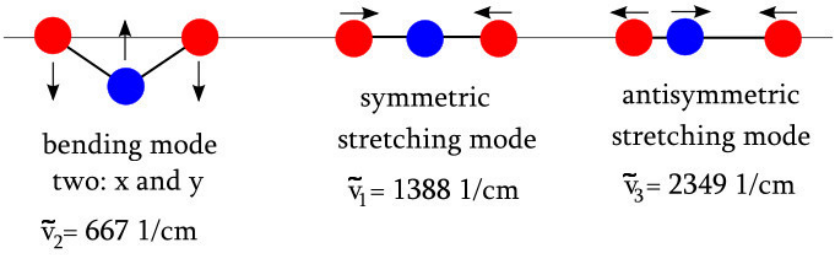

Figure 2.12: The sketches show the three different vibrational modes (bending mode, symmetric stretching mode and antisymmetric stretching mode) of a carbon dioxide molecule and their basic oscillations ($\tilde{\nu}_1 = 1388\,{}^1/_{cm}$, $\tilde{\nu}_2 = 667\,{}^1/_{cm}$ and $\tilde{\nu}_3 = 2349\,{}^1/_{cm}$)(Bohren and Clothiaux, 2006). The bending mode is doubly degenerated and can occur either in the x-y- or x-z-plane.

It has four degrees of freedom and can exert three different types of vibrations (bending vibration, asymmetric stretching vibration and symmetric stretching vibration) wheres the bending vibration is doubly degenerated. To be infrared active, the dipole moment has to change during vibration. That is only possible for the asymmetric stretching and the two bending vibrations but not for the symmetric stretching vibration because CO_2 has no dipole moment for its ground state and the geometry does not change for the symmetric stretching. The absorption band around 1605 nm shows the P- and R-branch of the rotational-vibrational transitions (fig. 2.13).

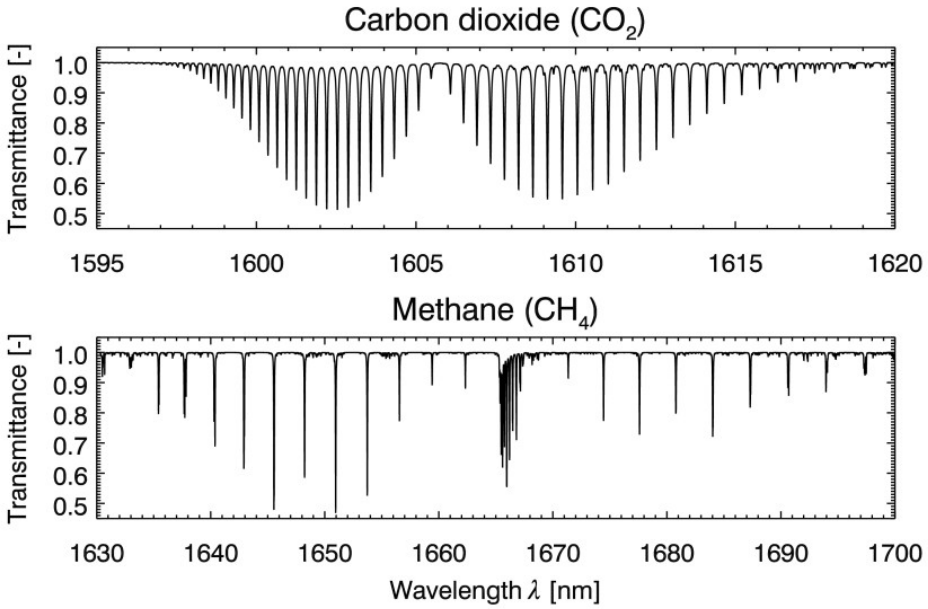

Figure 2.13: The two graphs depict the high resolution rotational-vibrational absorption spectra of carbon dioxide and methane around 1605 nm and 1665 nm, respectively, based on the HITRAN 2008 spectroscopic data base (Rothman et al., 2009). The R- and P-branch can be clearly seen in both spectra. Additionally, the methane spectra exhibits a Q-branch. Taken from Krings (2012).

Methane is a spherical molecule consisting of four hydrogen and one carbon atom. Hence, it can exert nine types of vibrations. They are based on the four basic oscillations symmetric stretching mode ($\tilde{\nu}_1 = 2917\,{}^1/_{cm}$), symmetric bending mode ($\tilde{\nu}_2 = 1533\,{}^1/_{cm}$, doubly degenerated), asymmetric stretching mode ($\tilde{\nu}_3 = 3019\,{}^1/_{cm}$, triply degenerated), and asymmetric bending mode ($\tilde{\nu}_4 = 1311\,{}^1/_{cm}$, triply degenerated)(Bohren and Clothiaux, 2006). It has no permanent dipole moment in its ground state and, therefore, no rotational transitions without vibrations. Furthermore, only the asymmetric modes ($\tilde{\nu}_3$ and $\tilde{\nu}_4$) are infrared active. The absorption features around 1665 nm originates from an overtone of the asymmetric stretching mode and also shows a Q-branch (fig. 2.13).
The rotational-vibrational absorption spectra depicted in fig. 2.13 is the basic physical feature, which is measured by MAMAP. However, the instrument cannot resolve each single line and combines them to bands as it will be discussed in the next chapter.

Chapter 3

Description of the instrument and the approach

In order to interpret the calculated atmospheric CO_2 and CH_4 amounts correctly and to obtain meaningful emission rates, it is necessary to understand how the basic physical property, solar radiance, is actually measured by the instrument and converted to the final quantity.
Therefore, the first part of this chapter presents the MAMAP instrument used in this study and describes improvements and modifications over the past years. The second part then deals with the algorithm which derives the important intermediate quantity atmospheric column-averaged dry air mole fraction. Finally, the Gaussian plume model is introduced, which is used to model the measured and retrieved column-averaged dry air mole fractions, and yields the final result, the emission rate of a certain target. To improve the accuracy of the inferred emission compared to previously published results, a method is presented based on new vertically highly resolved wind and potential temperature profiles.

3.1 The Methane Airborne MAPper (MAMAP)

The following two sections describe the main parts of the instrument and modifications between the flights in 2007 and 2011, and their influence on the measured spectra. Furthermore, the measurement geometry and the actually measured air masses are depicted.

3.1.1 Structure and signal handling

MAMAP is an airborne based measurement device, which records backscattered solar radiation from the surface. It was build in 2006 in cooperation with the Helmholtz

Centre Potsdam, German Research Centre for Geoscience (GFZ) and was extensively discussed by Gerilowski et al. (2011). It consists of two separate Falcon racks, each weighing approx. 120 kg, which can be installed on board typical research aircrafts like Dornier 228, Dassault Falcon, Cessna Caravan and Basler-DC3. Fig. 3.1a depicts both MAMAP racks, here, mounted in the Polar-5 (Balser-DC3) aircraft (fig. 3.1b). The left unit is called concomitant rack and contains the control system, recording devise and a battery. The right unit, the spectrometre rack, contains two spectrometres, one covering the absorption features of methane and carbon dioxide around 1640 nm (SWIR) and one covering the absorptions features of the O_2A-band around 760 nm (NIR). This Master thesis focuses on the information gained by measuring the absorption features of carbon dioxide and methane around 1640 nm and, thus, the NIR spectrometre is not further discussed in the following.

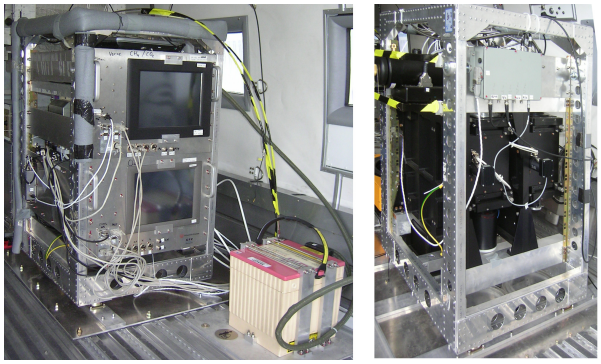

(a) The two MAMAP racks. Left panel: concomitant block. Right panel: spectrometre block. (photographs by Thomas Krings)

(b) The Polar-5 aircraft. (photograph by Anja Schönhardt)

Figure 3.1: The MAMAP system mounted in the aircraft Polar-5 of the Alfred-Wegener-Institute für Polar- und Meeresforschung in Bremerhaven.

In its original version, used for flights in 2007, the SWIR spectrometre had access to its own telescope. It allowed collection of radiation either from the zenith[1] or nadir[2] direction by switching a mirror (also compare fig. 3.3a), whereas only the nadir port was used. The incoming light was focused onto the entrance slit of the spectrometre by an optimized aspheric doublet lens (manufactured by ZEISS). Within the spectrometre, the radiation is reflected by the first mirror (collector), which produces a parallel light bundle, onto a grating. The grating decomposes the light into its spectral components, which are focused by a second mirror (collimator) on a 1-dimensional InGaAs detector. The grating with 600 $^{grooves}/_{mm}$ covers a spectral range of 93.3 nm at a spectral resolution of 0.82 nm around a centre wavelength of about 1640 nm and is able to screen both absorption bands of CO_2 and CH_4 simultaneously. The spectral resolution is not only a function of the grating but of the whole spectrometre setup, especially the entrance slit, and determines how the instrument displays the absorption features due to methane

[1] zenith = looking up
[2] nadir = looking down

and carbon dioxide (compare fig 2.13 and 3.2). It is defined by a line shape function with a certain FWHM[3] (here: 0.82 nm). The InGaAs detector is a linear modified array which is cooled by liquid nitrogen to −120 °C to minimize the dark current. It has a total length of 25.6 mm and 1024 pixels with a pixel pitch of 25 μm.

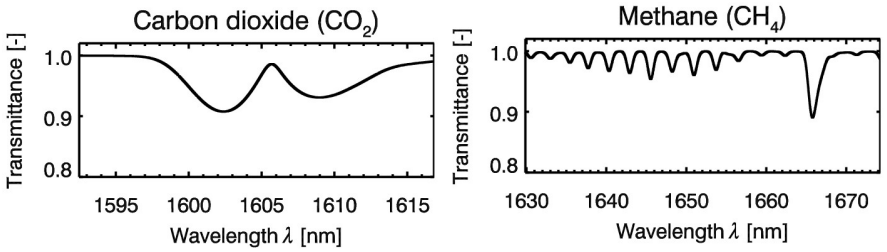

Figure 3.2: The two plots depict the rotational-vibrational absorption spectra of carbon dioxide and methane seen by MAMAP. The high resolution spectra from the previous section (fig. 2.13) have been convolved with the instrumental line shape function with a FWHM of 0.82 nm of the SWIR spectrometre. The single absorption lines of CO_2 combine to two bands, representing the R- and P-branch. For CH_4, also the strong Q-branch is observed. The absorption feature due to the single lines in the R- (and P-)branch can still be observed, whereas the used detector does not record photons with wavelengths larger than 1674 nm. Also compare to fig. 3.6 second row. (Provided by Thomas Krings)

From the intensity distribution along the detector, which represents the spectrum of one measurement, the amount of carbon dioxide and methane can be derived. This raw spectrum is also influenced by two effects originated in the sensor. Firstly, it contains an offset caused by the remaining dark current which cannot be completely removed by cooling the detector. It differs from pixel to pixel and is also not stable over time. To remove it, a dark spectrum is recorded regularly during measurements and subtracted from the signal. Additionally, parts of the spectrometre like the mirrors and grating or the lens in front of the telescope can imprint structures in the spectrum which affect the measurement. In contrast to the dark current, this influence is nearly constant and is removed by dividing the signal by the signal of a white light source, which is recorded once before each flight. This kind of normalization also removes sensitivity differences of the pixels.
Between the flights in 2007 and 2011 the instrument was modified. The aspheric doublet lens of the telescope was replaced by a spatial scrambler and a glass fibre (fig. 3.3b). The fibre allows a more flexible positioning of the racks because, in the past, the spectrometre rack had to be placed right above an aperture hole in the cabin. Using glass fibres and an external, seperate telescope, the rack can be mounted further away from the aperture hole. The distance is only limited by the length of the fibre. The second improvement, the spatial scrambler, addresses the quality of the measured spectra. Without scrambler, it could happen that the entrance slit of the spectrometre was not illuminated evenly because one part of the surface scene was bright (high albedo, e.g.,

[3]FWHM = full width at half maximum

soil) and the other part was dark (low albedo, e.g, water). This effect led to pseudo noise in the measured column-averaged dry air mole fractions of carbon dioxide (XCO_2). The improvement was already suggested by Gerilowski et al. (2011) and confirmed by Krings et al. (2013).

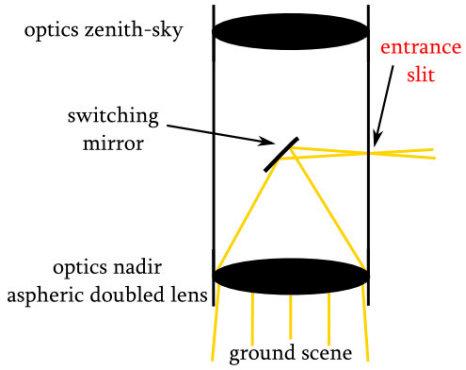

(a) Sketch of the old optics used in the flight 2007. Shown is the telescope with the aspheric doubled lens for the nadir mode, a normal lens for zenith-sky observation, and the switching mirror.

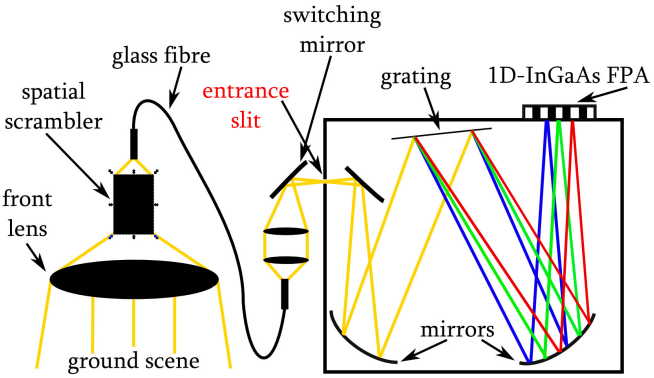

(b) Sketch of the modified optics used in the flights 2011 and the SWIR spectrometre.

Figure 3.3: The modified MAMAP system in terms of the SWIR channel and optics. The spectrometre itself had not changed, just the structure of the optics before the entrance slit (emphasized in red colour). The term ground scene represents the area seen by the instrument on the earth's surface.

3.1.2 Measurement geometry

It is important to know where the light comes from, which air mass is represented by a measurement, and where the absorption has taken place as already indicated by the ground scene in fig. 3.3. Fig. 3.4 depicts typical flight conditions of the MAMAP instrument. MAMAP is integrated into an aircraft and the telescope collects scattered radiation from the nadir direction. The sketch is only idealized and does not show any scattering within the atmosphere.
The sun radiation penetrates the whole atmosphere, is reflected by the surface and, then, gathered by the telescope at a certain altitude. The area on the surface, which is seen by the telescope, and from which light is collected, is defined by the aperture angle of the complete system. This field is also called instantaneous field of view (IFOV) and is given by cross track[4] $*$ along track[5] angle. In combination with the flight altitude, the size of the ground scene can be determined provided the aircraft would be in the air but not flying or moving. Normally, a combination of flight velocity and exposure time[6]

[4]angle perpendicular to flight direction
[5]angle in flight direction
[6]the time while the sensor is collecting light

determine the length of the ground scene in flight direction. In this case, the measured radiance is averaged over the distance which has been covered by the aircraft within the exposure time at a given flight velocity and altitude. The three parametres flight velocity, flight altitude and exposure time vary from flight to flight and consequently also the observed ground scene size. Moreover, one MAMAP measurement normally consists of 10 consecutive single readouts, called burst. This extends the ground scene size in flight direction further (compare to tab. 3.1). Additionally, the spatial scramble also changed the IFOV.

year of flight	**flight altitude [km]**	**flight velocity [km/h]**	**exposure time [ms]**	**ground scene size cross ∗ along [m ∗ m]**
2007	1.25	200	580	$29x33$
2011	1.54	200	980	$28x82$

Table 3.1: The table summarizes and compares parametres relevant for the modified ground scene size of the flight 2007 and 2011.

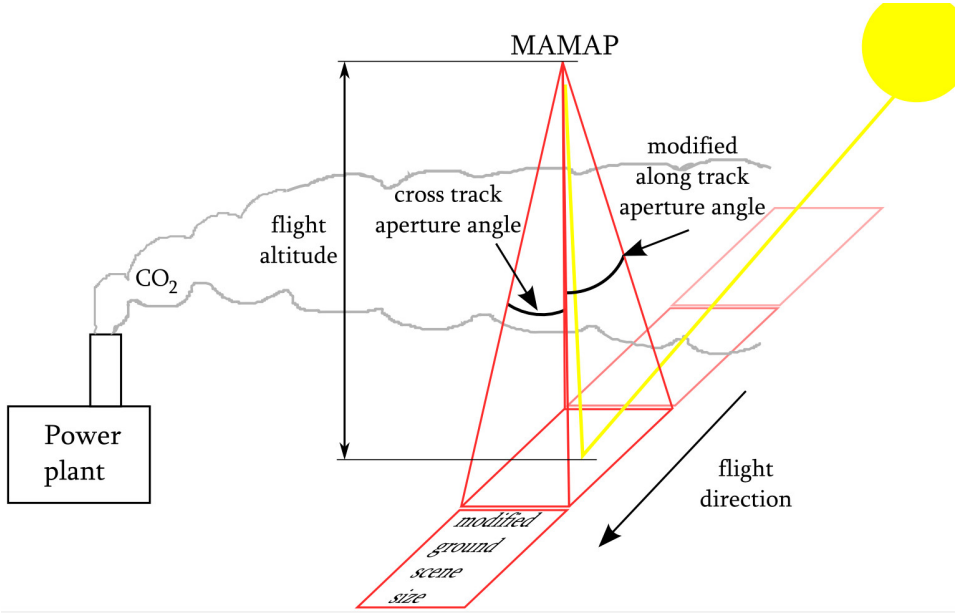

Figure 3.4: The sketch shows the usual observation geometry of the MAMAP instrument. The aircraft crosses the plume of a power plant nearly perpendicularly. While flying, the telescope of the instrument is continuously gathering reflected sun light from the ground. The modified ground scene size is indicated by red rectangles which are determined by the aperture angles of the instrument, flight velocity, flight altitude, exposure time of the sensor and number of summed up consecutive readouts. The light path is only an idealized case but indicates that not only the airmass right beneath the aircraft is measured, limited by the ground scene size, but also absorption features occurring outside of the pyramid along the light path.

3.2 The retrieval algorithm

This section is dedicated to the separation of the absorption features of methane and carbon dioxide which modify the measured solar backscattered radiation in order to derive the intermediate quantity column-averaged dry air mole fractions of CO_2.

3.2.1 Weighting Function Modified DOAS (WMF-DOAS)

The retrieval algorithm extracts the absorption features of carbon dioxide and methane from the measured spectra obtained by the MAMAP instrument. It uses a modeled spectrum and compares it to a measured spectrum. The modeled spectrum is then modified based on scaling atmospheric profiles e.g., of CO_2 and CH_4 (compare to fig. 3.5), until the difference between both spectra is minimal. The results are profile scaling factors (PSFs) describing an increase or decrease in the absorption strength of CO_2 and CH_4 along the light path compared to the previous assumed profiles for the modeled spectrum.
The weighting function modified (WFM) differential optical absorption spectroscopy (DOAS) algorithm (Buchwitz et al., 2000) was originally developed for the retrieval of trace gases and water vapour in the short wave infrared (SWIR) measured by the Scanning Imaging Absorption Spectrometer for Atmospheric CHartographY (SCIMACHY) (Burrows et al., 1995; Bovensmann et al., 1999) on board the Environmental Satellite (Envisat).
The main differences to the standard DOAS are that the DOAS method assumes a linear dependence of the absorption strength with concentration and an independence of absorption cross-sections[7] with altitude and, therefore, with temperature and pressure. These assumptions are only valid for weak absorbers in our atmosphere e.g., nitrogen dioxide (NO_2), sulfur dioxide(SO_2) or formaldehyde ($HCHO$). In case of CO_2, CH_4 or water vapour around 1640 nm, the absorption strength depends on the concentration only in a narrow window linearly. Within this narrow window, often described as linearization point, weighting functions, which describe the change in radiance caused by e.g., varying amount of carbon dioxide in the atmosphere, are used.

The retrieval algorithm used in this study is basically the same as described in Krings et al. (2011).
The approach makes use of an approximation of the logarithm of the measured spectral radiances by a Taylor expansion around the linearization point, which also reflects a first assumption of the atmospheric state at the time of measurement:

[7] Absorption cross-sections describe the absorption behavior of a molecule with respect to wavelength and can also be used to identify species

$$ln\left(I_\lambda^{mea}\right) = ln\left(I_\lambda^{mod}(\bar{\mathbf{c}})\right) + \sum_i W_{\lambda,\bar{c}_i} * \frac{c_i - \bar{c}_i}{\bar{c}_i} + P_\lambda(\mathbf{a}) + \epsilon_\lambda \tag{3.1}$$

Here, I_λ^{mea} denotes the measured spectral radiances at discrete wavelengths λ and the first two terms on the right side represent the linearized radiative transfer model. $I_\lambda^{mod}(\bar{\mathbf{c}})$ is the result of a radiative transfer model (RTM) at the linearization point $\bar{\mathbf{c}}$, where the estimated state of the atmosphere at time of measurement is depicted by the entries $\bar{c}_i$ representing atmospheric parametres like amount of carbon dioxide, methane, water vapour and temperature.
The second term describes the corrections of the linearized model depending on the fit parametres c_i. This is used to scale the column weighting functions $W_{\lambda,\bar{c}_i}$, which represent the derivatives of the radiances with respect to the fit parametre c_i, which has a corresponding estimated $\bar{c}_i$. The weighting functions are calculated by SCIATRAN (Rozanov et al., 2005) using predefined atmospheric profiles for the different parametres e.g., carbon dioxide and methane (fig. 3.5), the HITRAN 2008 spectroscopy data base (Rothman et al., 2009), and a sun spectrum from Livingston and Wallace (1991).

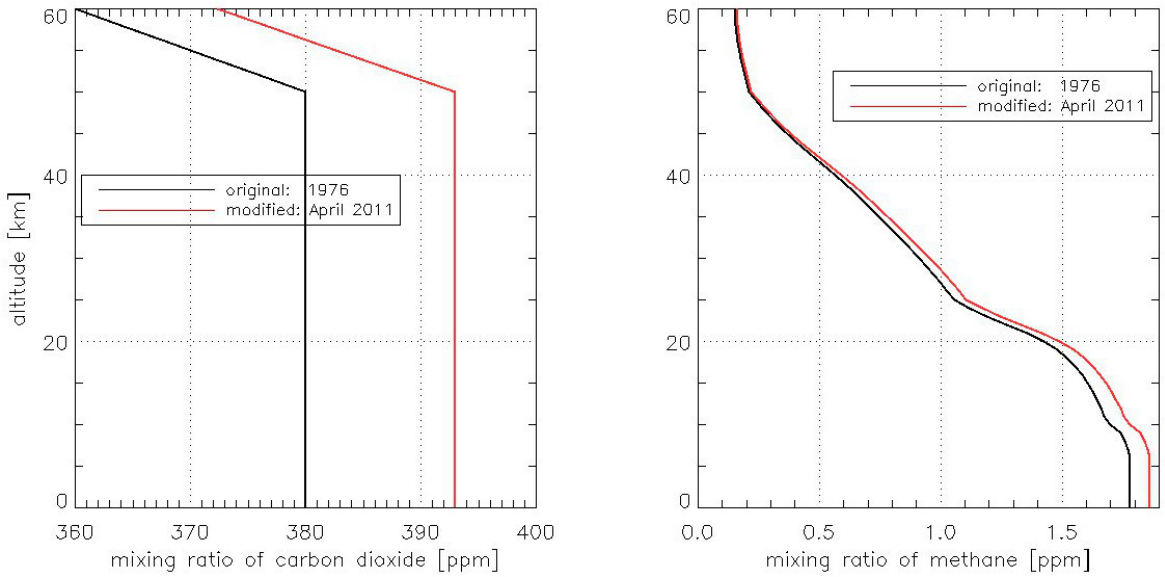

Figure 3.5: Shown are the mixing ratios of carbon dioxide (left panel) and methane (right panel) with respect to altitude as they are defined in the US standard atmosphere in the year 1976 (black line) and scaled to the actual ratios for April 2011 (red line). The scaling values were derived on basis of the discussion in chap. 4.2. These profiles are used for the radiative transfer model and for the retrieval itself.

Moreover, to account for effects varying slowly with wavelength and not well-known, a low-order polynomial $P_\lambda(\mathbf{a})$ with the fit parameters a_i is also added to the linearized model. Normally, the instrument produces detector noise and the low frequency part of the measurement, like surface spectral reflectance, aerosol scattering and the absolute

radiometric calibration function, represented by $P(\mathbf{a})$, cannot be modeled accurately. For that, an error term ϵ_λ is added.
After rearranging eq. 3.1 and using the matrix notation, the problem can be solve by a least squares fit:

$$\begin{pmatrix} ln\left(\frac{I^{mea}_{min}}{I^{mod}_{min}}\right) \\ ln\left(\frac{I^{mea}_{min+1}}{I^{mod}_{min+1}}\right) \\ \vdots \\ ln\left(\frac{I^{mea}_{max}}{I^{mod}_{max}}\right) \end{pmatrix} - \begin{pmatrix} W_{min,\bar{c}_1} & W_{min,\bar{c}_2} & \cdots & \lambda^0_{min} & \lambda^1_{min} & \cdots \\ W_{min+1,\bar{c}_1} & W_{min+1,\bar{c}_2} & \cdots & \lambda^0_{min+1} & \lambda^1_{min+1} & \cdots \\ W_{min+2,\bar{c}_1} & W_{min+2,\bar{c}_2} & \cdots & \lambda^0_{min+2} & \lambda^1_{min+2} & \cdots \\ W_{min+3,\bar{c}_1} & W_{min+3,\bar{c}_2} & \cdots & \lambda^0_{min+3} & \lambda^1_{min+3} & \cdots \\ \vdots & \vdots & & \vdots & \vdots & \\ W_{max,\bar{c}_1} & W_{max,\bar{c}_2} & \cdots & \lambda^0_{max} & \lambda^1_{max} & \cdots \end{pmatrix} * \begin{pmatrix} \frac{c_1-\bar{c}_1}{\bar{c}_1} \\ \frac{c_2-\bar{c}_2}{\bar{c}_2} \\ \vdots \\ a_0 \\ a_1 \\ \vdots \end{pmatrix} = \begin{pmatrix} \epsilon_{min} \\ \epsilon_{min+1} \\ \epsilon_{min+2} \\ \epsilon_{min+3} \\ \vdots \\ \epsilon_{max} \end{pmatrix} \tag{3.2}$$

or in short:

$$\mathbf{y} - \mathbf{A} * \mathbf{x} = \epsilon \tag{3.3}$$

where $\mathbf{y}$ is a vector consisting of the logarithm of the measured intensity divided by the modeled intensity at wavelengths λ_{min} to λ_{max}, $\mathbf{A}$ is a $m * n$ matrix consisting of m spectral points (λ_{max} - λ_{min}) and n fit parametres (c_i+a_i) with the necessary coefficients, $\mathbf{x}$ is a vector containing the unknown n fit parametres, and ϵ is the error because modeled and measured spectra will not fit perfectly.
The approach is to minimize the difference in eq. 3.3 by varying the free fit parametres c_i and a_i simultaneously at all wavelengths:

$$\sum_{\lambda_{min}}^{\lambda_{max}} \epsilon_i^2 = \|\epsilon\|^{\mathbf{2}} = \|\mathbf{y} - \mathbf{A} * \mathbf{x}\|^{\mathbf{2}} \longrightarrow \mathbf{min} \tag{3.4}$$

The solution vector $\hat{\mathbf{x}}$ is then given by

$$\hat{\mathbf{x}} = (\mathbf{A}^T\mathbf{A})^{-1}\mathbf{A}^T\mathbf{y} \tag{3.5}$$

The statistical error of one fit parametre $\sigma_{\hat{x}_i}$ can be deduced from the residual given by $\|\epsilon\|^2$ which represents the differences between adjusted model and measurements:

$$\sigma_{\hat{x}_i} = \sqrt[2]{(\mathbf{A}^T\mathbf{A})^{-1}_{i,i}\frac{\|\epsilon\|^2}{m-n}}) \tag{3.6}$$

with

$$\|\epsilon\|^2 = \sum_{\lambda_{min}}^{\lambda_{max}} \epsilon_i^2 \tag{3.7}$$

where $(\mathbf{A^T A})^{-1}$ is the solution covariance matrix, m is the number of spectral points used for the fit, n is the number of fit parametres and $m - n$ is the number of degrees of freedom of the least squares problem.
Fig. 3.6 shows a typical fit result. The important output parametres used for further analysis are the profile scaling factors of methane and carbon dioxide in the second row. They describe how large the enhancement or decrease in the absorption strength in the measurement compared to the initial estimate at the linearization point is. 1.015 is an increase of 1.5 % and 0.985 is a decrease of 1.5 % in the total column of the specific gas relative to background.

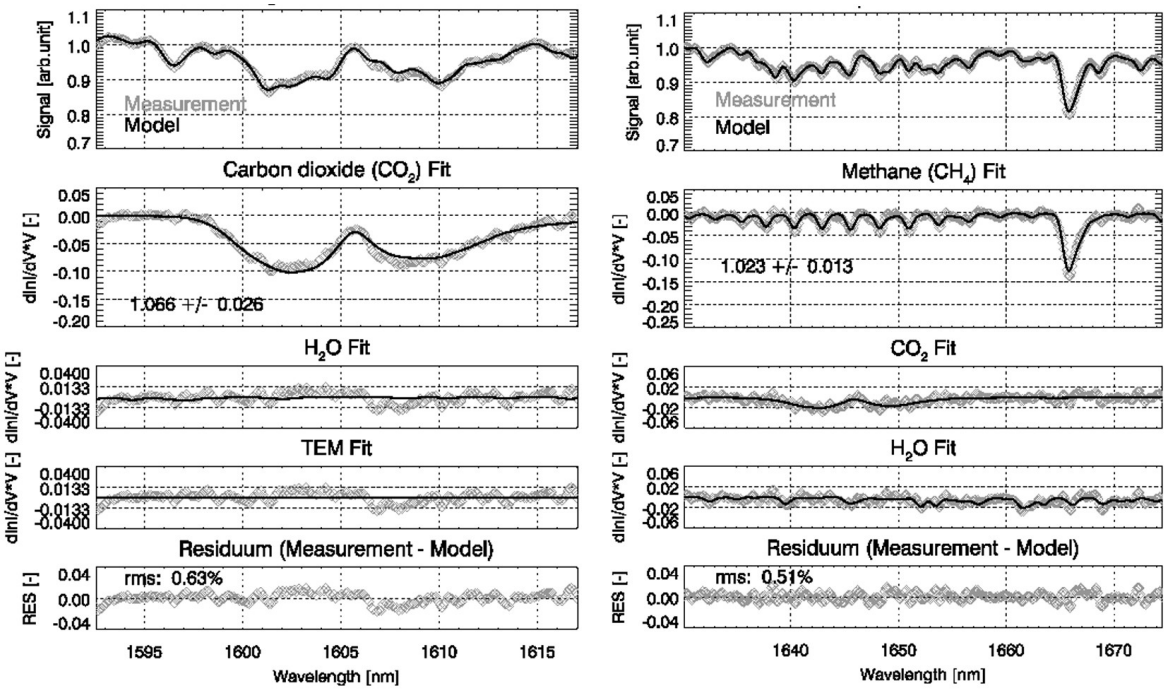

Figure 3.6: The left panels show the fit result for the carbon dioxide retrieval and the right panels show the fit result for the methane retrieval from a readout on the 29 April 2011. The top boxes show the measured spectra in grey rectangles and the fitted model in in black. The differences ϵ_λ between both can be seen in bottom boxes. The middle ones show the result for the fit parametres c_i, namely the profile scaling factor of methane, carbon dioxide, water vapour and a temperature shift.

3.2.2 Column-averaged dry air mole fractions of MAMAP

These altitude-averaged increased or decreased profile scaling factors (PSFs) are then used to calculate column-averaged dry air mole fractions.
In order to estimate the emission fluxes, it is necessary to define a physical property, that only depends on the concentration of the gases under consideration. The retrieved PSFs, however, are influenced by two major effects:

- by varying the concentration of the gas along the light path
- by varying the length of the light path whereas the concentration remains constant

Additionally, that quantity needs to be independent of the water content and temperature in the atmosphere. Mole fractions give the number of a specific species in terms of the total number of molecules e.g., 500 molecules of CO_2 per 1,000,000 molecules of air or 500 parts per million (ppm), in a sample.
The dry air mole fraction considers all molecules except water vapour because the other components of the atmosphere are fairly constant (nitrogen, oxygen) or their influence on the composition can be neglected compared to the most abundant species nitrogen and oxygen. Considering water vapour would not give reliable (wet) mole fractions. Water is temporally and spatially highly variable and can contribute to the atmospheric composition with 5 % (Wallace and Hobbs, 2006) which also depends on temperature.
Therefore, an increase of the dry air mole fraction of CO_2 can be attributed to more CO_2 in the atmosphere and not to less air molecules because water vapour rained out or a change in temperature occurred.
To solve that problem, a second well-mixed gas, which does not significantly vary in the measurement area, can be used because its (wet) mole fraction is influenced in the same way by water vapour as the (wet) mole fraction of the gas of interest. By dividing one by the other, the effect of water vapour vanishes.
An additional advantage, which is even more important, is, that e.g., errors which are introduced by a varying light path and not explicitly accounted for in the modeled spectrum e.g., due to changing surface elevation, flight altitude or multiple scattering because of thin cirrus clouds, would have similar effects on the light path of both gases (gas of interest and well-mixed gas) and light path errors cancel out to large extend in the column-averaged dry air mole fractions.
This implies the usage of O_2 that is measured by MAMAP using the O_2A absorption band because its mole fraction is well-known and spatially and temporally rather constant in the dry atmosphere. Although this method has successfully been applied for example by Schneising et al. (2008) using SCIAMACHY satellite data, it cannot remove all errors. The reason is that the measured absorption band of oxygen is spectrally far away from the absorption band of methane or carbon dioxide and scattered photons are not influenced in the same manner.
The problem can be solved by choosing absorption bands which are spectrally close to-

gether (Frankenberg et al., 2005; Schneising et al., 2009). MAMAP provides the opportunity to measure both carbon dioxide around 1605 nm and methane around 1665 nm simultaneously in its SWIR channel. It can now be assumed that in case of power plants, which only emits carbon dioxide leading to strong gradients near the power plant, the background concentration of methane stays constant and the column-averaged dry air mole fraction of carbon dioxide can be calculated by the normalized column of methane:

$$XCO_2 = \frac{CO_2^{column}}{CH_4^{column}/CH_4^{aver.molefraction}} \tag{3.8}$$

where XCO_2 is the column-averaged dry air mole fraction of carbon dioxide, CO_2^{column} is the measured column of carbon dioxide, CH_4^{column} is the measured column of methane and $CH_4^{aver.molefraction}$ is the averaged background mole fraction for CH_4.
A third possibility is the usage of external data. For that, surface pressure obtained e.g., from meteorological analysis, can be used to calculate the amount and remove the influence of water vapour from the CO_2 column. This requires a relatively high spatial resolution of a few metres to capture all features of the topography. Moreover, errors introduced by a changing profile scaling factor not caused by a changing concentration of trace gas but due to a change in the light path, are not corrected.

Furthermore, the column averaging kernels $AK(z)$ of MAMAP have to be considered (Krings et al., 2011). They describe the change of the retrieved parametres $c_{retrieved}$ if the true parametres c_{true} vary at a certain altitude z:

$$AK(z) = \frac{\partial c_{retrieved}}{\partial c_{true}(z)} \tag{3.9}$$

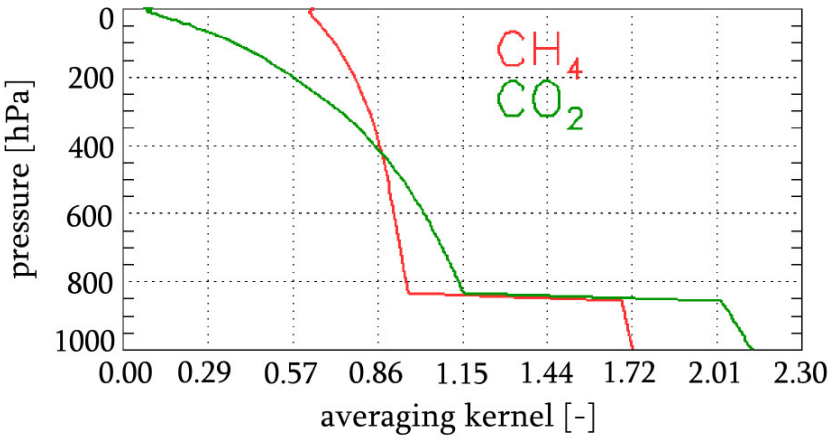

Figure 3.7: Averaging kernels of methane and carbon dioxide of the modeled spectrum used for the overflight of power plant Jänschwalde in 2011. The step at around 850 hPa corresponds to the flight altitude of 1540 m.

They are also a measure of altitude sensitivity. An averaging kernel smaller than 1 indicates an underestimation of the parametres, vice versa, an averaging kernel larger than 1 e.g., 2, leads to an overestimation of the true value by a factor of 2.
This effect needs also to be taken into account for the retrieved columns of carbon dioxide and methane in case of MAMAP. As fig. 3.7 indicates, all retrieved columns are overestimated. This can be explained by the viewing geometry of the aircraft and the location of the plume provided all changes in CO_2 and CH_4 occur below the aircraft. The light has to pass the atmospheric column below the aircraft twice before it is registered by the instrument. Therefore, the absorption and sensitivity, respectively, is twice as high as above the aircraft. Assuming that the whole plume is located below the aircraft, the column can be corrected by the inverse of the weighted[8] averaged column averaging kernel k below the instrument:

$$k = \frac{1}{\overline{AK}_{below}} \tag{3.10}$$

The correction factor k (0.485 in case of the Jänschwalde overflight in 2011 for CO_2) is applied to the statistical error (eq. 3.6) and to the column-averaged dry air mole fractions (eq. 3.8):

$$\sigma^{corrected} = k * \sigma \tag{3.11}$$

$$XCO_2^{corrected} = CO_2^{aver.molefraction} + k * \left(XCO_2 - CO_2^{aver.molefraction}\right) \tag{3.12}$$

[8]taken into account the decreasing density of the atmosphere with altitude

3.3 The Gaussian plume model

The column-averaged dry air mole fractions (see previous section) describe an increase or decrease of, here, CO_2 with respect to the assumed background concentration in the modeled spectrum/atmosphere. Depending on the flight pattern of the airplane, the emission rate of a target and the wind speed, a clear plume can be seen in the measurements visually (also compare to fig. 4.2a, 4.2c, 4.5 and 4.6). The aim of this section is to introduce the plume model, which is used to model the measurements and obtain the emission rate.
For that, the first part describes general assumptions of the model and gives an overview of how it works and looks like. Next, the model is modified so that it can depict and simulate the MAMAP measurements, which yields the emission rate. Therefore, in the last section, an important parametre, the mean wind speed of the plume, is derived on basis of a further version of the model describing the vertical extent and distribution of the plume in the atmosphere.

3.3.1 The general 3D Gaussian plume model

The model used in this work to derive the emission rates is described in detail in Krings et al. (2011, 2013). It is based on the Gaussian plume model (Sutton; Gifford, 1961; Pasquill) which simulates a plume of e.g., a power plant. Fig. 3.8 depicts such a plume schematically.

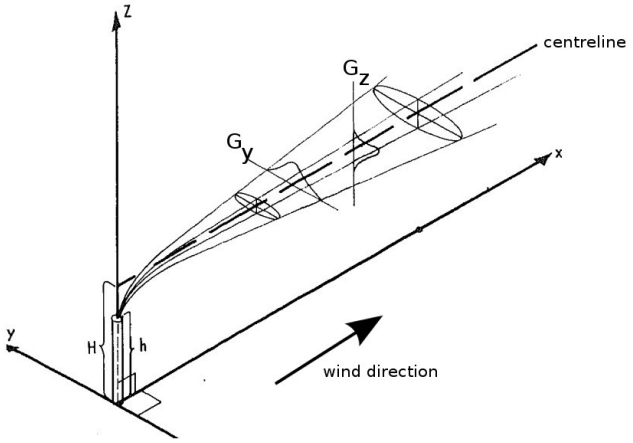

Figure 3.8: Shown is a 3D Gaussian plume which is emitted by a point source at a certain height h and rises to the height H at the origin before it follows the wind direction along the x-axis. It is diverging symmetrically around the centreline at the height H while it is moving away from the source. The diverging process is defined by two Gaussian function $G_y(x)$ (in the horizontal axis) and $G_z(x)$ (in the vertical axis), whereby their standard deviations give the 1-σ environment of the plume (68.27 % of the plume is located within this environment and the two ellipses, respectively) (modified after Turner (1970, p. 5)).

The figure shows an idealized, time-averaged plume, which is released at the origin at a certain height h from a stack to the atmosphere. Due to an initial velocity of the exhaust gases in z-direction and buoyancy effects, it might rise further (to a height H) before it follows the wind direction, here, in positive x-direction. Time-averaged means that many snapshots of a real plume in the atmosphere are taken and superimposed. One picture might show an irregular and disturbed shape but in the mean, the plume symmetrically arranges itself around a centerline pointing in wind direction. Near the source, the plume is quite narrow but as it is moving away, it is diverging along the z-axis (vertically) and along the y-axis (horizontally).
Mathematically, these diverging or dispersion processes can be described by two Gaussian curves indicated by the two cross sections $G_y(x)$ and $G_z(x)$ in fig. 3.8. The Gaussian dispersion model now relates the emission rate F [g/s] of the power plant, the mean wind speed u [m/s] of the plume and the horizontal and vertical dispersion coefficients σ_y [m] and σ_z [m] to the concentration C [g/m^3] at each point (x, y, z):

$$C(x,y,z) = \frac{F}{\sqrt{2\pi} * \sigma_y(x) * \sigma_z(x) * u} * \exp\left(-\frac{1}{2} * \left(\frac{y}{\sigma_y(x)}\right)^2\right) * \exp\left(-\frac{1}{2} * \left(\frac{z-H}{\sigma_z(x)}\right)^2\right) \tag{3.13}$$

The dispersion coefficients are a measure of and related to the stability of the real atmosphere. They describe the 1-σ deviation of the plume extend from the centreline at a certain distance x and can be looked up in Turner (1970); Pasquill and Martin (1976). These parametres are based on empirical findings and divide the stability of the atmosphere in different classes, from very unstable (A) to stable (F) (tab. 3.2) depending on the surface wind velocity and the solar insolation. Each class consists of a set of values, one for the horizontal dispersion (a) and three four the vertical dispersion (c, d, f), also depending on the distance from the source (tab. 3.3), which are then used for calculating σ_y [m] and σ_z [m]:

$$\sigma_y = a * (x + x_0)^{0.894} \tag{3.14}$$

and

$$\sigma_z = c * (x + x_0)^d + f \tag{3.15}$$

where x is the distance from the source in km and x_0 the offset distance in km. To contribute for a certain areal extent of a point source e.g., the stack width y_0 [m] of a power plant, the offset distance x_0 is applied, which describes a 2-σ environment, where 95.45 % of the exhaust gases are found:

$$x_0 = \left(\frac{y_0}{4 * a}\right)^{\frac{1}{0.894}} \tag{3.16}$$

surface wind speed $\left[{}^{m}/_{s}\right]$	day solar insolation		
	strong	**moderate**	**slight**
< 2	A	A-B	B
2-3	A-B	B	C
3-5	B	B-C	C
5-6	C	C-D	D
> 6	C	D	D

Table 3.2: Atmospheric stability classification on basis of surface wind speed and day solar insolation: A ≡ very unstable, B ≡ moderately unstable, C ≡ slightly unstable, D ≡ neutral. During night, additional stability classes are possible: E ≡ slightly stable, F ≡ stable (Pasquill).

		$x \leq 1\,\mathbf{km}$			$x > \mathbf{1km}$		
stability	**a**	**c**	**d**	**f**	**c**	**d**	**f**
A	213	440.8	1.941	9.27	459.7	2.094	−9.6
B	156	106.6	1.149	3.3	108.2	1.098	2.0
C	104	61.0	0.911	0.0	61.0	0.911	0.0
D	68	33.2	0.725	−1.7	44.5	0.516	−13.0
E	50.5	22.8	0.678	−1.3	55.4	0.305	−34.0
F	34	14.35	0.740	−0.35	62.6	0.180	−48.6

Table 3.3: Values for the stability parametres given for different stability classes and distances x from the source (Martin, 1976).

It should be emphasized that the classification of the stability as shown in tab. 3.2, is just used as an indicator and later replaced by a more sophisticated method, which is based on the measured data (see chap. 3.3.2).

In order to apply the model correctly, some further assumptions have to be taken into account:

- the emission rate has to be constant during time of measurement/overflight
- the wind speed has to be constant during the overflight and over space
- the gas of interest within the plume has to be conservative
- the terrain downwind of the source has to be relatively flat

Especially, the quantity wind speed needs further discussion because it is highly variable with altitude and not spatially and temporal constant (see chap. 3.3.3).

3.3.2 Integrated column and horizontal extent of a plume (2D)

In the previous section the Gaussian plume model was introduced which allows calculations of the concentration of a pollutant, for example, emitted by a power plant at any point. The following part is dedicated to the application of eq. 3.13 to the MAMAP measurements in order to derive the emission rate. For that it needs to be discussed which quantity MAMAP measures in terms of the plume model and which method can then be used to derive the emission rate from the measurements.
From chap. 3.2, it is known, that the intermediate quantity column-averaged dry air mole fraction of CO_2 (XCO_2) derived from the measured spectra, is the corrected amount of carbon dioxide relative to the background below the aircraft. Furthermore, it represents the whole and integrated column, respectively, and does not contain any altitude distribution information about the gas location. Therefore, eq. 3.13 can also be integrated along the z-axis, from the ground to the top of the atmosphere, to obtain an integrated column V [g/m^2] (Krings et al., 2011):

$$V(x,y) = \int_0^\infty C(x,y,z)dz = \frac{F}{\sqrt{2\pi} * \sigma_y(x) * u} * \exp\left(-\frac{1}{2} * \left(\frac{y}{\sigma_y(x)}\right)^2\right) \tag{3.17}$$

Providing the emission rate of the power plant, the mean wind speed of the plume and the stability of the atmosphere is known, the plume can be modeled in the xy-plane (fig. 3.9):

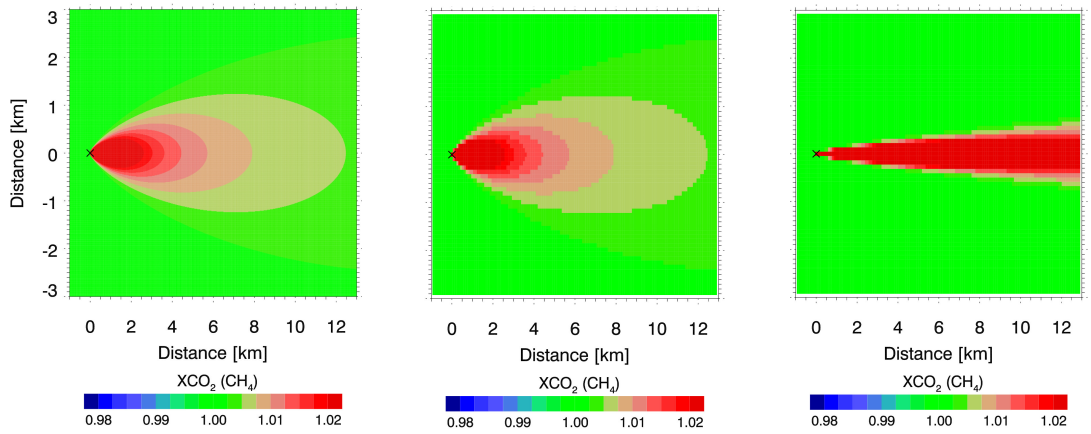

(a) Simulation of a highly resolved scene. Atmospheric stability has been assumed to be very unstable (class = A, a = 213.0).

(b) Simulation at approx. MAMAP ground scene size (90 m * 90 m). Atmospheric stability has been assumed to be very unstable (class = A, a = 213.0).

(c) Simulation at approx. MAMAP ground scene size (90 m * 90 m). Atmospheric stability has been assumed to be stable (class = F, a = 34.0).

Figure 3.9: Shown are column-averaged dry air mole fractions of CO_2 relative to the background. The point source is located at $(0, 0)$ marked by a black cross. All simulations use a mean wind speed u of 5 m/s, an emission rate of F of 765000 g/s and a source width y_0 of 50 m.

For the estimation of the emission rate from the MAMAP measurements, eq. 3.17 is used in an optimal estimation approach, where the $V(x, y)$ correspond to the measured columns based on the column-averaged dry air mole fractions. Under the assumption, the mean wind speed u is known, the two fit parametres emission rate F and the stability parametre a hidden in the horizontal dispersion coefficient σ_y (compare to eq. 3.14) are adjusted until agreement between model and measurements is at maximum (for further information see Krings et al. (2011) and Krings (2012)). The advantage of fitting both emission rate and stability simultaneously is that the empirical approach based on wind speed and solar insolation is subjective to a certain degree. Additionally, the stability classification in tab. 3.2 only delivers reasonable emission rates in case of a perfect plume. Often, the plume measured by the MAMAP instrument has experienced an artificial broadening due to changing wind directions or wind shear with altitude or additional turbulences have been introduced due to the hot exhaust gases, which have to be taken into account.
For retrieving the emission rate of a specific power plant from the MAMAP measurements, the parametre mean wind speed u enters linearly eq. 3.17. That means, if the mean wind speed is wrong by 5 %, then also the emission rate estimate is wrong by 5 %. Therefore, a sensible way of deriving the mean wind speed needs to be found.

3.3.3 Vertical extent and distribution of a plume (2D)

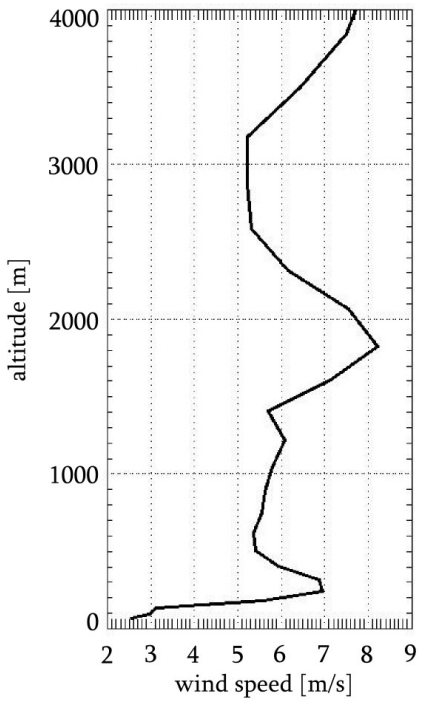

Figure 3.10: Vertical wind speed profile based on COSMO-DE model of German Weather Service.

The mean wind speed in eq. 3.17 is an important parametre and its error propagates linearly to the final emission rate estimates. Thus, it needs to be estimated properly. The following section discusses what needs to be considered and presents a method to retrieve a mean wind speed of the plume at the end.
Fig. 3.10 shows an arbitrary vertical wind profile based on the COSMO-DE model by the German Weather Service. It can be seen that the wind speed has a high variability with altitude. Using this wind profile to derive a mean wind speed of a plume of a power plant means, that its location must be known. If the plume was located in the lower 100 m, it would have a mean wind speed of approx. $3\,{}^{m}/_{s}$. But it could also be located around 1000 m leading to a mean wind speed of about $6\,{}^{m}/_{s}$. The resulting emission rates based on these wind speeds would also differ by a factor of 2.
That means, first, the plume location is estimated, and based on this, the mean wind speed is derived.

The vertical plume model

For the first part, a modified version of eq. 3.13 is used:

$$C(x,0,z) = \frac{F}{\sqrt{2\pi} * \sigma_z(x) * u} * \left\{ \exp\left(-\frac{1}{2} * \left(\frac{z - H - s_{elevation}}{\sigma_z(x)} \right)^2 \right) + \exp\left(-\frac{1}{2} * \left(\frac{z + H - s_{elevation}}{\sigma_z(x)} \right)^2 \right) + \text{correction terms} \right\} \tag{3.18}$$

where H is the height of the centreline in m and $s_{elevation}$ is the surface elevation in m. Eq. 3.18 describes the vertical distribution of the plume along the centreline ($y = 0$) downwind of the point source (in positive x-direction). The first exponential function considers the total source height (stack height h, which is assumed to be equal to height H of the centreline, and surface elevation $s_{elevation}$) and the second one the reflection of the plume at the ground. If the plume hits the ground, it is not lost but reflected upward and rises. The term *correction terms* is responsible for further reflections (compare to eq. 3.19) which are discussed later.
Fig. 3.11 illustrates the application of eq. 3.18 for the two different atmospheric stability classes A and B. It shows an emission source at a height of around 180 m and the wind blows in x-direction. Near the source, the amount of exhaust gases are relatively high whereby they are lower further away and higher up. Depicted are normalized concentrations so that the total amount of gas at each x in the column (from the ground to top of the atmosphere) is 1. In other words, the total amount of gas at a certain distances x remains constant in the total column, it just becomes blurred in the vertical. Moreover, due to the normalization, they only depend on the vertical dispersion coefficient σ_z, which considers the stability of the atmosphere, and not on the emission rate F and mean wind speed u (compare to eq. 3.15 and tab. 3.3).
This basic model suggests, that the plume is able to reach altitudes as high as 6000 m and even more under very unstable atmospheric conditions (fig. 3.11a). Compared to that, a plume located in a moderately stable atmosphere (3.11b) diverges much less and only reaches a height of 2000 m at a distance of 4100 m. As already discussed in chap. 2.2.2, usually, there is a capping layer in the atmosphere which separates the free troposphere from the planetary boundary layer. Pollutants emitted near the ground are not able to penetrate this layer easily in case it is a strong inversion. Assuming the exhaust gases are trapped within the lower part of the troposphere, eq. 3.18 can be expanded by additional correction terms (eq. 3.19), which describe the reflection of the plume at a certain altitude (modified after Bierly and Hewson (1962)).

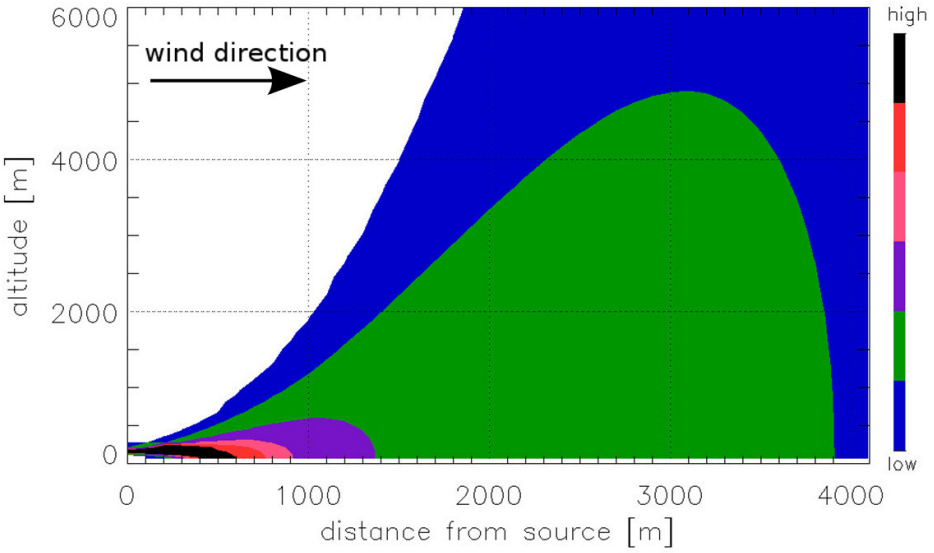

(a) The atmospheric stability has been assumed to be very unstable (class = A; $a = 213.0$; for $x \leq 1000\,\mathrm{m}$: $c = 440.8$, $d = 1.941$, $f = 9.27$; for $x > 1000m$: $c = 459.7$, $d = 2.094$, $f = -9.6$).

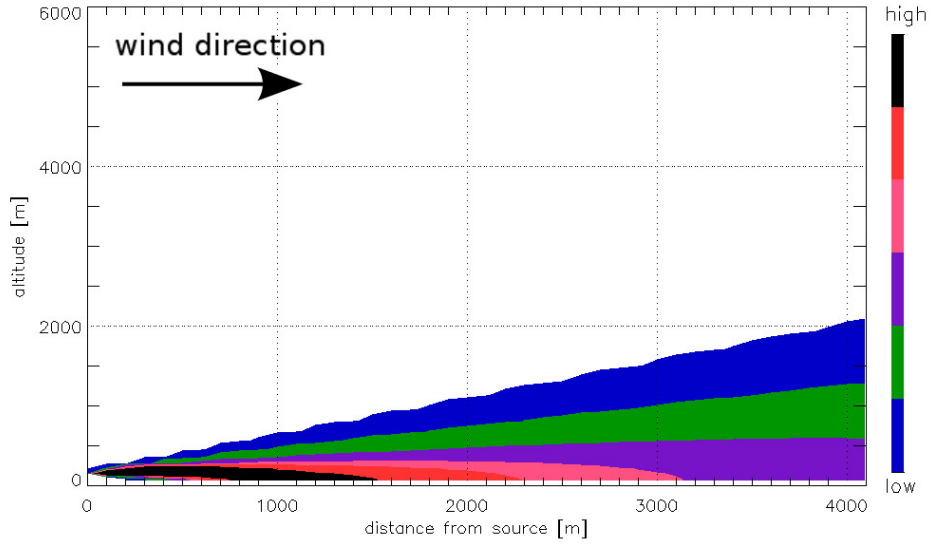

(b) The atmospheric stability has been assumed to be moderately unstable (class = B; $a = 156.0$; for $x \leq 1000\,\mathrm{m}$: $c = 106.8$, $d = 1.149$, $f = 3.3$; for $x > 1000m$: $c = 108.2$, $d = 1.098$, $f = 2.0$).

Figure 3.11: Shown are model runs with eq. 3.18 without the correction term. The emission of exhaust gases take place at the origin at an altitude of 180 m $\big($stack hight $h(= H) = 120\,\mathrm{m}$, surface elevation $(s_{elevation}) = 60\,\mathrm{m}\big)$ and a source width $y_0 = 50\,\mathrm{m}$). The distance from the source is on the x-axis in m and the y-axis depicts the altitude in m. Displayed are cross sections of the plume parallel to the centreline or x-axis at $y = 0$ (also compare to fig 3.8) and the colour code represents normalized concentrations with the total column (black $\hat{=}$ high amount of gas and blue $\hat{=}$ low amount of gas), which are independent of the emission rate F and the mean wind speed u.

$$\text{correction terms} = \sum_{m=1}^{T}\left[\exp\left(-\frac{1}{2}*\left(\frac{z+H-s_{elevation}+2*m*(-r_{height}+s_{elevation})}{\sigma_z(x)}\right)^2\right)\right.$$
$$+\exp\left(-\frac{1}{2}*\left(\frac{z-H-s_{elevation}+2*m*(+r_{height}-s_{elevation})}{\sigma_z(x)}\right)^2\right) \quad (3.19)$$
$$+\exp\left(-\frac{1}{2}*\left(\frac{z+H-s_{elevation}+2*m*(+r_{height}-s_{elevation})}{\sigma_z(x)}\right)^2\right)$$
$$\left.+\exp\left(-\frac{1}{2}*\left(\frac{z-H-s_{elevation}+2*m*(-r_{height}+s_{elevation})}{\sigma_z(x)}\right)^2\right)\right]$$

where r_{height} [m] is the height of the reflection layer where the plume is reflected downwards. Each of the four exponential functions describe a specific kind of reflection, whereas the summation gives the number of reflections. For example, if the reflection layer is rather low e.g., around 500 m, the atmosphere is very unstable, and the plume shall be simulated till a distance x of 4000 m, then, at least 30 terms are necessary ($T = 30$). Otherwise, the integrated column is lower than 100 % at a certain distance x and part of the gas has been lost due to missing multiple reflections. Fig. 3.12b depicts the relation between the number of terms T and the loss of exhaust gases, again, for a very unstable atmosphere, but the reflection layer ist around 1000 m. It can be said, that the reflection terms are less important, if the atmosphere is more stable and the reflection layer is higher up in the atmosphere.
Fig. 3.12a shows a typical plume distribution with a reflection layer at approx. 1000 m. The remaining parametres are the same as in fig. 3.11a. It can be seen that due to the trapping effect at 1000 m, the normalized concentrations have increased, especially after 1000 m.
Combining this vertical plume distribution with vertical profiles of wind speed (fig. 3.10), the mean wind speed of the plume can be estimated.

New vertically highly resolved wind and temperature profiles

In order to get an idea where possible trapping or reflection layers can be found and what are the wind speeds and directions, modeled data from the routine analysis of the numerical weather prediction model COSMO-DE from the German Weather Service (DWD) (Doms and Schättler, 2002) has been applied. The data is available hourly at a horizontal resolution of $0.025° * 0.025°$ which corresponds to approx. $2.8\,\text{km} * 2.8\,\text{km}$. Compared to the old study by Krings et al. (2011), where one whole vertical profile only consisted of 10 values, the new highly resolved profiles consists of 50 values (fig. 3.13).

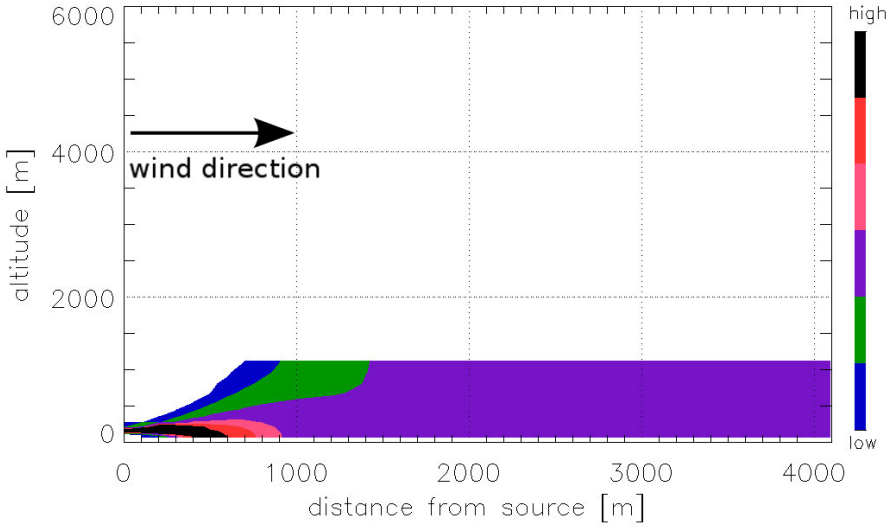

(a) Shown is a cross section parallel to the centreline similar to 3.11a but with a reflection layer at 1000 m and $T = 30$.

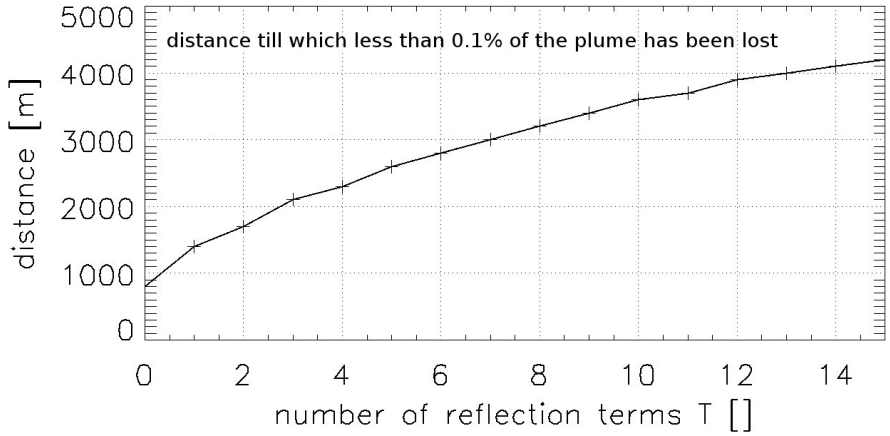

(b) The plot depicts the number of reflection terms T on the x-axis and the distance from the source on the y-axis. The black curve shows at which distance more than 0.1 % is lost due to missing reflections depending on the number of reflection terms T. For example, without any reflection term ($T = 0$), already after 1000 m, more than 0.1 % of the plume is lost, whereas with $T = 15$, losing plume starts after 4100 m firstly.

Figure 3.12: Shown are simulations of the Gaussian plume model with the correction terms attributing a reflection layer at approx. 1000 m (eq. 3.18 in combination with eq. 3.19). The remaining parametres are the same as for the simulation in fig. 3.11a. The stability of the atmosphere has been assumed to be very unstable (class = A) and emission has taken place at an altitude of 180 m.

Moreover, additional to wind speed and direction, also the potential temperature is given serving as a measure of the stability of the atmosphere (compare to chap. 2.2).
The advantages in the new profiles are that they are more detailed than the old ones and provide even some information about a possible layering of the atmosphere. For example, the strong increase in potential temperature aloft 1500 m in fig. 3.13a indicates a very stable layer. A change in potential temperature with altitude is often accompanied by a jump in the wind speed (fig. 3.13b) and wind direction (fig. 3.13c). Especially in terms of wind speed jumps, it is important to give a reasonable estimate of how the stability of certain layers, based on potential temperature, might influence the plume propagation and location. These kind of information was not available in the past because it is almost impossible to infer proper information about an atmospheric layering from 4 values in the lower 4000 m compared to 23 and without any potential temperature.

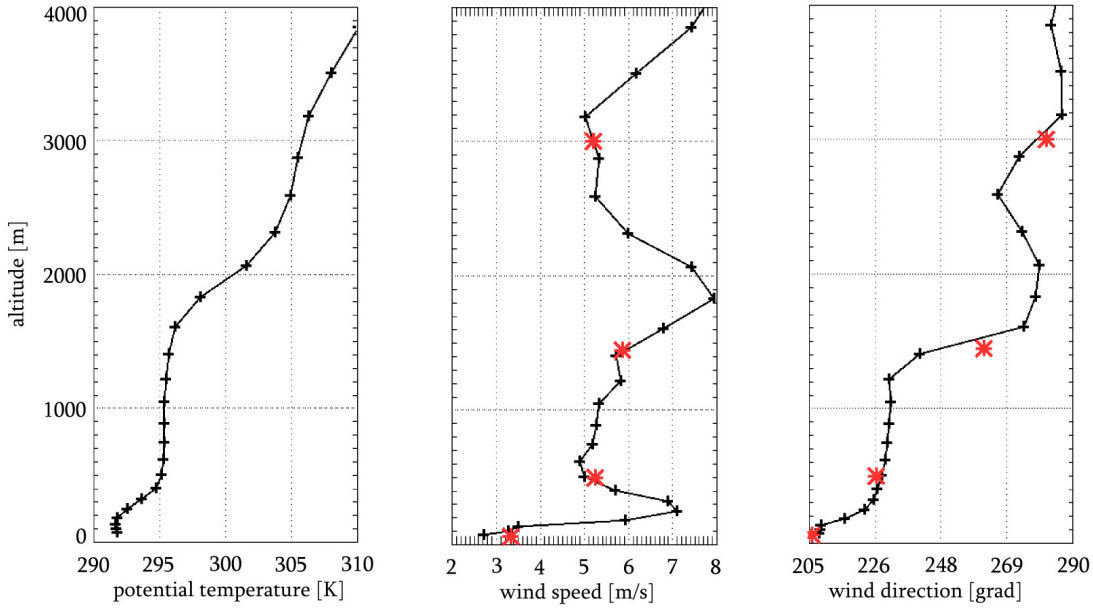

(a) Highly resolved profile of potential temperature.

(b) Profiles of wind speed. Black: highly resolved. Red: coarsely resolved.

(c) Profiles of wind direction. Black: highly resolved. Red: coarsely resolved.

Figure 3.13: Shown are vertically highly resolved profiles based on the COSMO-DE model from the DWD in black for the lower 4000 m, which have been used in this study. The black crosses correspond to the available value at an atmospheric layer at a given altitude. The red crosses depict the coarsely resolved profiles also based on COSMO-DE model data from the DWD, which were used in Krings et al. (2011).

This extra knowledge is used in combination with the vertical plume model (eq. 3.18 and 3.19). From the vertical profiles of the potential temperature, potential reflection layers are extracted, which are then applied to the model to simulate the plume distribution parallel to the centreline at certain distances x from the source (fig. 3.12a). The stability class of the atmosphere has been estimated by fitting stability parametre a and emission

rate F in the horizontal plume model by the optimal estimation method (compare to chap. 3.3.2) to the measurements assuming a reasonable mean wind speed, beforehand. In the next step, the concentration of exhaust gases in the different atmospheric layers, which are given by the COSMO-DE model e.g., the amount of gas in % between 60 m and 120 m, 120 m and 200 m, 200 m and 250 m, etc., can be calculated at each distance x. These concentrations are weights for the wind speed profiles at x. The wind speed is given in the middle of these layers where the concentrations have been calculated for e.g. given at 90 m for the first layer (60 - 120 m), 165 m for the second layer (120 - 200 m), etc.
Assuming a two layered atmosphere, where the first layer contains 40 % of the plume and a wind speed of 3 $^m/_s$, and the second layer 60 % and a wind speed of 6 $^m/_s$, results in a mean wind speed of the whole plume of 4.8 $^m/_s$ (both layers have the same wind direction). But if the wind blew in exactly opposed directions with the same speed of 3 $^m/_s$, using the absolute wind speeds, would result in a wrong mean wind speed of 3 $^m/_s$ instead of the correct one of 0 $^m/_s$. Therefore, not the absolute values but the single components u (x - direction) and v (y - direction) are used, also given by the DWD model. This intermediate step is necessary in order to consider different wind directions in the different layers.
This calculation is done at each distance x downwind of the source along the centreline, whereby also the wind profiles can differ from x to x depending on the model data. To make available vertical profiles on a finer grid than provided by the DWD (2.8 km $*$ 2.8 km), the modeled data is interpolated to 0.100 km $*$ 0.100 km. The model does not only provide the absolute wind speeds but also the values for the u (x - direction) and v (y - direction) components separately. Finally, at each distance x and each hour, a mean wind speed of the plume has been calculated, which can be averaged over the whole plume or just over certain distances e.g., from 500 m to 1500 m and 2500 m to 4500 m, depending on the shape of the flight track and time of overflight (compare to chap. 5). Finally, the resulting mean wind speeds are again used in the horizontal plume model (optimal estimation, chap. 3.3.2) to derive the conclusive emission rate of the source.

Chapter 4

Atmospheric mole fraction results

This chapter deals with the extraction of the input parametres needed for determining the linearization point in the radiative transfer model, and the application of the retrieval algorithm introduced in chap. 3.2.
Therefore, the algorithm has been utilized to the previously analyzed data set of 2007 already published by Krings et al. (2011).
After that, the same procedure has also been used for the new measurements from the year 2011, which have not been published yet, of the same power plants Jänschwalde and Schwarze Pumpe.
In the third part, the obtained columns and column-averaged dry air mole fractions, respectively, from both years are compared with each other, especially in terms of fit quality and precision.

4.1 The measurement flight of 2007

This part is dedicated to the measurements from the year 2007. It should be tested whether it is possible to reproduce the column-averaged dry air mole fractions of carbon dioxide of CO_2 with the CH_4-proxy method $\left(XCO_2(CH_4)\right)$ in case of the power plants Jänschwalde (JW) and Schwarze Pumpe (SP) and whether the retrieval worked on the new system correctly. Additionally, recent optimizations in the retrieval algorithm could also have an impact on the results.

4.1.1 Target description and flight parametres of 2007

The campaign, which was a test flight, took place near Berlin in Germany in July 2007 and the MAMAP instrument was mounted on a Cessna 207 aircraft from the FU Berlin. The flight took place on 26 July in the morning, whereby the overflight time of the power plant Jänschwalde was between 08:55 and 09:20 UTC and Schwarze Pumpe was between 08:10 and 08:55 UTC (Krings et al., 2011). Both power plants, located south

east of Berlin in the Lausitz and operated by Vattenfall Europe Generation AG, Cottbus, Germany, are coal-fired.

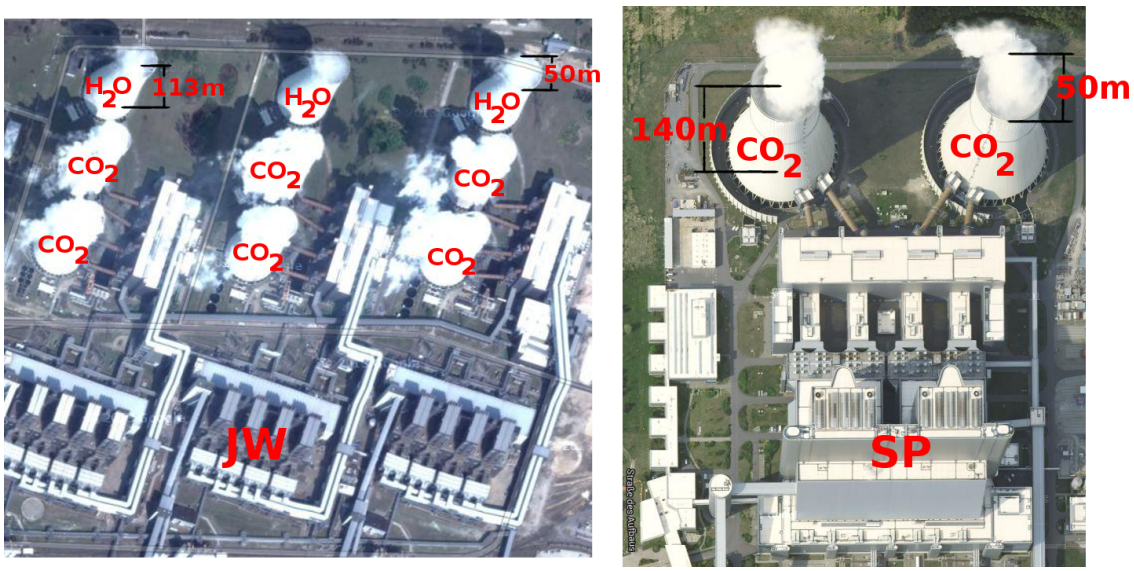

Figure 4.1: Shown are the two targets power plant Jänschwalde (JW, left panel) and Schwarze Pumpe (SP, right panel). Jänschwalde consists of 9 cooling towers with a height of 113 m and a diameter of 50 m whereas only 6 (marked by 'CO_2') are used to emit flue gases (CO_2 and H_2O). The pure water vapour emitting stacks are labeled by 'H_2O'. Schwarze Pumpe has only two cooling towers with a height of 140 m and a diameter of 50 m but both emit the exhaust gases and water vapour (labeled by 'CO_2'). (produced with Google Maps - © 2013 Google)

Jänschwalde (fig. 4.1, left panel) has a total power output of 3000 MW which is divided in 6 units with 500 MW. It burns lignite, which exhaust gases and water vapour trapped within the coal are released by 9 cooling towers with a stack hight of 113 m whereas 6 emit CO_2 and H_2O and 3 only water vapour. The annual CO_2 emission was 23.6 $^{MtCO_2}/_{yr}$ in 2009 (data from the Carbon Monitoring for Action (CARMA) Database, www.carma.org, last visit: 08.08.2013).
For Schwarze Pumpe (fig. 4.1, right panel), the total power output of 1600 MW is produced by also firing lignite in 2 units. The flue gases and water vapour are released by two cooling towers at an altitude of 140 m. Its annual CO_2 emission was 10.7 $^{MtCO_2}/_{yr}$ in 2009 (data from the Carbon Monitoring for Action (CARMA) Database, www.carma.org, last visit: 08.08.2013).
The actual emission rates at time of the overflights were provided by the power plant provider on a temporal resolution of 15 min, which were converted to the yearly values. On the day of the overflight, clear sky without clouds was prevailing and the wind was blowing from approx. south-west. The flight conditions are further discussed in chap. 5.1 and 5.2 whereas tab. 4.1, first row gives an overview of additional parametres also necessary for the modeled spectrum.

Target	aircraft altitude	surface elevation	SZA	albedo	aerosol scenario	background XCO_2	background XCH_4
2007, both	1.25 km	0.00 km	40.0°	0.18	urban	380 ppm	1700 ppb
2011, JW	1.54 km	0.06 km	41.0°	0.18	urban	393 ppm	1779 ppb
2011, SP	1.56 km	0.11 km	38.5°	0.18	urban	393 ppm	1779 ppb

Table 4.1: The table depicts the main parametres of the modeled spectra, which were used to simulate the spectrum at the linearization point for the years 2007 and 2011, respectively. The values of the first row were adopted from Krings et al. (2011) and, for completeness, the values of the second and third row are also given but discussed in chap. 4.2. For 2007, only one radiative transfer model run was used as in Krings et al. (2011), whereas for 2011, two RTM runs were applied to account for different conditions at the two power plants.

4.1.2 XCO_2 of 2007 and comparison to already published data

Fig. 4.2 shows the reproduced columnar change of the dry air mole fractions of CO_2 of the power plants Jänschwalde (fig. 4.2a) and Schwarze Pumpe (fig. 4.2c) for the year 2007. They (fig. 4.2a and 4.2c) clearly depict enhanced CO_2 relative to the background downwind of the power plants $\big(XCO_2(CH_4) > 1.00\big)$, whereby the remaining parts are almost at background concentration $\big(XCO_2(CH_4) \approx 1.00\big)$. It is important to point out, that the plots depict an enhanced or decreased CO_2 concentration only compared to the normalized background concentration assumed for the modeled spectrum at the linearization point (eq. 3.12).
The panels in fig. 4.2b and 4.2d compare the measurements of the re-retrieved XCO_2 and the published values in Krings et al. (2011) for Jänschwalde (JW) and Schwarze Pumpe (SP), respectively. Important quantities are the XCO_2 itself and the position of a measurement. In case of the location, the distance in x-direction of each measurement in the area to the source $\big($JW (fig. 4.2b) or SP (fig. 4.2d)$\big)$ was used. In the left scatter plots, the new distance is written on the x-axis and the old one on the y-axis. The y-interception of the fitted lines $y_{JW,x}$ and $y_{SP,x}$ is not equal $0\,m$, which means that the location of the re-retrieved measurements differs from the old one. The same can be observed for the distance in y-direction. For XCO_2 (right panel), the same has been done, but an y-interception of 0 and a slope of 1 proof that the values are still identical. The shift in the location of one measurement occurs in flight direction and can be explained by a new function added to the retrieval algorithm. One measurement consists of ten readouts which are routinely assigned to the same GPS location, namely, the longitude and latitude of the first readout. This assumption can be further refined by considering the movement of the aircraft while the single readouts are taken. A geolocation correction interpolates the longitude and latitude between the first readout of a measurement and the first readout of the next measurement and, then, calculates an averaged longitude and latitude from the readouts for one co-added measurement/burst. This leads to a shift in flight direction.

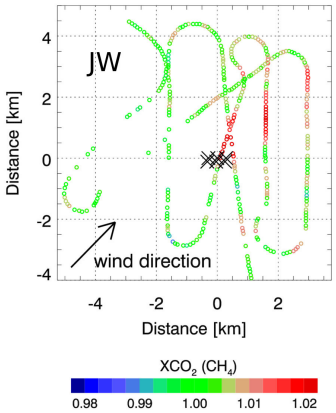

(a) Retrieved column-averaged dry air mole fractions $XCO_2(CH_4)$ normalized to the background. Reproduced columns from the flight over Jänschwalde (JW) in 2007.

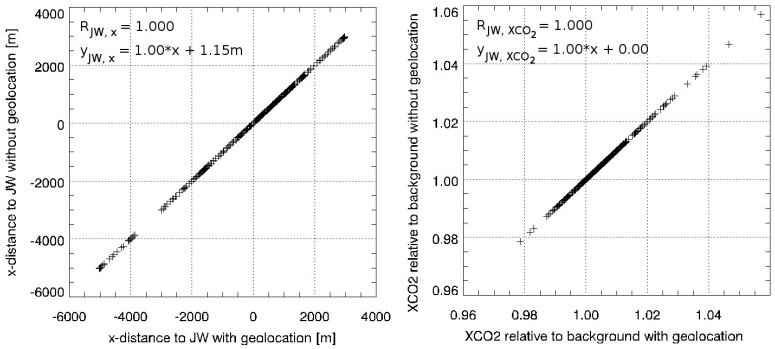

(b) Left panel: the scatter plot depicts the relation between the original x-distance (as in Krings et al. (2011)) and the re-retrieved x-distance, which is influenced by the geolocation correction, from the power plant Jänschwalde. Right panel: relation between the original column-averaged dry air mole fractions of CO_2 (as in Krings et al. (2011)) and the re-retrieved column-averaged dry air mole fractions of CO_2 of the overflight of power plant Jänschwalde.

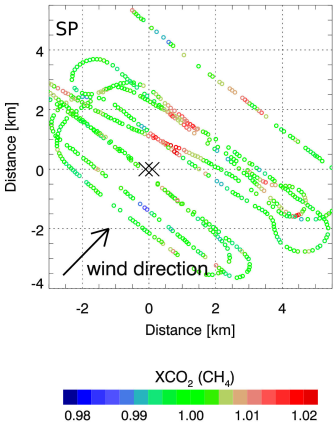

(c) As in (a) but for Schwarze Pumpe (SP) 2007.

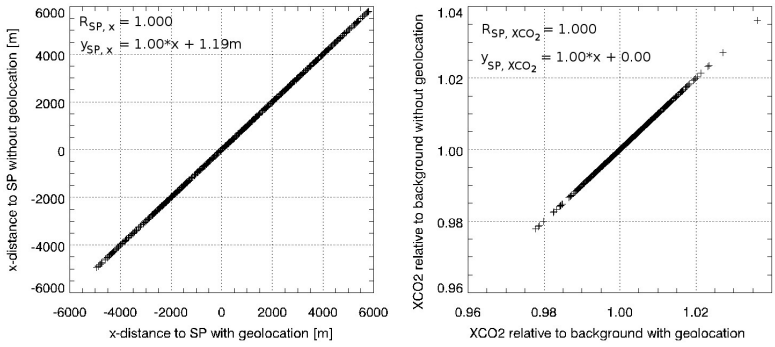

(d) As in (b) but for Schwarze Pumpe (SP) 2007.

Figure 4.2: Comparison of the re-retrieved flight over Jänschwalde (JW) and Schwarze Pumpe (SP) in 2007 with the already published flight over Jänschwalde and Schwarze Pumpe in 2007. Values with an combined RMS value larger than 0.95 % are not depicted and were also not used for further calculations. Values of $XCO_2(CH_4)$ are smoothed by a 3-point moving average due to the noisy character of that dataset. The 1-σ precision of the measured columns with respect to the background is $\sim 0.83\,\%$ (Krings et al., 2011).

The data gaps in fig. 4.2a and 4.2c are due to filtering processes during the retrieval. If the signal strength, determined by the amount of counts, in one spectrum is too low (< 3000 counts) or too high (> 55000 counts), it will not be considered because it might be too noisy and saturated, respectively. Additionally, if the combined RMS-value $\left(\sqrt{RMS^2(CO_2) + RMS^2(CH_4)}\right)$ based on the single RMS values (chap. 4.7) of one readout is lager than 0.95 %, that readout will also be disregarded. That means for one measurment consisting of ten readouts, that a measurement is only displayed if, at least, 6 out of 10 readouts are valid.

4.2 The measurement flight of 2011

In this section, the new column-averaged dry air mole fractions of CO_2 of the flight in 2011 are shown.
For that, the first part deals with the extraction of the parametres solar zenith angle (SZA), flight altitude, surface elevation, background mole fractions of CO_2 and CH_4, which were needed for the general state of the atmosphere at time of overflight and linearization point, respectively. Compared to the already published flight from 2007, where they were just adopted from Krings et al. (2011), for 2011, they were still to be extracted from the measurement files.
On basis of these parametres, the $XCO_2(CH_4)$ has been derived from the measurements, as described in the second part.

4.2.1 Target description and flight parametres of 2011

The flight from 2011 was part of a campaign carried out at the end of April beginning of of May 2011. The specific flight analyzed here took place on 29 April 2011 and included overflights of the power plants Jänschwalde, Schwarze Pumpe and the landfill Schöneiche. In the following, first retrieval results from the Jänschwalde and Schwarze Pumpe overflight are presented. Until now, the power plant provider has not provided us with the emission rates.
The weather conditions differed from that in 2007. While the sky was nearly cloud free, except a very thin homogeneous cirrus, strong surface winds were blowing from north east. A more quantitative discussion on the wind conditions can be found in chap. 5.3.
In order to choose the correct input parametres for the reference radiative transfer model computed with SCIATRAN, the flight track was studied with respect to time of overflight, the resulting solar zenith angle, stability of flight altitude and surface elevation. This has been done for both power plants Jänschwalde (fig. 4.3) and Schwarze Pumpe (fig. 4.4) separately in order to consider changing conditions during the flight.

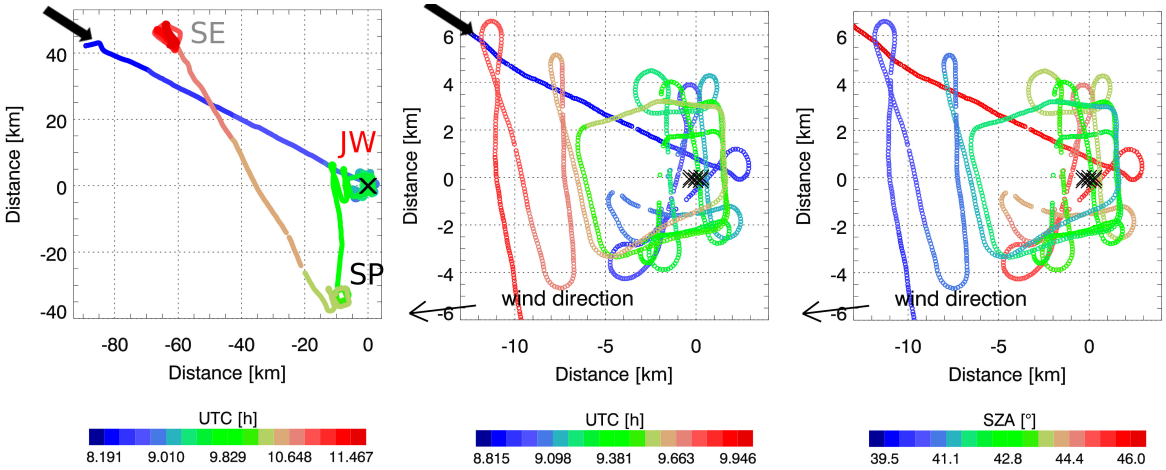

(a) Left panel: shows the whole flight track, whereas the thick arrow highlights the starting point. The colour code of the circles is time (UTC, blue: early morning, red: midday). The location of the power plant Schwarze Pumpe (SP) and landfill Schöneiche (SE, not further considered) are also shown. Middle Panel: the same as left panel but restricted to the power plant location of Jänschwalde (JW). Right panel: solar zenith angle (SZA) along the flight track.

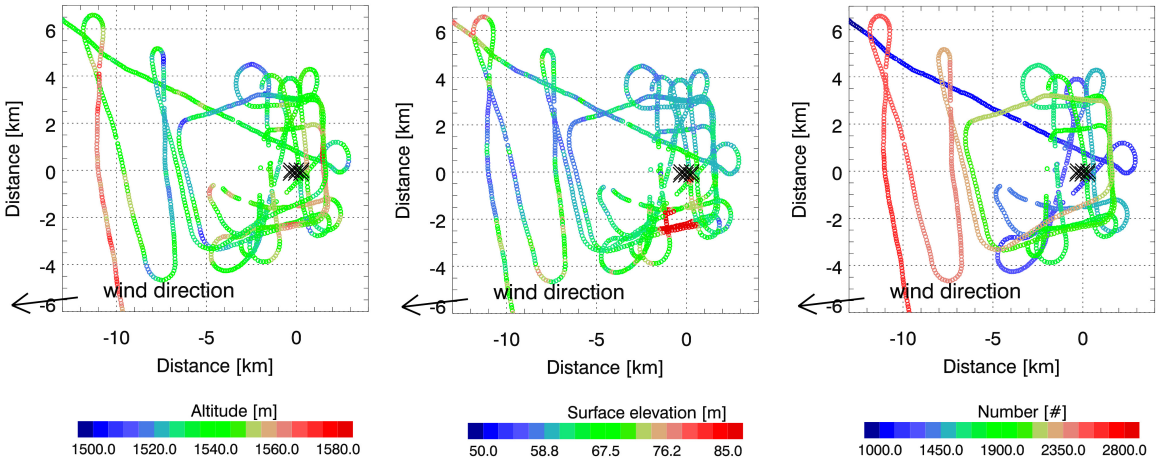

(b) Left panel: shows the flight altitude of the aircraft along the track. The mean altitude was 1.54 km ± 14 m, whereas the lowest and highest altitude were 1.50 km and 1.58 km, respectively. Middle panel: depicts the surface elevation extracted from the Shuttle Radar Topography Mission (SRTM) Dataset version 2.1 (http://dds.cr.usgs.gov/srtm/version2_1/). The mean elevation was 72 m ± 20 m, whereas the lowest and highest elevation were 54 m and 152 m, respectively. Right panel: the number of the measurement. Both quantities standard deviation and peak-to-peak value serve as a measure of variability.

Figure 4.3: The plots show important parametres as needed for the radiative transfer model, which were determined along the flight track for the year 2011. Each circle corresponds to a measurement. Red circles denote large values and blue circles denote small values. The thin black arrow denotes wind direction. The crosses represent the power plant's stacks and, therefore, the location of the power plant Jänschwalde.

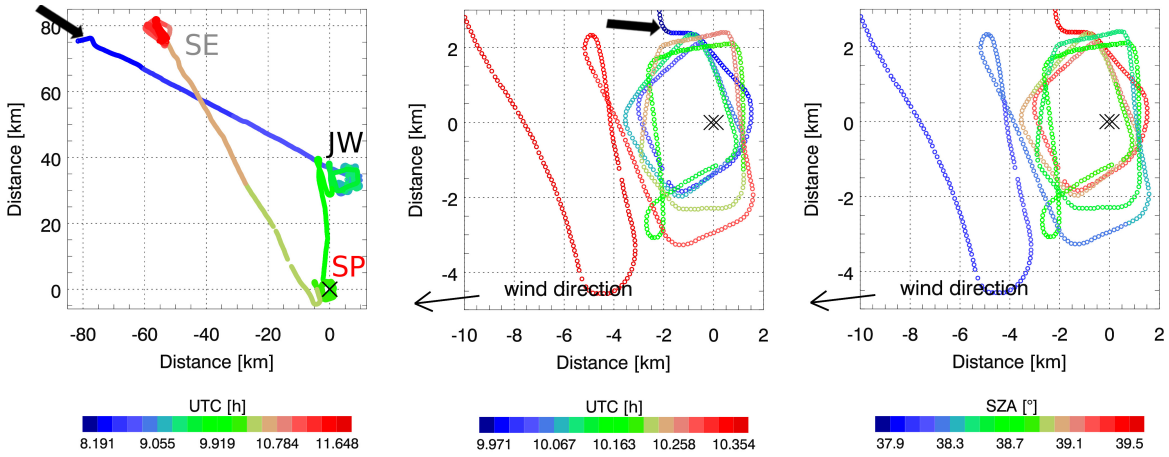

(a) Left panel: shows the whole flight track, whereas the thick arrow highlights the starting point. The colour code of the circles is time (UTC, blue: early morning, red: midday). The location of the power plant Jänschwalde (JW) and landfill Schöneiche (SE, not further considered) are also shown. Middle Panel: the same as left panel but restricted to the power plant location of Schwarze Pumpe (SP). Right panel: solar zenith angle (SZA) along the flight track.

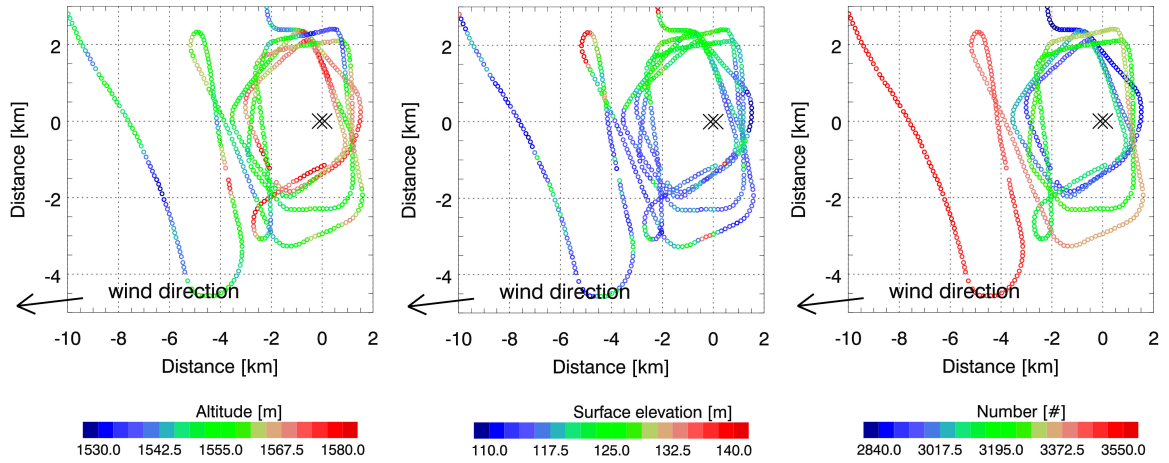

(b) Left panel: shows the flight altitude of the aircraft along the track. The mean altitude was 1.56 km ± 11 m, whereas the lowest and highest altitude were 1.53 km and 1.59 km, respectively. Middle panel: depicts the surface elevation extracted from the Shuttle Radar Topography Mission (SRTM) Dataset version 2.1 (http://dds.cr.usgs.gov/srtm/version2_1/). The mean elevation was 112 m ± 18 m, whereas the lowest and highest elevation were 62 m and 159 m, respectively. Right panel: the number of the measurement. Both quantities standard deviation and peak-to-peak value serve as a measure of variability.

Figure 4.4: As in fig. 4.3 but for Schwarze Pumpe 2011.

By analyzing these data, it was possible to estimate appropriate parametres for the simulation of the spectrum at the linearization point, which describes the atmospheric state and flight properties, at and around the power plants Jänschwalde and Schwarze Pumpe (tab. 4.1). The parametres aircraft altitude, surface elevation and SZA for the flight in 2011 were derived from fig. 4.3 and 4.4.

- **SZA (JW:** 41.0°**, SP:** 38.5°**)**: it was chosen so that it fits values downwind of the power plants best.

- **flight altitude (JW:** 1.54 **km, SP:** 1.56 **km)**: mean value in the area of the power plants was used, whereas a small standard deviation of 13 m (JW) and 11 m (SP) and a maximal and minimal altitude of 1.50 km and 1.58 km (JW) and 1.53 km and 1.58 km (SP), respectively, indicate a rather stable flight.

- **surface elevation (JW:** 0.06 **km, SP:** 0.11 **km)**: mean value of surface elevation was 72 m but, as seen in the middle panel of fig. 4.3b, it was influenced by a high mountain (152 m) south of the power plant and, therefore, the actual value for the region downwind of the power plant was slightly lower (JW). In case of SP, the mean value was 112 m with a standard deviation of 18 m and a minimum and maximum elevation of 62 m and 159 m respectively.

- **albedo (JW and SP:** 0.18**)**: typical albedo over land/vegetation as used for the WFM-DOAS retrieval by SCIAMACHY (Schneising et al., 2011).

- **aerosol scenario (JW and SP: urban)**: urban aerosol scenario, following the properties and nomenclature of Hess et al. (1998).

- **mixing ratio of CO_2 (JW and SP:** 393 **ppm)**: derived from the 4 stations (tab. 4.2) Bialystok, Bremen, Garmisch-Partenkirchen and Karlsruhe of the Total Carbon Column Observation Network (TCCON) (Wunch et al., 2011). Therefore, daily mean values were calculated around the 29.04.2011 (from 14.04.2011 to 14.05.2011) and from that, a weighted monthly mean was derived. When the daily mean was further away in time from the flight day, it also contributed less to the monthly mean than e.g., the daily mean on the flight day directly. This mean value was then used to scale the US standard atmospheric profile of carbon dioxide (also compare to fig. 3.5).

- **mixing ratio of CH_4 (JW and SP:** 1779 **ppb, surface value of** 1840 **ppb)**: based on TCCON (similar to carbon dioxide).

	Bialystok	Bremen	Garmisch-Partenkirchen	Karlsruhe	mean value
XCO_2	393.3 ppm	392.9 ppm	392.1 ppm	393.4 ppm	392.9 ppm
XCH_4	1786.6 ppb	1778.0 ppb	1770.5 ppb	1782.1 ppb	1779.3 ppb

Table 4.2: Depicted are the monthly means of column-averaged dry air mole fraction of CO_2 and CH_4 for each used station around the flight day and finally the mean values, which were used in the radiative transfer model for the linearization point and to scale the US standard profiles (compare to fig. 3.5), respectively.

4.2.2 XCO_2 of 2011

In the next step, the measurements and the modeled spectrum, which is based on the previously obtained flight parametres, were used to derive the profile scaling factors by applying the method described in chap. 3.2.1, and from that, the normalized column-averaged dry air mole fractions (chap. 3.2.2).

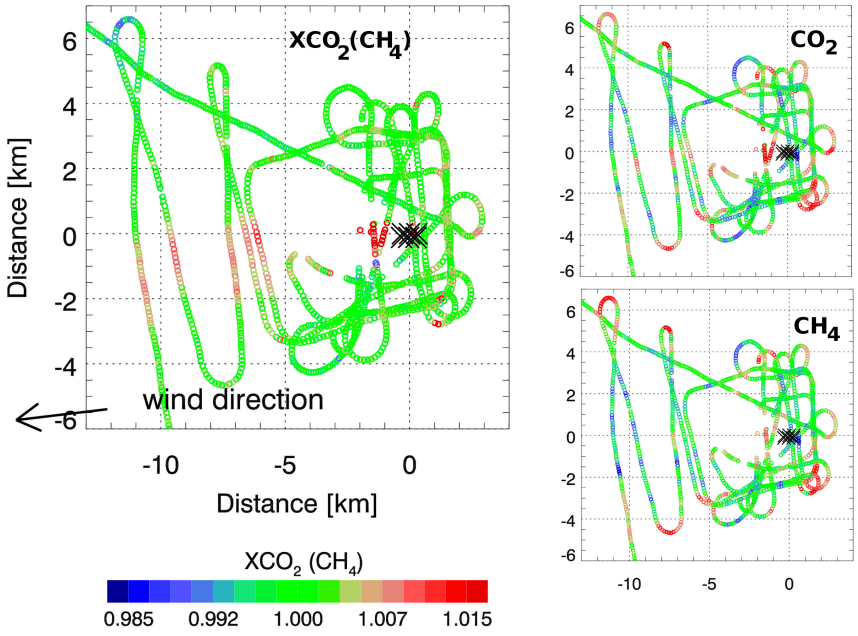

Figure 4.5: Presented are the retrieval results for the power plant Jänschwalde for the overflight in 2011. Left panel: shown are the retrieved column-averaged dry air mole fractions of CO_2 with the aid of the CH_4-proxy method relative to the assumed background. The crosses are the 6 cooling towers emitting flue gases. Right panel: depicted are the profile scaling factors of CO_2 and CH_4 in arbitrary units, separately. They are also corrected by a 100-point moving average, which was not used for the quantitative analysis, to remove the influence if the SZA for visual inspection.

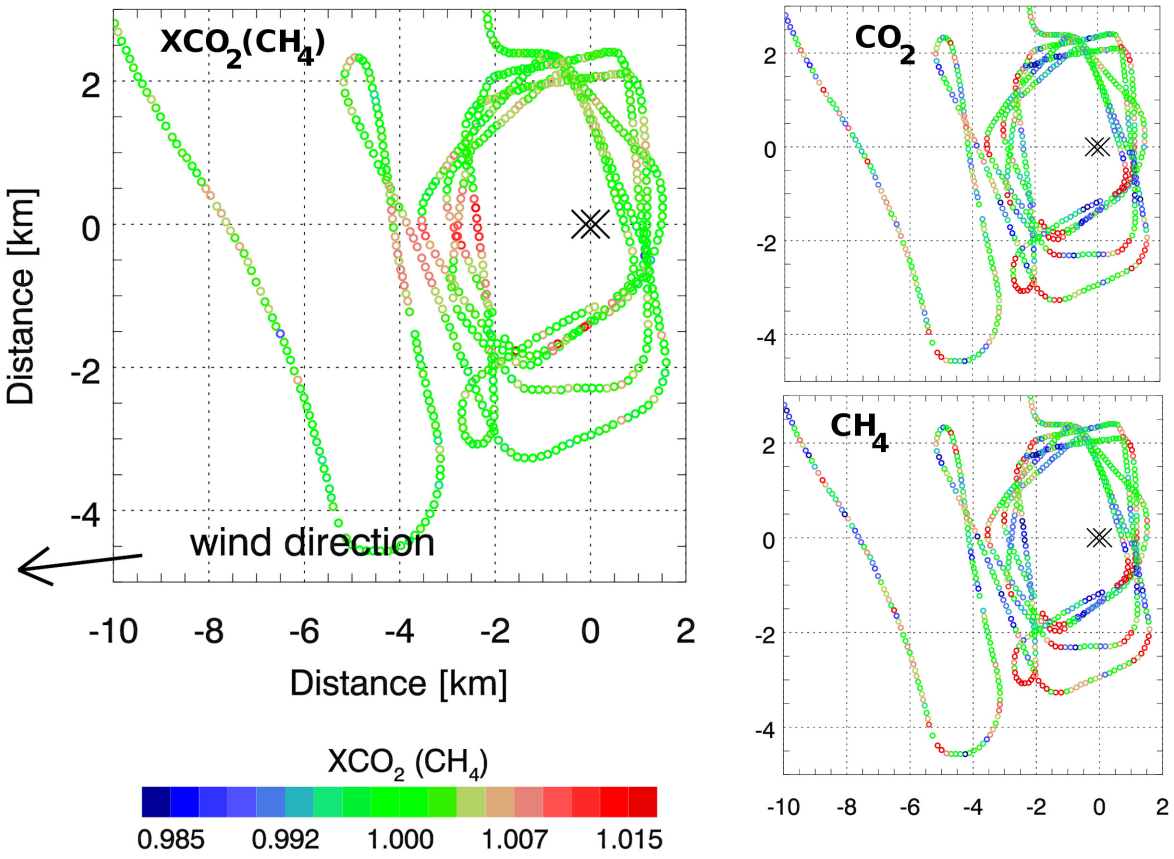

Figure 4.6: As in fig. 4.5 but for Schwarze Pumpe 2011.

The profile scaling factors of methane and carbon dioxide can separately be seen on the right panels in fig. 4.5 and 4.6. The intermediate result, the column-averaged dry air mole fraction of CO_2 with respect to CH_4, is shown in the left panel of fig. 4.5 and 4.6. The filter criteria are similar to the year 2007. That is, a readout is only valid, if its signal strength is between 3000 counts and 55000 counts. In terms of the combined RMS value, no additional filter has been applied because of the increased data quality (also see chap. 4.3.2). The 1-σ precision of the retrieved column-averaged dry air mole fractions of carbon dioxide with respect to the background is $\lesssim 0.4\,\%$ in 2011. It was calculated on basis of 400 measurements taken in an area without any emissions. Hence, varations in the columns are mainly due to noise of the instrument.

4.3 Comparison of the 2007 and 2011 data set

In the following part, the applicability of the CH_4-proxy method in terms of the column-averaged dry air mole fractions of CO_2 to the data from 2011 is discussed. Furthermore, the data quality of the flights in 2007 and 2011 are compared.

4.3.1 The methane-proxy method $\left(\mathbf{XCO_2(CH_4)}\right)$

Fig. 4.5 and 4.6 shows the advantage of the CH_4 proxy method, in case of a power plant when no CH_4 sources or sinks are expected.
Both PSFs of CO_2 and CH_4 are influenced in a similar way by light path errors due to their spectral closeness. This is important, for example, for the parametre SZA. In the right panels its influence cannot be seen because it has visually been removed by a 100-point moving average. Without the average, as applied in the quantitative analysis, correct profile scaling factors would only be delivered during a narrow time window around the SZA chosen in the modeled spectrum. As the right panels in fig. 4.3a and 4.4a show, it changed by 9° from the beginning of the flight over Jänschwalde to the end of the flight over Schwarze Pumpe. This change was partly considered by using two radiative transfer models, at 41.0° and 38.5°, but the diurnal variation could still be seen in the single PSFs without the moving average. For example, a higher SZA than the assumed one of 41.0° (for JW) in the morning, led to an enhanced light path through the atmosphere because of the lower sun. The longer light path led to more absorption due to methane and carbon dioxide which is not accounted for in the retrieval/modeled spectrum. Therefore, the correct profile scaling factors for the single columns are only given where the actual SZA matches the one of the modeled spectrum. The advantage of the CH_4-proxy method is that by dividing the CO_2 columns by the CH_4 columns, the light path errors, which are not accounted for in the model explicitly, cancel out to a large extent because the wrong enhancement (or detraction) due to a wrong SZA occurs in both single columns similarly. This assumption is also valid for 2007, where, in a first approximation, only one model was used for both targets.
The same is true for the remaining structure in the right panels of fig. 4.5 and 4.6. Features which occur in the PSFs of CO_2 and CH_4 simultaneously, triggered by a deviation of surface elevation, flight altitude, additional aerosols or thin cirrus clouds in the atmosphere from the previously assumed values in the model, affect both gases in a similar way and they can be removed by the CH_4-proxy method to a large extent. Krings et al. (2011) also showed the advantage of the CH_4-proxy method compared to the O_2-proxy method and estimated the remaining uncertainties due to reasonable deviations from the modeled spectrum in 2007 by 0.24 % for the CH_4-proxy (tab. 4.3).

Paramtre	Expected Variation	Uncertainty	
		CO_2/CH_4	CO_2/O_2
Solar zenith angle	$\pm 5°$	$\sim -0.15\,\%$	$\sim -0.30\,\%$
Aerosol	urban vs. background	$\sim +0.05\,\%$	$\sim +0.10\,\%$
Surface elevation	$+50\,\mathrm{m}$	$\sim -0.16\,\%$	$\sim +0.42\,\%$
H_2O profiles	$*2$	$\sim +0.02\,\%$	$\sim -0.02\,\%$
Spectral albedo	Aspen vs 0.18	$\sim +0.04\,\%$	$\sim -0.47\,\%$
Cirrus clouds	no cirrus vs AOT 0.1, CTH $12\,\mathrm{km}$	$\sim -0.03\,\%$	$\sim +1.58\,\%$
Aircraft altitude	$\pm 50\,\mathrm{m}$	$\sim +0.06\,\%$	$\sim +0.08\,\%$
total uncertainty estimate		$\sim 0.24\,\%$	$\sim 1.73\,\%$

Table 4.3: The table summarizes the largest uncertainties in the column-averaged dry air mole fraction of CO_2 with the CH_4-proxy and O_2-proxy method by assuming reasonable variations for the flight parametres/conditions. Values are adopted from Krings et al. (2011).

4.3.2 Enhanced data quality in 2011

As discussed in chap. 3.2, the RMS value is an important measure of the fit quality. Comparing the RMS values of 2007 (left panel of fig. 4.7) and 2011 (right panel fig. 4.7), a significant difference can be observed. In general, the fit quality was worse in the past. In 2007, much more fit results exceed the combined RMS threshold of 0.95 % than in 2011 and were filtered out.

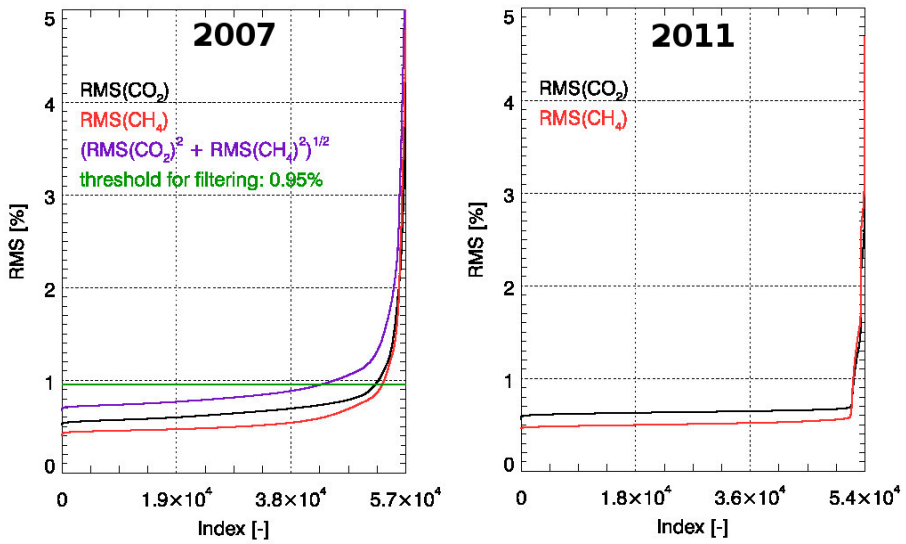

Figure 4.7: Depicted are the RMS values of the $PSFs$ of CO_2 and CH_4 of all readouts from 2007 (left panel) and 2011 (right panel), ordered by size. For 2007, also the used threshold for the combined RMS values are shown, whereas the filtering was not necessary anymore for the 2011 data due to their improved quality.

Although, there are always values with high RMS because the measured spectra might be too noisy or might be saturated in some spectral regions or because of underestimated contributors, their number has significantly decreased. The conclusion is, in 2007, additional effects influenced the fit quality. This can also be observed by comparing the column-averaged dry air mole fractions of 2007 (fig. 4.2a and 4.2c) to 2011 (fig. 4.5 and 4.6, left panels). The $XCO_2(CH_4)$ data in 2011 show less noise than in 2007, even when the 2007 data is smoothed by a 3-point moving average.
The improvement of the fit quality is attributed to the implementation of the homogenizer/spatial scrambler in MAMAP. It ensures that the entrance slit of the SWIR spectrometre is always illuminated evenly, independent of the surface scene. An irregular illumination led to noise observed in the 2007 overflight. This modification was originally proposed by Gerilowski et al. (2011) and has already been reported in Krings et al. (2013).
The large data gaps downwind of the power plant Jänschwalde (fig. 4.5) have been attributed to an area with many lakes (Peitzer Teichlandschaft mit Hammergraben). In general, water surfaces have a low spectral surface reflectance/albedo, which reflect little light back to the telescope. That means, these measurements have been disregarded because of a too small signal strength (< 3000 counts) and not because of too high RMS values and too low data quality, respectively.

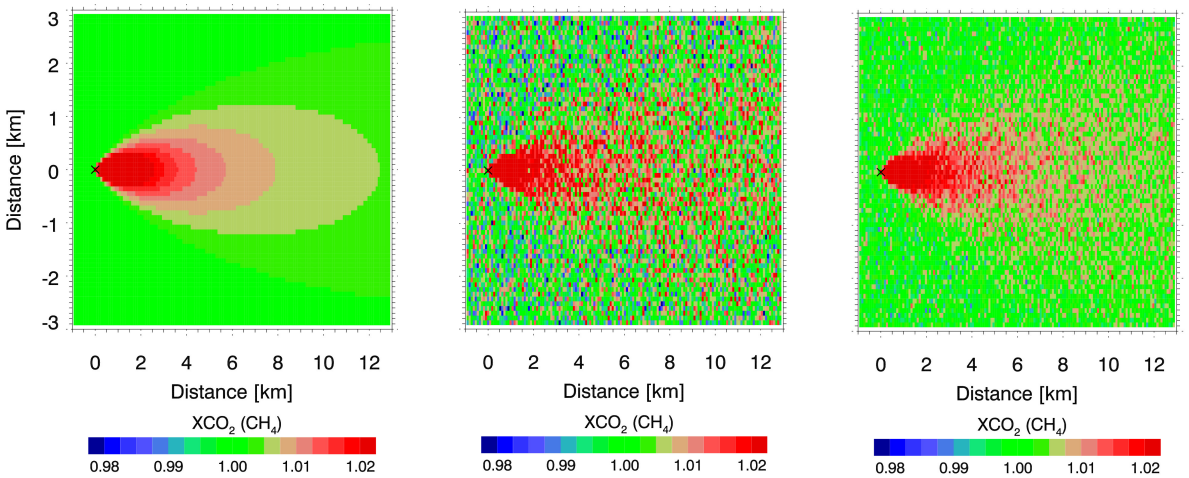

(a) Simulation without noise (same as in fig. 3.9b).

(b) Simulation at noise level for the flight in 2007 ($\sigma = 0.0083$).

(c) Simulation at noise level for the flight in 2011 ($\sigma = 0.0040$).

Figure 4.8: Shown are column-averaged dry air mole fractions of CO_2 relative to the background. The point source is located at $(0, 0)$ marked by a black cross. All simulations are at approx. MAMAP ground scene size ($90\,\mathrm{m} * 90\,\mathrm{m}$), use a mean wind speed u of $5\,{}^{m}/_{s}$, an emission rate of F of $765000\,{}^{g}/_{s}$ and a source width y_0 of $50\,\mathrm{m}$. Atmospheric stability has been assumed to be very unstable (class = A, $a = 213.0$).

Fig. 4.8 compares three simulated CO_2 plumes (integrated column and horizontal extent of a plume according to eq. 3.17). The first one (4.8a) depicts the ideal plume without any noise ($\sigma = 0.0$), whereas the normally distributed noise of 2007 ($\sigma = 0.0083$, compare

to fig. 4.2) has been added to the second one (fig. 4.8b) and the improved noise level of 2011 ($\sigma = 0.0040$, compare to p. 52) to the third one (fig. 4.8c). These are worst case scenarios and, normally, the 1-σ error is slightly below 0.0083 and 0.0040, respectively. The simulations underline the conclusion from the RMS plots (fig 4.7) visually. Due to the higher data quality in 2011 compared to 2007, the noise in the measurements has decreased. Firstly, this results in more measurements, which can be used for the inversion process later due to less rejections, and secondly, the column-averaged dry air mole fractions are less noisy, which leads to a better identification of the plume in the measurements and better single measurement precisions (2007: $\sigma = 0.0083 \rightarrow$ 2011: $\sigma = 0.0040$). Both should also propagate to the emission rate estimates leading to a smaller statistical error in the optimal estimation approach.

Chapter 5

Emission rate results

The column-averaged dry air mole fractions of CO_2 presented in chap. 4 are used to estimate the emission rates for the power plants Jänschwalde and Schwarze Pumpe during measurement campaigns in the years 2007 and 2011. Therefore, the vertically highly resolved profiles from the DWD (chap. 3.3.3) are applied. The vertical plume location is derived from the potential temperature profile (atmospheric stability and vertical Gaussian dispersion model) and from that, a mean wind speed of the plume, which is used in the optimal estimation approach to get the CO_2 emissions (chap. 3.3.2).

5.1 The Jänschwalde overflight 2007

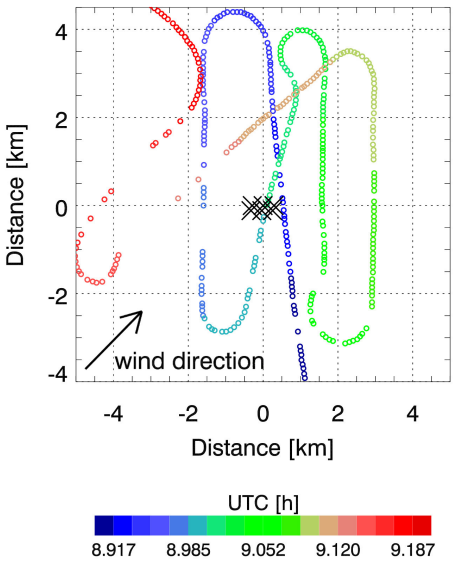

Figure 5.1: Flight pattern around the power plant Jänschwalde (marked by six crosses, one per stack) in 2007. The colours represent the measurement time in UTC.

As discussed in chap. 2.2, the potential temperature is a measure for the stability of the atmosphere and, thus, for the vertical distribution of the plume. The plume rise can be damped or even suppressed dependent on the degree of stability. Fig. 5.2a shows profiles of potential temperature at three different times which were used for the stability estimate at the power plant Jänschwalde in the year 2007, whereby the overflight of the plume took place at 09:00 UTC (compare to fig. 5.1). The profiles represent the conditions at the location of that power plant. The left panel depicts the state of the atmosphere in the lower 6000 m and the right panel zooms in the lower 2500 m. Very pronounced is the increase in potential temperature above 1500 m. This implies the existence of a very stable layer. Comparing it to fig. 2.6, indicates the capping layer, which separates the free troposphere from the planetary boundary layer. The idea is

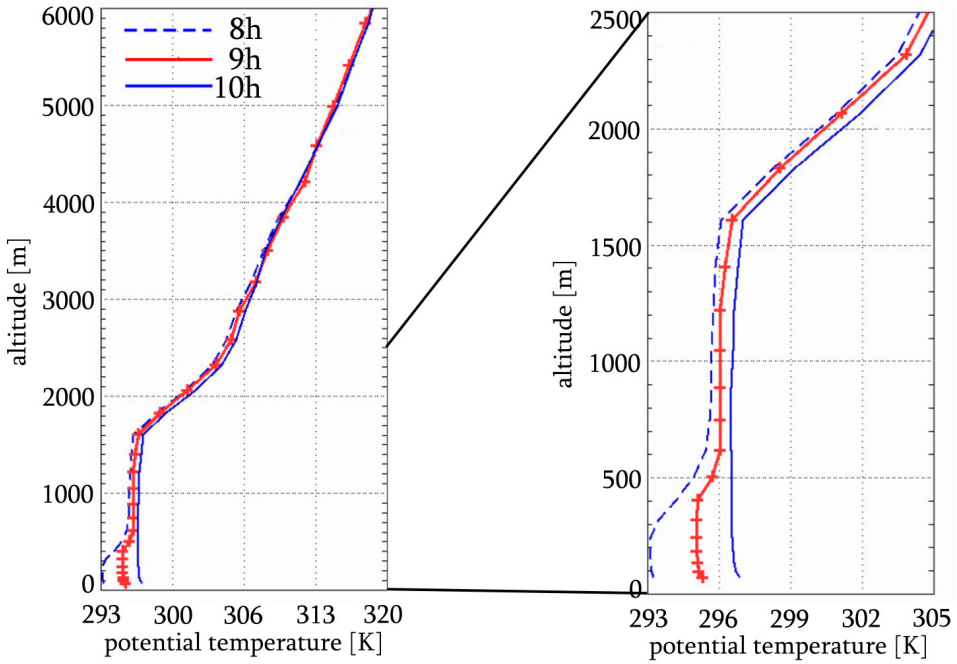

(a) Depicted are the profiles of potential temperature up to an altitude of 6000 m on the left side and a zoom up to an altitude of 2500 m on the right side.

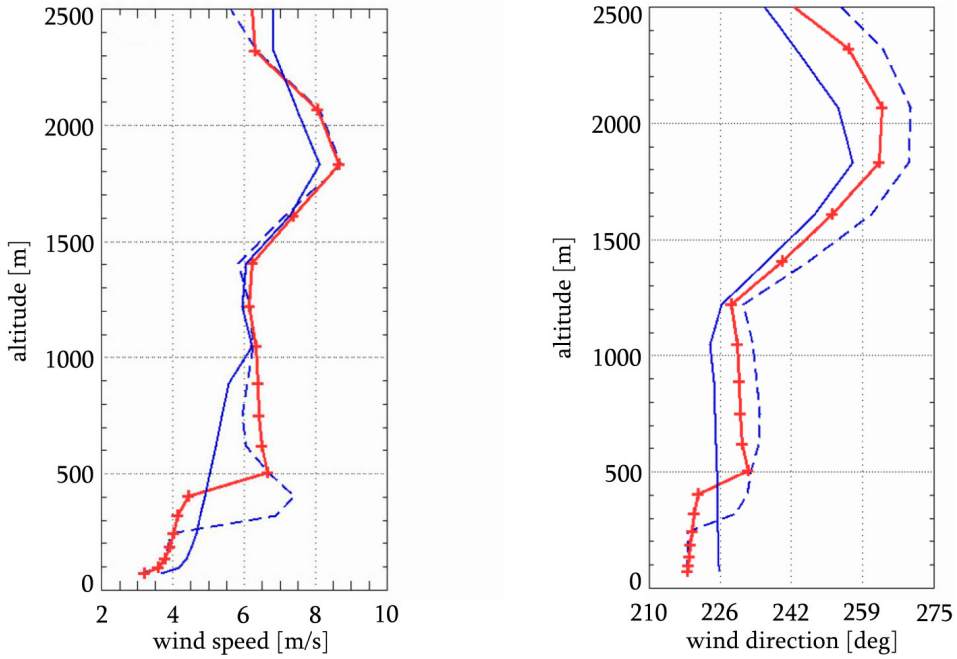

(b) Depicted are the profiles of wind speed on the left side and wind direction on the right side up to an altitude of 2500 m.

Figure 5.2: Shown are the highly resolved vertical profiles from the COSMO-DE model at the location of the power plant Jänschwalde in 2007 at three different times. The overflight took place around 09:00 (solid red line) UTC.

also supported by its temporal constancy, which did not change between one hour before and one hour after the measurement. In a first approximation, the exhaust gases could not penetrate it, at least, during the short time period, the overflight was taking place. The capping layer was not the only feature which might have affected the plume. Around 500 m, the potential temperature was also increasing indicating a second stable layer. In contrast to the distinct one above 1500 m, this layer was quite narrow in altitude and was also dissolving till 10:00 UTC. But, this stable boundary layer (compare to fig. 2.6), which had developed during the night, was still there at 09:00 UTC, and should have modified the plume rise. The kind and strength of its influence is difficult to estimate on basis of the potential temperature profiles (fig. 5.2a). Two extreme cases can be assumed. Firstly, the plume was trapped below 500 m and not able to rise further. But as mentioned before, this layer might not be strong enough. Furthermore, the gases were released at an altitude of 0.17 km (surface elevation of 0.06 km and stack height of 0.11 km) to the atmosphere and they were warmer than the surrounding air. These circumstances might facilitate the rise of the plume and penetration of the 500 m layer, which was followed by a neutral layer till 1500 m.
On basis of this discussion two simulations have been used to estimate the vertical distribution. The first one assumed a reflecting layer at the capping layer at 1500 m (fig. 5.3a) and the second one a reflection layer at the stable boundary layer height at 500 m (fig. 5.3b). Subsequently, a mean wind speed of the plume at each distance x from the source was calculated for both simulations on basis of the horizontally interpolated wind profiles derived from the DWD model (fig. 5.2b, left panel).
These values were then used to calculate the mean wind speed of the whole plume, whereas two different approaches were tested:

1. **entire plume inversion**: mean wind speed and direction were calculated for the whole plume e.g., $0 - 4100$ m for Jänschwalde 2007 (also compare to plume extent in fig. 5.4a, left panel).

2. **single track inversion**: mean wind speed and direction were calculated at and around the distance of each flight track in order to consider their variability.

As fig. 5.3 shows, the vertical plume distribution changes with distance from the source, as expected. That also means, the mean wind speed depends on the distance to the source. Due to different wind speeds in different altitude layers, the wind speed near the source, where the plume is concentrated in a narrow layer, might be completely different from the wind speed further away, where the plume is well mixed. The same is true for wind direction. Therefore, the crossings of the aircraft with the plume downwind of the power plant have been divided into 3 tracks. The distance d_i of each track to the source is determined by the interception point of the flight tracks with the x-axis, after the plume has been rotated in positive x-direction (also compare to fig. 5.4). The track i=1 consists of two overflights whereas track i=2 and 3 consist of only one overflight. For each track i the wind speed v_i is averaged over the distances $d_i \pm \Delta d$. The Δd depends on the slope of the track relative to x-axis. If the track is perpendicular to the axis, it will be very small and vise versa. Then, for each v_i at d_i the emission rates F_i is

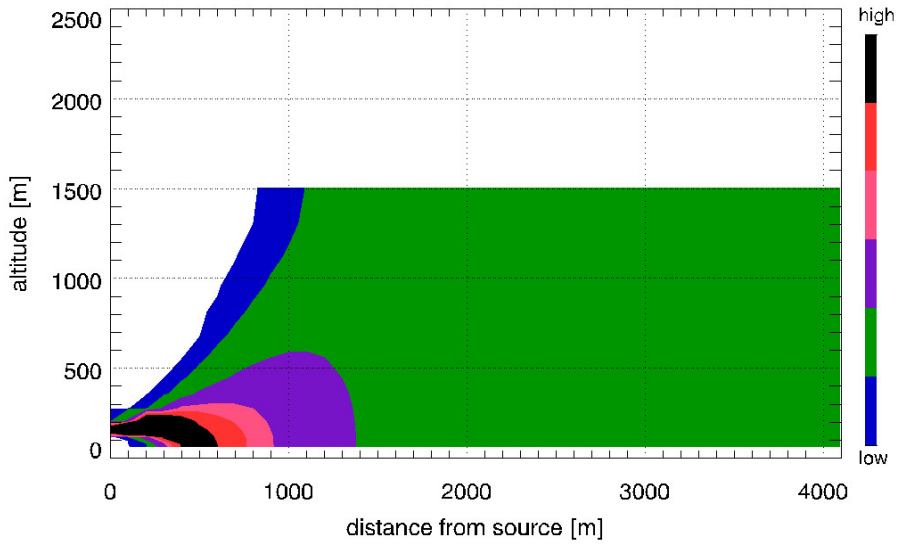

(a) Simulation for reflection layer at approx. trapping layer height of 1500 m (actual height is 1548 m because the altitude grid has been adopted from the DWD model).

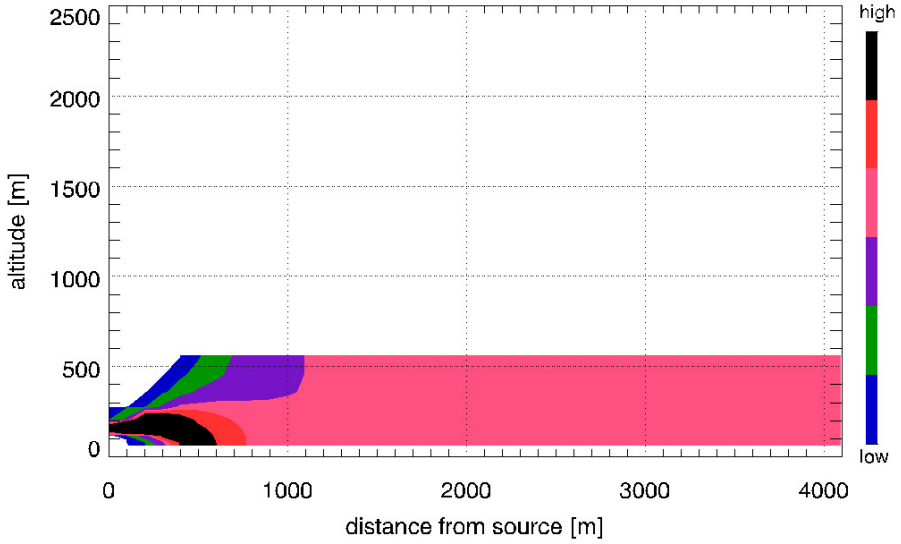

(b) Simulation for reflection layer at approx. stable boundary layer height of 500 m (actual height is 558 m because the altitude grid has been adopted from the DWD model).

Figure 5.3: Shown are simulations of the vertical distribution of the CO_2 plume at power plant Jänschwalde 2007 for two different reflection layers. The emission takes place at an altitude of 0.17 km (stack height of 0.11 km, surface elevation of 0.06 km and source width of 50 m). The distance from the source is on the x-axis in m and the y-axis depicts the altitude in m. Depicted are cross sections of the plume parallel to the centreline or x-axis at $y = 0$ and the colour code represents normalized concentrations with the total column (also compare to chap. 3.3.3), which are independent of the emission rate F and the mean wind speed u. The atmospheric stability has been assumed to be very unstable (class = A; $a = 213.0$; for $x \leq 1000$ m: $c = 440.8$, $d = 1.941$, $f = 9.27$; for $x > 1000m$: $c = 459.7$, $d = 2.094$, $f = -9.6$; also see tab. 3.3).

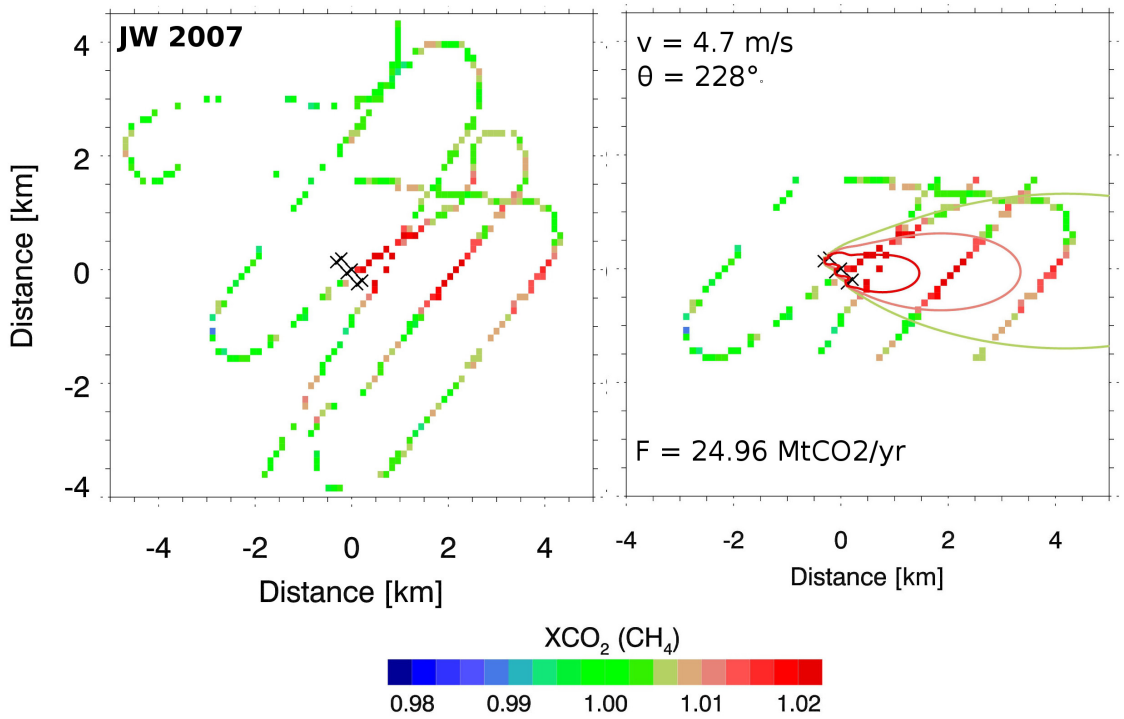

(a) Left panel: same as in fig. 4.2a but rotated so that wind direction points in positive x-direction and gridded. Right panel: only the measurements which have been used for the inversion and the contour lines of the fitted plume are shown ('entire plume inversion').

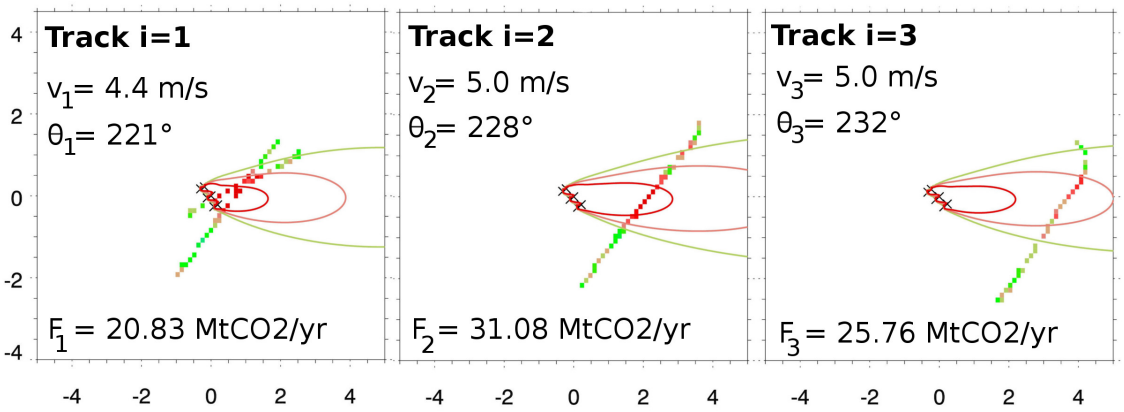

(b) Shown are only the measurements of the specific tracks which have been used separately in the inversion and the contour lines of the resulting fitted plumes ('single track inversion'). The weighted mean emission rate of the three tracks based on their statistical errors is 23.28 $^{MtCO_2/yr}$.

Figure 5.4: The plots show the rotated and gridded $(120\,\mathrm{m} * 120\,\mathrm{m}$ as in Krings et al. (2011)$)$ overflight of the power plant Jänschwalde in 2007 in different configurations. The colour code refers to column-averaged dry air mole fractions of $CO_2(CH_4)$ relative to the background. All parametres and results are also summarized in tab 5.1.

estimated and, finally, the F_{1-3} are averaged to get the final emission rate F. The wind direction is also estimated for each distance d_i.
The wind direction needed plays an important role for the emission rate estimate. Although, it is given by the DWD model (fig. 5.2b, right panel), its uncertainty is about 10° (Krings et al., 2011). Therefore, it was visually derived by rotating the plot of the $XCO_2(CH_4)$ (fig. 5.4) until the whole plume (approach 1, entire plume inversion) or the single tracks (approach 2, single track inversion) were aligned in positive x-direction. The DWD wind direction (fig 5.2b, right panel) was only used for consistency checks.
Fig. 5.4 shows the estimated emission rates for JW 2007 with the main input parametres wind speed and direction and output parametre emission rate. The whole inversion result for the power plant Jänschwalde is summarized in tab. 5.1 on p. 74.

5.2 The Schwarze Pumpe overflight 2007

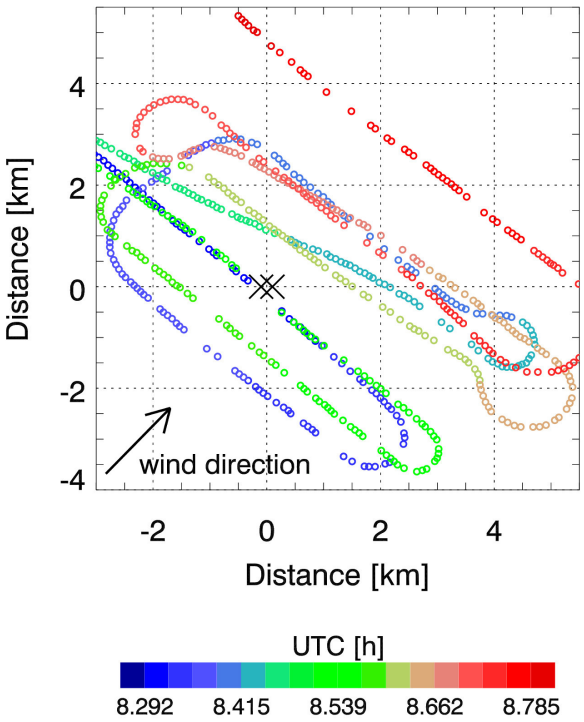

Figure 5.5: As fig. 5.1 but for the Schwarze Pumpe overflight 2007 marked by the two crosses in the middle.

During the overflight of the power plant Schwarze Pumpe, the wind direction significantly changed while crossing the plume (fig. 5.8b). The difference between the first track and the last track was approx. 24° and prohibit the application of the first approach, where an emission rate is calculated for the whole plume. Krings et al. (2011) have applied the 'entire plume inversion' but considered the changing wind direction by rotating the first part of the track in x-direction and, then, rotated the second part (with the second wind direction) in x-direction and bend it to the first one. This has violated the quasi stationary conditions and has introduced additional uncertainties. In case of Jänschwalde, a difference of 11° could be tolerated. Thus, only approach two was used.
Compared to Jänschwalde, the measurements took place between 08:00 and 09:00 UTC, which needed to be considered, whereas also three tracks could be identified. The corresponding three wind speeds v_i at or around the intercept d_i of the tracks were calculated on basis of the wind profiles at 08:00 and at 09:00 UTC and, subsequently, averaged depending on the overflight

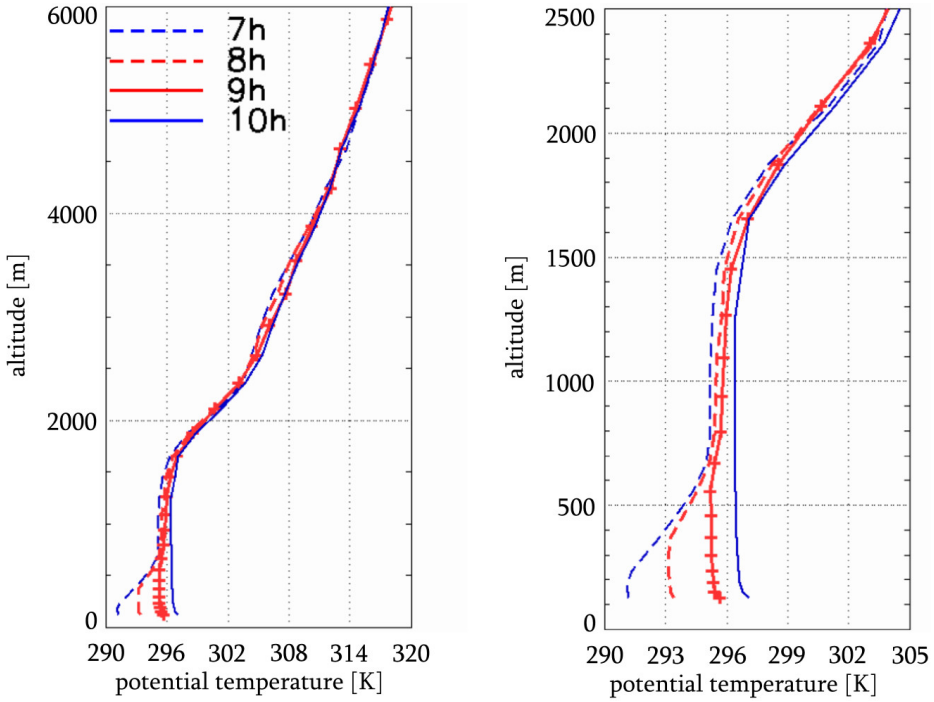

(a) Depicted are the profiles of potential temperature up to an altitude of 6000 m on the left side and up to an altitude of 2500 m on the right side.

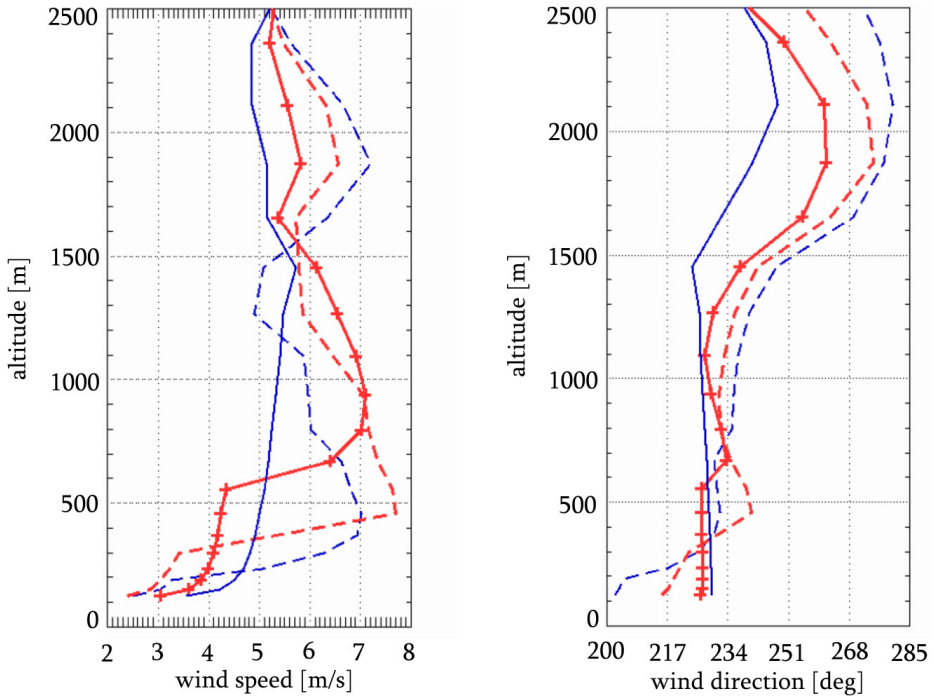

(b) Depicted are the profiles of wind speed on the left side and wind direction on the right side up to an altitude of 2500 m.

Figure 5.6: As fig. 5.2 but at the location of the power plant Schwarze Pumpe in 2007 at four different times. The overflight took place between 08:00 (dashed red line) and 09:00 (solid red line) UTC.

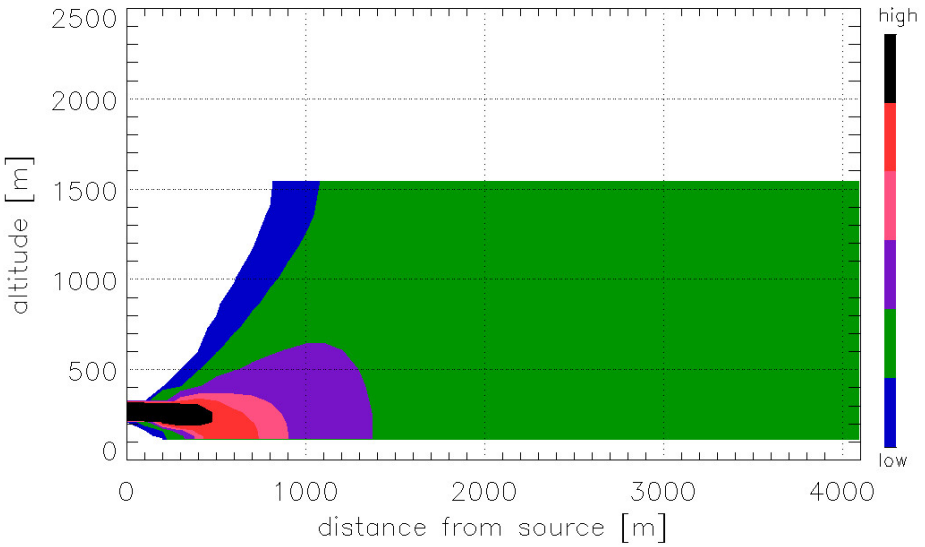

(a) Simulation for reflection layer at approx. trapping layer height of 1500 m (actual height is 1548 m because the altitude grid has been adopted from the DWD model).

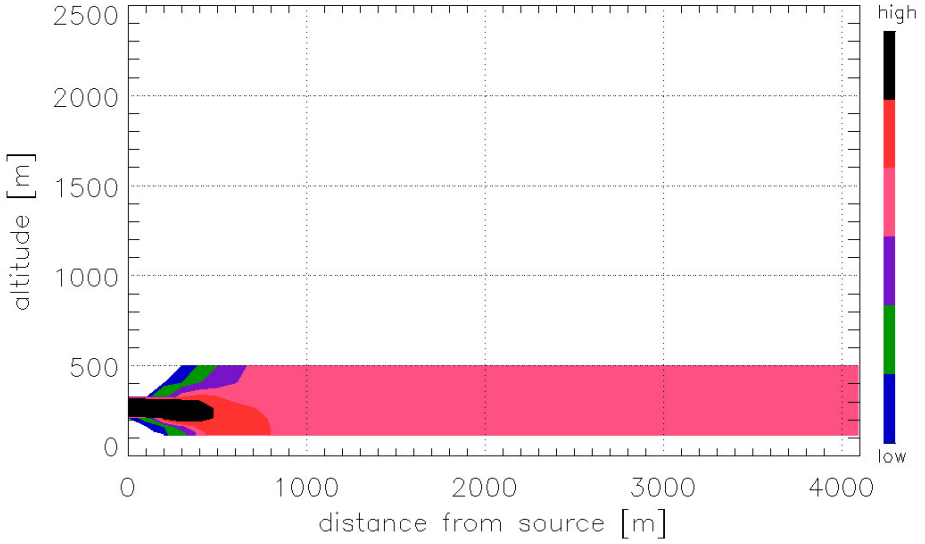

(b) Simulation for reflection layer at approx. stable boundary layer height of 500 m (actual height is 501 m because the altitude grid has been adopted from the DWD model).

Figure 5.7: As in fig. 5.3 but for Schwarze Pumpe 2007. The emission takes place at an altitude of 0.25 km (stack height of 0.14 km, surface elevation of 0.11 km and source width of 50 m).

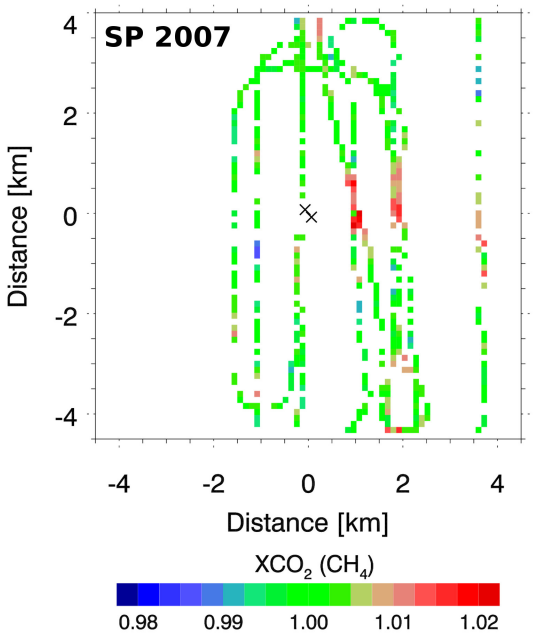

(a) Same as in fig. 4.2c but rotated so that wind direction points in positive x-direction and gridded.

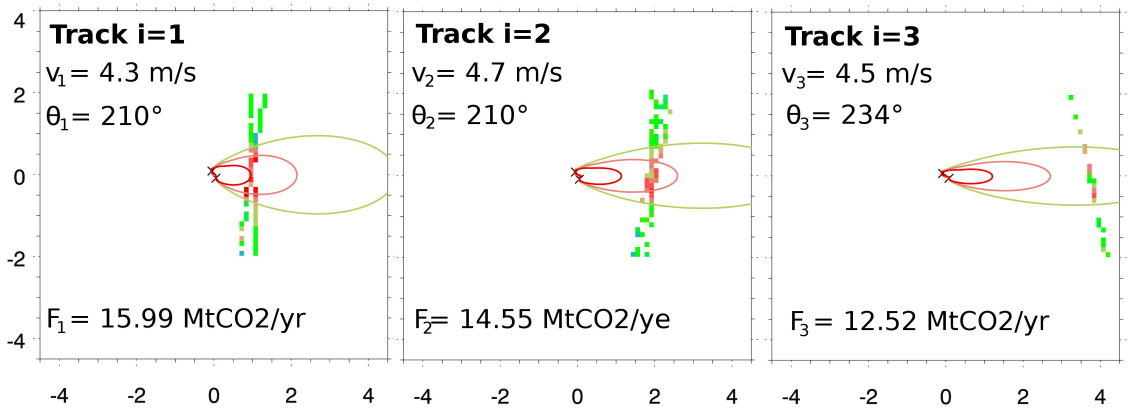

(b) Shown are only the measurements of the specific tracks which have been used in the inversion and the contour lines of the resulting fitted plume ('single track inversion'). The final emission rate based on a weighted mean of the three tracks is 14.98 $^{MtCO_2}/_{yr}$.

Figure 5.8: As in fig. 5.4 but for the power plant Schwarze Pumpe in 2007.

	track intercept at d [km]	Δd [m]	**wind velocity v** $[m/s]$	**wind direction** θ [°]	**emission rate** F $[MtCO_2/yr]$	**statistical error of** F [%]	**difference (reported-measured)**	**stability parametre** a	**statistical error of** a [%]
JW 2007	reported value by provider				$24.125\ MtCO_2/yr$				
entire plume inversion			$4.7\ m/s$	228°	$24.96\ MtCO_2/yr$	8.0 %	+3.5 %	370	11.4 %
single track inversion					$23.28\ MtCO_2/yr$	7.6 %	−3.1 %		
Track 1	0.8 km	500 m	$4.4\ m/s$	221°	$20.83\ MtCO_2/yr$	10.1 %		288	18.6 %
Track 2	2.0 km	500 m	$5.0\ m/s$	228°	$31.08\ MtCO_2/yr$	12.5 %		244	16.0 %
Track 3	3.6 km	500 m	$5.0\ m/s$	232°	$25.76\ MtCO_2/yr$	23.1 %		252	25.3 %
SP 2007	reported value by provider				$13.025\ MtCO_2/yr$				
single track inversion					$14.98\ MtCO_2/yr$	11.9 %	+15.0 %		
Track 1	1.0 km	200 m	$4.3\ m/s$	210°	$15.99\ MtCO_2/yr$	16.31 %		391	16.2 %
Track 2	2.0 km	200 m	$4.7\ m/s$	210°	$14.55\ MtCO_2/yr$	19.4 %		276	20.7 %
Track 3	3.7 km	200 m	$4.5\ m/s$	234°	$12.51\ MtCO_2/yr$	40.3 %		237	34.2 %

Table 5.1: The table summarize the emission rate estimates from the year 2007 of the power plants Jänschwalde (JW) in the upper part and Schwarze Pumpe (SP) in the lower part. Shown are the input parametres wind velocity v and wind direction θ as well as the properties of the single tracks track intercept with the x-axis at d, width Δd and the fitted parametres emission rate F, the stability parametre a and their statistical errors, given by the optimal estimation approach. Third row ('entire plume inversion' of JW): parametres and results for the whole plume ($0 - 4100$ m). Fourth row ('single track inversion' of JW): result of the emission rate and its statistical error, which represents the weighted means from the single tracks Track 1 ($300 - 1300$ m), Track 2 ($1500 - 2500$ m) and Track 3 ($3100 - 4100$ m) on basis of their the statistical errors. Large error means little weight and vice versa. Row 8-12: similar as above but for SP.

time of the tracks. For example, from track i=1 consisting of two single overflights (compare to fig. 5.5), which took place at approx. 08:26 (8.45) UTC and 08:36 (8.62) UTC, respectively, a mean overflight time of 8:31 was calculated. This time served as weight how the wind speed at 08:00 and 09:00 UTC were considered in the mean.
The vertical plume distribution at the power plant Schwarze Pumpe was similar calculated as for Jänschwalde. A stable boundary layer at 500 m and a capping layer at 1500 m were observed and also used as reflection layer heights in the two simulations fig. 5.7a and 5.7b. Additionally, the changed emission height of 0.25 km (surface elevation of 0.11 km and stack height of 0.14 km) needed to be considered.

5.3 The Jänschwalde overflight 2011

The emission rate estimates of the year 2007 show that the inversion and the new wind algorithm work properly and deliver reasonable results. Therefore, it was also applied to the new flight over the power plant Jänschwalde in 2011. For this flight the power plant operator has not provided us with information on the emissions.
In order to calculate the emission rate a test run of the optimal estimation method (chap. 3.3.2) was used to obtain the stability parametre a of the atmosphere/plume at the location of Jänschwalde in 2011 (a is independent of wind speed and emission rate). Compared to 2007 where the conditions were very unstable (class A), for Jänschwalde 2011, an a of 184 indicated a stability between class A (very unstable) and B (moderately unstable) (also compare to tab. 3.2 and 3.3). This was also in good agreement with the potential temperature (fig. 5.9a) which was constantly increasing from the ground to at least 6000 m, with a very pronounced region around 500 m at 09:00 UTC, which had risen to around 800 m at 10:00 UTC marking the stable boundary layer. Thus, in a first approximation, it was assumed that the plume was trapped below 500 m and 800 m, respectively. This seems to be valid because, compared to 2007 where the region between 500 m and 1500 m was neutrally layered, in 2011, the potential temperature was still increasing above 500 m and the whole lower atmosphere was stably layered. The overflight started at 09:00 UTC and ended at 10:00 UTC (also compare to fig 4.3a, middle panel).
Therefore, the vertical plume distribution was calculated for a reflection layer at approx. 500 m at 09:00 UTC, 800 m at 10:00 UTC and for two different stability classes A and B (see fig. 5.10 and see tab. 5.2). Subsequently, these wind speeds were averaged considering all values equally because the overflights of the plume were distributed evenly in time and the stability of 184 is almost in the middle of class A and B.

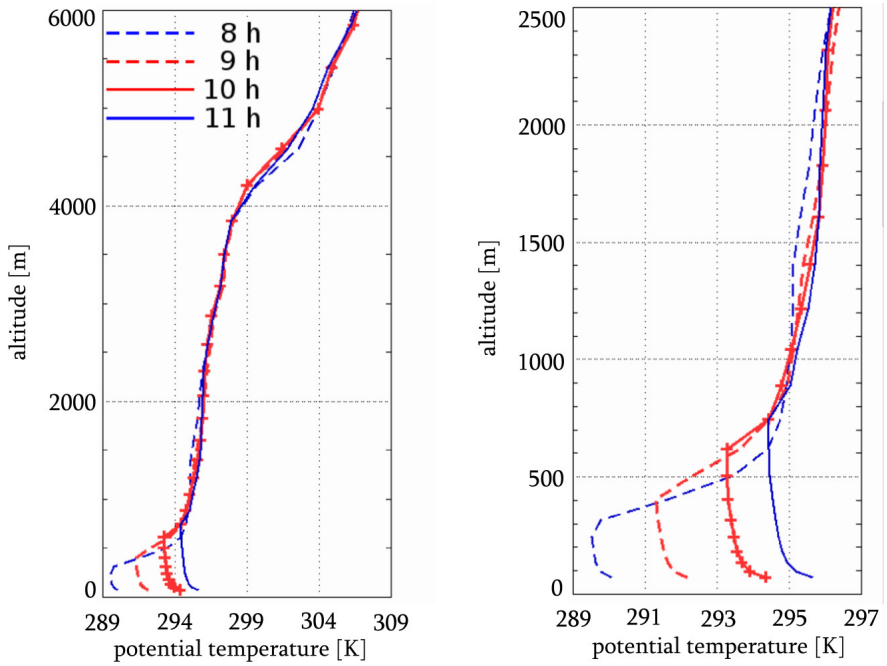

(a) Depicted are the profiles of potential temperature up to an altitude of 6000 m on the left side and a zoom up to an altitude of 2500 m on the right side.

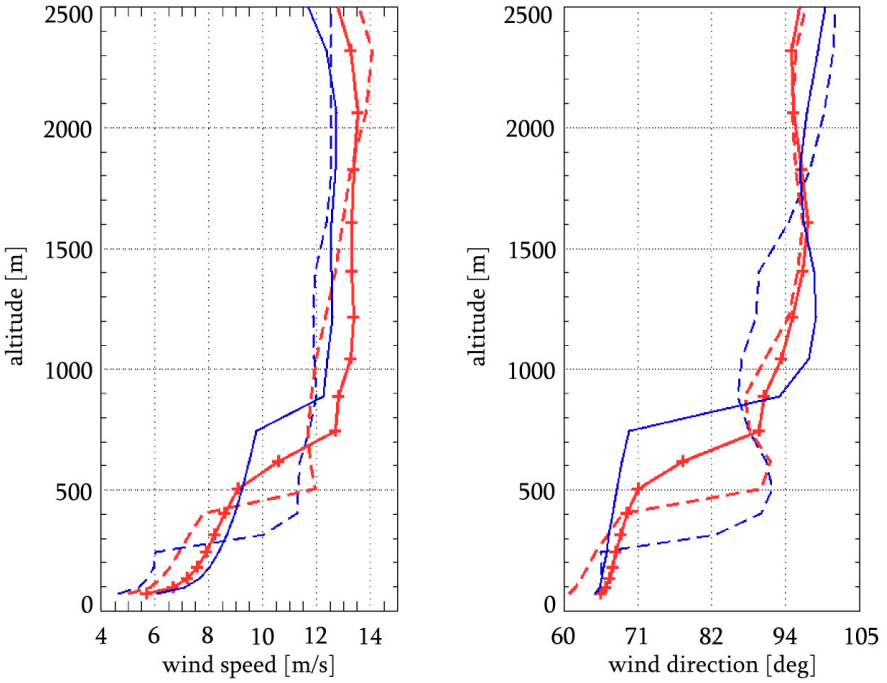

(b) Depicted are the profiles of wind speed on the left side and wind direction on the right side up to an altitude of 2500 m.

Figure 5.9: As in fig. 5.2 but at the location of the power plant Jänschwalde in 2011 at four different times. The overflight took place between 09:00 (dashed red line) and 10:00 (solid red line) UTC.

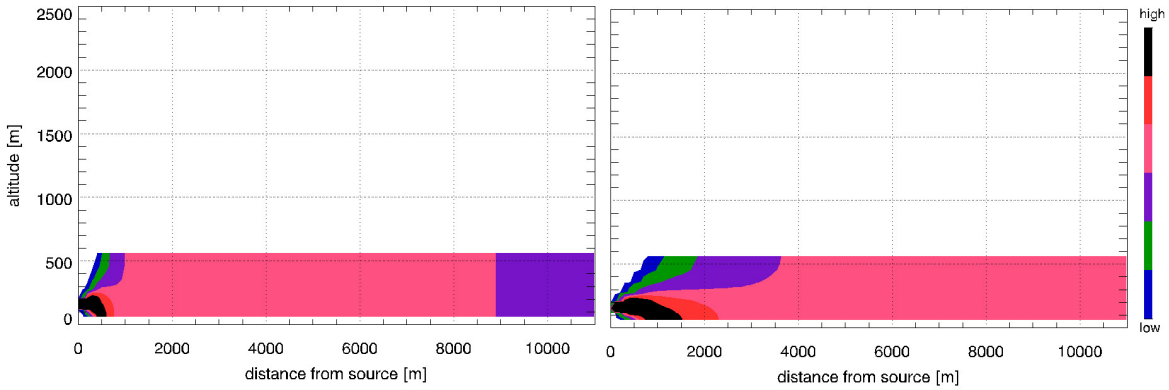

(a) Simulation for reflection layer at approx. stable boundary layer height of 500 m (actual height is 558 m because the altitude grid has been adopted from the DWD model). Left panel: stability class A. Right panel: stability class B.

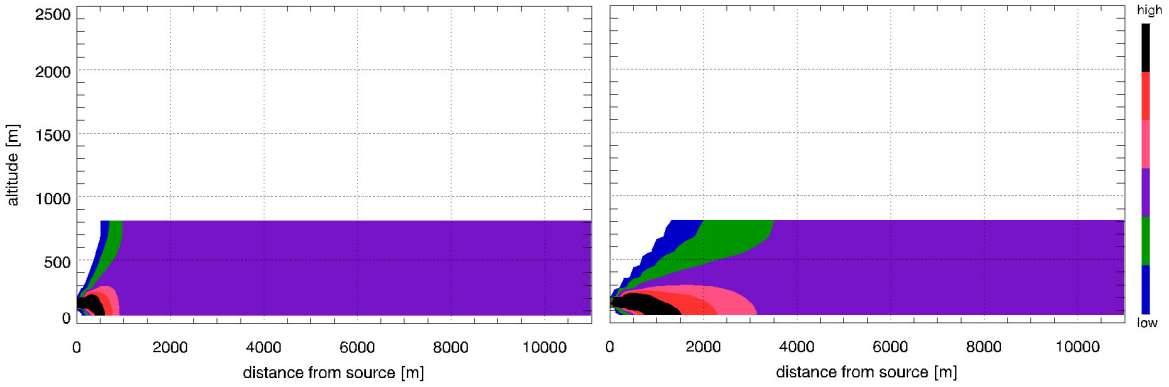

(b) Simulation for reflection layer at approx. stable boundary layer height of 800 m (actual height is 814 m because the altitude grid has been adopted from the DWD model). Left panel: stability class A. Right panel: stability class B.

Figure 5.10: Shown are simulations of the vertical distribution of the CO_2 plume at power plant Jänschwalde 2011 for two different reflection layers and stability classes, similar to fig. 5.3. Compared to Jänschwalde 2007 (compare to 5.3), the maximum distance is 11000 m and not 4100 m. Therefore, the number of the reflection terms T in eq. 3.19 had to be adjusted to 120 for the extreme case: class = A and height = 500 m. The emission takes place at an altitude of 0.17 km (stack height of 0.11 km, surface elevation of 0.06 km and source width of 50 m). The atmospheric stability has been assumed to be very unstable (class = A; $a = 213.0$; for $x \leq 1000$ m: $c = 440.8$, $d = 1.941$, $f = 9.27$; for $x > 1000m$: $c = 459.7$, $d = 2.094$, $f = -9.6$) and moderately unstable (class = B; $a = 156.0$; for $x \leq 1000$ m: $c = 106.6$, $d = 1.149$, $f = 3.2$; for $x > 1000m$: $c = 108.2$, $d = 1.098$, $f = 2.0$; also see tab. 3.3).

	500m		800m	
	A	**B**	**A**	**B**
09:00 UTC	$8.249\,^{m}/_{s}$	$8.126\,^{m}/_{s}$	—	—
10:00 UTC	—	—	$9.443\,^{m}/_{s}$	$9.092\,^{m}/_{s}$

Table 5.2: The four calculated wind speeds on basis of the two stability classes A and B at boundary layer heights of 500 m and 800 m for 09:00 and 10:00 UTC. The final wind speed derived from these values is $8.7\,^{m}/_{s}$

This resulted in a mean wind speed of $8.7\,^{m}/_{s}$ for the whole plume ($0 - 11000m$, entire plume inversion), which was used in the optimal estimation approach (chap. 3.2.2) yielding an emission rate of $22.2\,^{MtCO_2}/_{yr}$ at the time of the overflight with a statistical error of $\pm 6.4\,\%$ for Jänschwalde in 2011 (also compare to fig. 5.11).

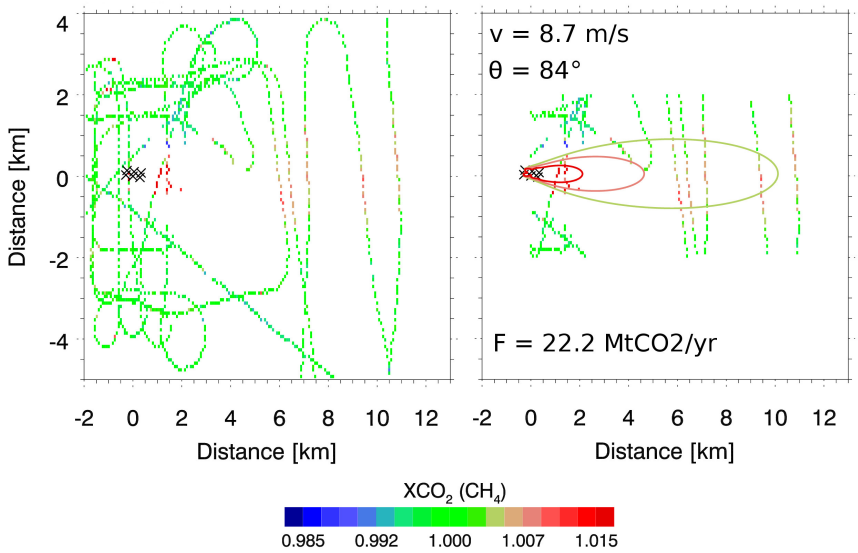

Figure 5.11: The plots show the rotated (wind direction points in positive x-direction) and gridded ($82\,\text{m} * 82\,\text{m}$ pixel, grid size has been adapted to ground scene size of the MAMAP instrument, compare to tab. 3.1) overflight of the power plant Jänschwalde in 2011. The colour depicts the column-averaged dry air mole fraction of $CO_2(CH_4)$ relative to the background. Left panel: similar to fig. 4.5. Right panel: only the measurements which have been used for the inversion and the contour lines of the fitted plume are shown ('entire plume inversion'). The measurements right above the power plant (around (0,0)) have been excluded because, at this position, the plume is quite narrow and a small shift in the position of the gridded pixels leads to a large change in the emission rate estimates and, thus, causes instabilities in the inversion.

5.4 Applicability of the Gaussian plume model and typical uncertainties

The newly developed algorithm for deriving the mean wind speed of a specific plume works with sufficient reliability as it can be seen on the emission rate estimates for the year 2007 (tab. 5.1). The advantage of the Gaussian plume model is that it takes all measurements of a plume into account and, thus, minimizes the influence of outliers caused by small atmospheric turbulences. The more measurements/pixels are available describing the plume, the smaller the statistical uncertainty of the resulting emission rate is. It also appropriately handles small deviations from a mean wind direction within a plume of the single tracks as happened for Jänschwalde 2007 $\left(\Delta\theta = 11°\right.$, also compare to fig. 5.4$\left.\right)$ but not for Schwarze Pumpe 2007 $\left(\Delta\theta = 24°\right.$, also compare to fig. 5.8$\left.\right)$. The 'entire plume inversion' should be preferred to the 'single track inversion'.
The disadvantage is that a mean wind speed is needed, which is assumed to be constant for the whole plume. A good approximation is the mean wind speed based on the DWD model data, although it is rather sensitive to the chosen reflection layer height. This height has been determined with the aid of the potential temperature profiles. If there was a stable layer near the ground e.g., around $500 - 1000$m, it was assumed that the hot gases could penetrate this layer to some extend, whereas they could not penetrate a stable layer higher up e.g., around 1500m, because they had already cooled down. Of course, this assumptions are only valid to a certain degree. The penetration depth depends on the strength of a stable or inversion layer, as well as on the temperature of the released gases, which are both difficult to assess on basis of the current data. Furthermore, even if the plume is able to penetrate the lowest stable layer to a certain degree, it might cool and sink again at a certain distance from its source, which has been neglected in this study.
In order to give an estimate of the uncertainties related to the new vertical profiles, each target is discussed in some detail in the following. The main points are the error of the chosen reflection heights and how it propagates to the mean wind speed and the emission rate estimates (for JW and SP 2007) as well as a small deviation of the mean wind direction for the whole plume and the influence of the enhanced data quality and changed ground scene size in 2011 compared to 2007 on the example Jänschwalde 2011.

Jänschwalde 2007

To investigate the uncertainty of the penetration depth in the lowest stable layer the reflection layer height has been varied by two altitude steps based on the vertical DWD grid in the case of Jänschwalde 2007.
That means, instead of having the reflection layer at approx. 500 m (yields: $4.27\,{}^{m}/_{s}$), it has been lowered to approx. 400 m ($3.84\,{}^{m}/_{s}$, $-10\,\%$) and 320 m ($3.78\,{}^{m}/_{s}$, $-11\,\%$), and

lifted to 620 m (4.61 m/s, +8 %) and 750 m (4.82 m/s, +13 %). The values in brackets represent the wind speeds for the whole plume/distance (4100 m) at 9 o'clock UTC in absolute values and the deviation from the used one of 4.27 $^{m}/_{s}$ (not comparable to mean wind speed of 4.7 $^{m}/_{s}$ in fig. 5.4a because it has already been averaged over values of the lower (500 m) and higher (1500 m) reflection layer). Averaging these values also with the wind speed of the higher reflection layer yields a range of wind speeds from 4.5 to 5.0 $^{m}/_{s}$, or −4 % and +6 % compared to the 4.7 $^{m}/_{s}$, repectively. Additionally, the error of the wind speed itself given by the DWD is about 0.9 $^{m}/_{s}$ (Krings et al., 2011). These uncertainties propagate linearly to the final emission rate estimates of Jänschwalde 2007.

Schwarze Pumpe 2007

Whereas, for the power plant Jänschwalde 2007, both methods 'entire plume inversion' and 'single track inversion' have missed the reported emission rate of 24.125 $^{MtCO_2}/_{yr}$ by only up to 3.5 % (Krings et al. (2011) 'entire plume inversion' overestimated the emission by 8.3 % with a statistical error of ±7.0 %), the calculated emission rate for Schwarze Pumpe 2007 overestimates the reported value of 13.025 $^{MtCO_2}/_{yr}$ by 15 % (Krings et al. (2011) 'modified entire plume inversion' underestimated the emission by 9.0 % with a statistical error of ±12.4 %). The relativly large change in wind direction by 24° during the overflight, which is also a violation of the basic assumption in order to use the Gaussian plume model, only allowed the application of the method 'single track inversion'.
This deviation might have its origin in the calculation of the mean wind speed. As already discussed, the overflight took place between 08:00 and 09:00 UTC, whereas a lower reflection layer height has been assumed at around 500 m (as for JW) for both times. Thus, the hot plume was able to penetrate the stable layer approx. 100 m before it got reflected. Having a closer look to the wind speed profile in fig. 5.6b shows that above 300 m the wind speed is significantly increasing at 09:00 UTC. That means, if the lower reflection height has wrongly been assumed to be too high e.g., at around 500 m, the wind speed is also significantly too high and, therefore the emission rate estimate is too high. A second uncertainty is the lower reflection layer height at 10:00 UTC. The potential temperature profile (fig. 5.6b) actually only shows a minor increase around 500 m but the wind speed is also significantly changing at that altitude indicating a change in the atmospheric layering. That means, it could already have be vanished by 10:00 UTC.

Jänschwalde 2011

For 2011, the reported values from the power plant provider are not available. If it is assumed that the emission had not changed, the calculated rate for the target Jänschwalde of $22.2\,{}^{MtCO_2}/_{yr} \pm 6.4\,\%$ would be 7.9% too low.
In terms of the reflection layer height, only one layer has been chosen (instead of 2 as for 2007), which could not be penetrated completely by the gases due to the quite stable conditions on that day (compare to potential temperature profile in fig. 5.9a), but, maybe, to some extent. Moreover, it was also growing from 09:00 to 10:00 UTC during the overflight.
To investigate the influence of the wind direction on the inversion, the value has been varied by $\pm 5°$ around 84°. The resulting rates deviate by $-3.3\,\%$ for $-5°$ and $+13.0\,\%$ for $+5°$ from $22.2\,{}^{MtCO_2}/_{yr}$ at 84°.
Comparing the statistical error of 6.4 % from Jänschwalde 2011 to the value of 8.0 % from Jänschwalde 2007 only shows a slight decrease despite the enhanced data quality. This is connected to the simultaneously changed ground scene size from $120\,m * 120\,m$ (2007) to $82\,m * 82\,m$ (2011). In 2007, the grid had approx. 4 times the size of the MAMAP ground scene, which led to an additinal smoothing. This was necessary because of the noisy data in 2007 but not anymore for 2011. Thus, the grid size has been adapted to the real MAMAP ground scene size of $28\,m * 82\,m$ but only quadratic pixels are allowed, therefore, $82\,m * 82\,m$ was selected. That means, the benefit due to the improved data quality has partly been compensated by a smaller grid size, meaning, less smoothing and more noise but more detailed knowledge of the plume location at a higher horizontal resolution.

Chapter 6

Summary

The goal of this master thesis is to estimate emission rates of point sources from spectroscopic measurements recorded by the MAMAP instrument.
More specific, the aim is to analyze the flights over the two CO_2 emitting coal-fired power plants Jänschwalde and Schwarze Pumpe in 2011 to quantify the emission rates, which have not been analyzed yet. In this context, significant parametres are wind and potential temperature profiles. New vertically highly resolved profiles should minimize the error in the estimated emission rates. This has already been done for CH_4 targets in Krings et al. (2013) but not for CO_2 from power plants. These new profiles are also applied to flights of a campaign executed in 2007. The results of Jänschwalde and Schwarze Pumpe in 2007 have already been published in Krings et al. (2011) but only vertically coarse wind and no potential temperature profiles have been used.
For that purpose, it is necessary to extract column-averaged dry air mole fractions of carbon dioxide (XCO_2) from the measured raw data and spectra of MAMAP. In the next step, the XCO_2 is inverted to emission rates using external data. It can be referred to already available retrieval and inversion algorithms, which have to be adjusted and modified to accommodate for the new MAMAP data set in 2011 and better resolved wind and new potential temperature data. Moreover, the emission fluxes determined from the flight in 2007 only using vertically low resolved wind data are compared to the flight in 2007 using highly resolved wind data.

Following steps were necessary to achieve emission rate estimates of the power plants Jänschwalde and Schwarze Pumpe for 2007 and 2011:

- Installation of all routines and software packages on a new system.
- Test runs of the retrieval (without inversion algorithm). This also included reproduction of XCO_2 of 2007 published in Krings et al. (2011) and a comparison between both results.
- Extracting of flight parametres for example, flight altitude, surface elevation or

SZA, for the flight in 2011.

- Retrieval of XCO_2 from the new measurements in 2011.
- Comparison of the data quality of XCO_2 between the flight in 2007 and 2011.
- Development of new algorithms in order to derive a mean wind speed of a specific plume, based on new vertically highly resolved profiles from the German Weather Service.
- Inversion of the 2007 data set on basis of the new mean wind speeds.
- Comparison of emission rate estimates for either power plants in 2007 using the new wind speed, to the already published (Krings et al., 2011) and reported ones.
- Inversion of the new measurements of 2011 also with the new wind speeds.

The Master thesis is summarized in the following:
A short motivation was given showing the advantages of he MAMAP instrument in the beginning. In order to derive a reasonable mean wind speed of a plume, which depended on the vertical wind profile as well as on its location in the atmosphere, the second chapter addressed the dynamics and stability of the lower atmosphere. Additionally, the physical background, in particular, in terms of infrared spectroscopy was explained. This was important to interpret the measurements by MAMAP correctly.
Next, the MAMAP instrument, its influence on the measurements, and the retrieval algorithm converting the spectra into column-averaged dry air mole fractions were described. The algorithm inverting the XCO_2 into emission rates by simulating the measurements with a Gaussian plume model was also introduced. Its correct application needed precise knowledge of the plume location e.g., plume height, plume extent, plume direction, plume velocity and plume divergence, and, therefore, the stability of the atmosphere and planetary boundary layer height. These parametres were extracted and taken into account by a new approach/algorithm utilizing the new vertically highly resolved profiles under consideration of the vertical plume distribution to calculate its mean wind speed needed for the inversion process.
The forth part was dedicated to the application of the retrieval. It has been shown that it worked properly. The reproduced column-averaged dry air mole fractions of carbon dioxide in 2007 over Jänschwalde showed only a small shift in the position compared to the XCO_2 published in Krings et al. (2011). This position shift led back to a correction for the location of the measurements added to the algorithm. In order to retrieve the XCO_2 for the new flights in 2011 over the power plants Jänschwalde and Schwarze Pumpe, important flight parametres were extracted from the data set of that flight. The comparison between the XCO_2 of 2007 and 2011 has shown that the RMS was reduced due to assembling of a spatial scrambler/homogenizer in the MAMAP instrument. This

enhanced data quality also led to an improved single measurement precision by a factor of 2 and avoided additional filtering of the data by RMS values for the 2011 flight. Krings et al. (2013) came to the same conclusion in case of the CH_4 point sources.
In chapter five, the previously obtained column-averaged dry air mole fractions of CO_2 were used to estimate the CO_2 emission rates of the power plants Jänschwalde and Schwarze Pumpe in 2007 and 2011. For that purpose, the inversion model based on the Gaussian plume model in combination with the new wind model was applied. It has been demonstrated that the new wind model produces reasonable mean wind speeds leading to deviations from the reported emission rates of maximal $\pm 15.0\,\%$ (Jänschwalde 2007: $\pm 3.5\,\%$, Schwarze Pumpe 2007: $+15.0\,\%$, Jänschwalde 2011: $-7.9\,\%$ if actual emission was the same as in 2007).
Compared to the emission rate estimate of Jänschwalde 2007 in Krings et al. (2011), which overestimated the reported emission by $8.3\,\%$, the bias could be reduced by a factor of 2 with the new atmospheric profiles. For Schwarze Pumpe, the emission rate estimates in Krings et al. (2011) and in this study are not directly comparable because the quasi stationary assumption of the plume model was violated by a changing wind direction during the overflight. Moreover, two different apporaches have been used ('single track inversion' in this study and the 'modified entire plume inversion' in Krings et al. (2011)) for Schwarze Pumpe 2007. Even so, the emission rate estimate of 2007 of the power plants Jänschwalde and Schwarze Pumpe of this study and in Krings et al. (2011) agree well within the uncertainties.
It could also be confirmed that the improved data quality propagates to the emission rates whereby its statistical error has only be reduced by a factor of 1.25 due to a simultaneously decreased gridding size. The largest systematic error of the new wind model arises from the behavior of the emitted plume in the atmosphere and, in particular, the reflection height at very stable layers. This could lead to an additional offset of $\pm 13\,\%$ of the mean wind speed, in case of a wrongly assumend height, propagating linearly to the emission rate.

Final Resume

This study has shown that deriving a mean wind speed based on the vertical plume distribution and layering of the atmosphere is possible but with a limited certainty. Model data and profiles, respectively, serve as a first indicator for the behavior of an emitted plume and possible heights of stable or inversion layers. Even if potential inversion layers can be located, the uncertainty of the exact reflection height still remains. The vertically highly resolved profiles have shown that previously uncertainties in the mean wind speed might have been underestimated and need further investigation. The emission rates, derived during this Master thesis, are not preciser than the already published ones but in the same range. It has turned out that the vertical wind profiles are highly variable and a precise knowledge of the plume location is necessary. The wind model needs also to be tested on the power plant Schwarze Pumpe 2011.

Possibilities to enhance the knowledge in the future are real-time measurements e.g., by a turbulent probe or a wind Lidar on board the same aircraft or an accompanying one. It would also be useful to have some on ground devices which yield also a wind field or at least the height of the planetary boundary layer. These ideas require additional money, human resources and need to be planned and incorporated in advance for flight campaigns and, thus, complex to accomplish.

List of Figures

List of Tables

Bibliography

Ackerman, K. V. and Sundquist, E. T.: Comparison of Two U.S. Power-Plant Carbon Dioxide Emissions Data Sets, Environmental Science and Technology, 42, 5688–5693, doi:10.1021/es800221q, 2008.

Babilotte, A., Lagier, T., Fiani, E., and Taramini, V.: Fugitive Methane Emissions from Landfills: Field Comparison of Five Methods on a French Landfill, Journal of Environmental Engineering, 136, 777–784, doi:10.1061/(ASCE)EE.1943-7870.0000260, 2010.

Banwell, C. N. and Kreiner, W. A.: Molekuelspektroskopie: ein Grundkurs, pp. 73–115, Oldenbourg, Muenchen [u.a.], xIII, 417 S. : Ill., graph. Darst., 1999.

Bell, M. L., Davis, D. L., and Fletcher, T.: A retrospective Assessment of Mortality from the London smog episode of 1952: the role of influenza and pollution, Environmental Health Perspectives, 112, 6–8, 2004.

Bierly, E. W. and Hewson, E. W.: Some Restrictive Meteorological Conditions to be Considered in the Design of Stacks, Journal of Applied Meteorology, 1, 383–390, 1962.

Bohr, N.: I. On the constitution of atoms and molecules, Philosophical Magazine Series 6, 26, 1–25, doi:10.1080/14786441308634955, 1913.

Bohren, C. F. and Clothiaux, E. E.: Fundamentals of atmospheric radiation: an introduction with 400 problems, pp. 91–102, Physics textbook, Wiley-VCH-Verl., Weinheim, xVIII, 472 S. ; 24 cm : Ill., graph. Darst., 2006.

Bovensmann, H., Burrows, J. P., Buchwitz, M., Frerick, J., Noel, S., Rozanov, V. V., Chance, K. V., and Goede, A. P. H.: SCIAMACHY: Mission Objectives and Measurement Modes, Journal of The Atmospheric Sciences, 56, 127–150, 1999.

Buchwitz, M., Rozanov, V. V., and Burrows, J. P.: A near-infrared optimized DOAS method for the fast global retrieval of atmospheric CH4, CO, CO2, H2O, and N2O total column amounts from SCIAMACHY Envisat-1 nadir radiances, Journal of Geophysical Research: Atmospheres, 105, 15 231–15 245, doi:10.1029/2000JD900191, 2000.

Burrows, J., Hoelzle, E., Goede, A., Visser, H., and Fricke, W.: SCIAMACHY - scanning imaging absorption spectrometer for atmospheric chartography, Acta Astronautica, 35, 445 – 451, doi:10.1016/0094-5765(94)00278-T, 1995.

Dennell, R. and Roebroeks, W.: An Asian perspective on early human dispersal from Africa, Nature, 438, 1099–1104, doi:10.1038/nature04259, 2005.

Doms, G. and Schättler, U.: A Description of the Nonhydrostatic Regional Model LM: Part I: Dynamics and Numerics, Deutscher Wetterdienst, Offenbach, 2002.

EPER: European Pollutant Emission Register, 2012.

European Commission: 2007/589/EC, establishing guidelines for the monitoring and reporting of greenhouse gas emissions pursuant to Directive 2003/87/EC of the European Parliament and of the Council, Official Journal of the European Union, 2007.

Evans, S., Deery, S., and Bionda, J.: How reliable are GHG combustion Calculations an emission Factors, Presented at the CEM 2009 Conference, 23-25 September, Milan, Italy, 2009.

Forster, P., Ramaswamy, V., Artaxo, P., Berntsen, T., Betts, R., Fahey, D. W., Haywood, J., Lean, J., Lowe, D. C., Myhre, G., et al.: Changes in atmospheric constituents and in radiative forcing, in: Climate change 2007: The physical science basics. Contribution of working group I to the fourth assessment report of the Intergovernmental Panel on Climate Change, Climate change, 20, 2007.

Frankenberg, C., Meirink, J. F., van Weele, M., Platt, U., and Wagner, T.: Assessing Methane Emissions from Global Space-Borne Observations, Science, 308, 1010–1014, doi:10.1126/science.1106644, 2005.

Gerilowski, K., Tretner, A., Krings, T., Buchwitz, M., Bertagnolio, P. P., Belemezov, F., Erzinger, J., Burrows, J. P., and Bovensmann, H.: MAMAP - a new spectrometer system for column-averaged methane and carbon dioxide observations from aircraft: instrument description and performance analysis, Atmospheric Measurement Techniques, 4, 215–243, doi:10.5194/amt-4-215-2011, 2011.

Gifford, F. A.: Use of routine meteorological observations for estimating atmospheric dispersion, Nuclear Safety, 2, 47–57, 1961.

Haken, H. and Wolf, H. C.: Molekuelphysik und Quantenchemie: Einfuehrung in die experimentellen und theoretischen Grundlagen ; mit 43 Tabellen und 133 Aufgaben, pp. 153–207, Springer-Lehrbuch, Springer, Berlin [u.a.], 5., voellig neubearb. und erw. aufl. edn., xXII, 530 S. : Ill., graph. Darst., 2006.

Hatsopoulos, G. N.: From Watt's Steam Engine to the Unified Quantum Theory of Mechanics and Thermodynamics , Int. J. of Thermodynamics, 9, 97–105, 2006.

Hess, M., Koepke, P., and Schult, I.: Optical Properties of Aerosols and Clouds: The Software Package OPAC, Bull. Amer. Meteor. Soc., 79, 831–844, doi:10.1175/1520-0477(1998), 1998.

IPCC: Climate Change 2007: The Physical Science Basis. Contribution of Working Group I to the Fourth Assessment Report of the Intergovernmental Panel on Climate Changee [Solomon, S., D. Qin, M. Manning, Z. Chen, M. Marquis, K.B. Averyt, M. Tignor and H.L. Miller (eds.)], Cambridge University Press, Cambridge, United Kingdom and New York, NY, USA, 2007.

IPCC-SPM: Summary for Policymaker. In: Climate Change 2007: The Physical Science Basis. Contribution of Working Group I to the Fourth Assessment Report of the Intergovernmental Panel on Climate Changee [Solomon, S., D. Qin, M. Manning, Z. Chen, M. Marquis, K.B. Averyt, M. Tignor and H.L. Miller (eds.)], Cambridge University Press, Cambridge, United Kingdom and New York, NY, USA, 2007.

Jones, P. D., New, M., Parker, D. E., Martin, S., and Rigor, I. G.: Surface air temperature and its changes over the past 150 years, Reviews of Geophysics, 37.

Krings, T.: Greenhouse gas emission rate estimates from airborne remote sensing in the short-wave infrared, Promotion, University of Bremen, 2012.

Krings, T., Gerilowski, K., Buchwitz, M., Reuter, M., Tretner, A., Erzinger, J., Heinze, D., Pflueger, U., Burrows, J. P., and Bovensmann, H.: MAMAP - a new spectrometer system for column-averaged methane and carbon dioxide observations from aircraft: retrieval algorithm and first inversions for point source emission rates, Atmospheric Measurement Techniques, 4, 1735–1758, doi:10.5194/amt-4-1735-2011, 2011.

Krings, T., Gerilowski, K., Buchwitz, M., Hartmann, J., Sachs, T., Erzinger, J., Burrows, J. P., and Bovensmann, H.: Quantification of methane emission rates from coal mine ventilation shafts using airborne remote sensing data, Atmospheric Measurement Techniques, 6, 151–166, doi:10.5194/amt-6-151-2013, 2013.

Liou, K. N.: An introduction to atmospheric radiation, pp. 82–87, International geophysics series ; 84, Academic Press, Amsterdam [u.a.], 2. ed edn., 2002.

Livingston, W. and Wallace, L.: An atlas of the solar spectrum in the infrared from 1850 to 9000 cm-1 (1.1 to 5.4 microns), N.S.O. technical report, National Solar Observatory (U.S.), 1991.

Martin, D. O.: "The Change of Concentration Standard Deviations with Distance", 26, 145–147, doi:10.1080/00022470.1976.10470238, 1976.

Masters, G. M. and Ela, W. P.: Introduction to Environmental Engineering and Science, Prentice Hall, 3. ed edn., 2008.

Pasquill, F.: Atmospheric dispersion of pollution, Quarterly Journal of the Royal Meteorological Society, 97.

Reuter, M., Buchwitz, M., Schneising, O., Hase, F., Heymann, J., Guerlet, S., Cogan, A. J., Bovensmann, H., and Burrows, J. P.: A simple empirical model estimating atmospheric CO_2 background concentrations, Atmospheric Measurement Techniques, 5, 1349–1357, doi:10.5194/amt-5-1349-2012, 2012.

Roedel, W. and Wagner, T.: Physik unserer Umwelt: Die Atmosphäre, Springer-Verlag Berlin Heidelberg, 3. ed. edn., doi:10.1007/978-3-642-15729-5, 2011.

Rothman, L., Gordon, I., Barbe, A., Benner, D., Bernath, P., Birk, M., Boudon, V., Brown, L., Campargue, A., Champion, J., Chance, K., Coudert, L., Dana, V., Devi, V., Fally, S., Flaud, J., Gamache, R., Goldman, A., Jacquemart, D., Kleiner, I., Lacome, N., Lafferty, W., Mandin, J., Massie, S., Mikhailenko, S., Miller, C., Moazzen-ahmadi, N., Naumenko, O., Nikitin, A., Orphal, J., Perevalov, V., Perrin, A., Predoi-cross, A., Rinsland, C., Rotger, M., Simeckova, M., Smith, Sung, K., Tashkun, S., Tennyson, J., Toth, R., Vandaele, A., and Vander Auwera, J.: The HITRAN 2008 molecular spectroscopic database, Journal of Quantitative Spectroscopy and Radiative Transfer, 110, 533–572, doi:10.1016/j.jqsrt.2009.02.013, 2009.

Rozanov, A., Rozanov, V., Buchwitz, M., Kokhanovsky, A., and Burrows, J. P.: SCIATRAN 2.0 A new radiative transfer model for geophysical applications in the 175 2400 nm spectral region, Advances in Space Research, 36, 1015–1019, doi: 10.1016/j.asr.2005.03.012, 2005.

Schneising, O., Buchwitz, M., Burrows, J. P., Bovensmann, H., Reuter, M., Notholt, J., Macatangay, R., and Warneke, T.: Three years of greenhouse gas column-averaged dry air mole fractions retrieved from satellite Part 1: Carbon dioxide, Atmospheric Chemistry and Physics, 8, 3827–3853, doi:10.5194/acp-8-3827-2008, 2008.

Schneising, O., Buchwitz, M., Burrows, J. P., Bovensmann, H., Bergamaschi, P., and Peters, W.: Three years of greenhouse gas column-averaged dry air mole fractions retrieved from satellite - Part 2: Methane, Atmospheric Chemistry and Physics, 9, 443–465, doi:10.5194/acp-9-443-2009, 2009.

Schneising, O., Buchwitz, M., Reuter, M., Heymann, J., Bovensmann, H., and Burrows, J. P.: Long-term analysis of carbon dioxide and methane column-averaged mole fractions retrieved from SCIAMACHY, Atmospheric Chemistry and Physics, 11, 2863–2880, doi:10.5194/acp-11-2863-2011, 2011.

Seinfeld, J. H. and Pandis, S. N.: Atmospheric Chemistry and Physics: From Air Pollution to Climate Change, John Wiley and Sons, Inc., 2. ed edn., 2006.

Stull, R. B.: An Introduction to Boundary Layer Meteorology, p. 666, Kluwer Acad. Publ. Dordrecht, 1988.

Sutton, O. G.: A Theory of Eddy Diffusion in the Atmosphere, Proceedings of the Royal Society of London. Series A, Containing Papers of a Mathematical and Physical Character, 135, pp. 143–165.

Turner, D. B.: Workbook of Atmospheric Dispersion Estimates, National Air Pollution Control Administration, 1970.

Wallace, J. M. and Hobbs, P. V. H.: Atmospheric science: an introductory survey, International geophysics series ; 92, Elsevier, Amsterdam [u.a.], 2. ed. edn., xVI, 483 S. : Ill., graph. Darst., Kt., 2006.

Wu, J., Huang, X., Carter, S., and Bowman, J. M.: Tests of MULTIMODE calculations of rovibrational energies of CH4, Chemical Physics Letters, 426, 285 – 289, doi:10.1016/j.cplett.2006.06.024, 2006.

Wuebbles, D. J. and Hayhoe, K.: Atmospheric methane and global change, Earth-Science Reviews, 57, 177 – 210, doi:10.1016/S0012-8252(01)00062-9, 2002.

Wunch, D., Toon, G. C., Blavier, J.-F. L., Washenfelder, R. A., Notholt, J., Connor, B. J., Griffith, D. W. T., Sherlock, V., and Wennberg, P. O.: The Total Carbon Column Observing Network, Philosophical Transactions of The Royal Society B: Biological Sciences, 369, 2087–2112, doi:10.1098/rsta.2010.0240, 2011.

Declaration

Herewith I declare that I wrote my Master Thesis without external support and that I did not use other than quoted sources and auxiliary means.

All statements which are literally or analogously taken from other publications, have been identified as quotations.

After having handed in my Master Thesis, I am not allowed to make any modifications.

Bremen, August 15, 2013 _____

Signature